Structured catalysts and reactors for three phase catalytic reactions

Manipulating activity and selectivity in nitrite hydrogenation

Roger Brunet Espinosa

STRUCTURED CATALYSTS AND REACTORS FOR THREE PHASE CATALYTIC REACTIONS

MANIPULATING ACTIVITY AND SELECTIVITY IN NITRITE HYDROGENATION

Promotion committee:

Chairman:	Prof. dr. ir. J.W.M. Hilgenkamp	University of Twente
Promotor:	Prof. dr. ir. L. Lefferts	University of Twente
Members:	Prof.dr.ir. R.G.H. Lammertink	University of Twente
	Prof. dr. G. Mul	University of Twente
	Prof.dr. F.G. Mugele	University of Twente
	Prof. dr. R. Dittmeyer	Karlsruhe Institute of Technology
	Prof. dr. J.H. Bitter	Wageningen UR

The research described in this thesis was financially supported by NanoNextNL, a micro- and nanotechnology consortium of the government of The Netherlands and 130 partners.

Structured catalysts and reactors for three phase catalytic reactions: Manipulating activity and selectivity in nitrite hydrogenation.

Pictures cover: Jordi Riba (www.jordiriba.net).

ISBN: 978-90-365-4143-5

DOI-number: 10.3990/1.9789036541435

URL: http://dx.doi.org/10.3990/1.9789036541435

Printed by Gildeprint – Enschede, The Netherlands.

STRUCTURED CATALYSTS AND REACTORS FOR THREE PHASE CATALYTIC REACTIONS

MANIPULATING ACTIVITY AND SELECTIVITY IN NITRITE HYDROGENATION

DISSERTATION

to obtain

the degree of doctor at the University of Twente,

on the authority of the rector magnificus,

Prof.dr. H. Brinksma,

on account of the decision of the graduation committee,

to be publicly defended

on Friday 3rd of June, 2016 at 16:45

by

Roger Brunet Espinosa

born on 22nd of February, 1988

in Barcelona, Spain

This dissertation has been approved by:

Prof. dr. ir. L. Lefferts (Promotor)

Gràcies Maria, sense tu no hagués pogut mai.

Per a tu, avi.

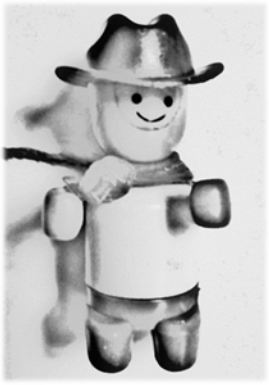

Table of contents

Chapter 1

Introduction

1. Mass transport

Heterogeneous catalysis demands for catalyst supports with high (hydro)thermal and mechanical stability and high specific area. The active component, highly dispersed in the porous media, needs high accessibility since diffusion plays a crucial role in the reaction rate. A heterogeneous reaction in a liquid is generally described in seven steps. Initially, reactants diffuse from the bulk liquid to the external surface of the catalyst support through a stagnant layer around the catalyst particles (external diffusion). Then, the reactants diffuse internally inside the catalytic pores towards the vicinity of the active phase, where they adsorb at the catalytic surface. There, the reaction takes place (generally *via* a sequence of elementary steps), leading to the adsorbed products. Desorption of the final products occurs, followed by internal diffusion towards the pore mouth of the support. Finally, the products diffuse through the external stagnant layer, reaching the bulk liquid [1-4].

The external diffusion is a physical hindrance that can create external heat or mass transfer limitations. It only depends on the hydrodynamics of the reactor. The internal diffusion inside the pores of the particles can generate internal mass transfer limitations, and more rarely, internal temperature gradients (catalyst support can act as a good thermal conductor) [1, 5]. These are negative effects since they hinder the intrinsic catalytic activity and therefore, they are generally prevented by shortening the pore length (small support particles with high porosity) and improving the hydrodynamics (*i.e.* stirring). In the end, the catalytic activity is defined by the interplay of intrinsic (thermodynamics and kinetics) and extrinsic (hydrodynamics and transport phenomena) processes [4, 5].

Thiele modulus (ϕ, Equation 1) can be used to assess if the activity of a catalyst is impeded by internal transport. Small values of this parameter indicates little mass transfer limitations. The effectiveness factor (η, Equation 2) indicates the degree of internal diffusion limitations in a catalyst particle. It can be derived from the Thiele

modulus and indicates the ratio between the observed reaction rate and the reaction rate with no internal transfer limitations [1, 4, 6, 7].

$$\phi = R_p * \sqrt{\frac{k * S_a * \rho_P}{D_{eff}}} \quad \text{Equation 1}$$

$$\eta = \frac{3}{\phi} * \left(\left(\frac{1}{\tanh \phi} \right) - \left(\frac{1}{\phi} \right) \right) \quad \text{Equation 2}$$

R: radius of diffusion path, k: rate constant, S_a: metallic surface area per gram of support, ρ_P: density of the support and D_{eff}: effective diffusivity.

This classical description of mass transport inside catalyst pores is not always sufficient for describing systems with gas or heat generation. Datsevich predicted theoretically that some of these reactions will generate a chaotic movement of the liquid inside the pores, altering the transport mechanisms [8-17]. This will happen when the partial pressure of saturated gas or vapour will exceed the maximum pressure in the pores, leading to bubble formation (figure 1a). These bubbles will grow until reaching the pore mouth (figure 1b). Then they will be swept away by the liquid flow and their pressure will equilibrate with the pressure in the reactor. When the bubble starts leaving the pore, the displacement of the meniscus and the subsequent stretching of the remaining liquid will cause a pressure decrease inside the pore (figure 1c). Immediately after, fresh liquid will fill the pore by capillarity forces. This process, called oscillation theory, repeats continuously, creating a convective flow inside the catalytic pores [8, 9, 16, 17]. It is worth stressing that this theory describes an ideal catalyst pore but does not consider that real catalysts contain a three-dimensional network of interconnected pores with different lengths and diameters [8].

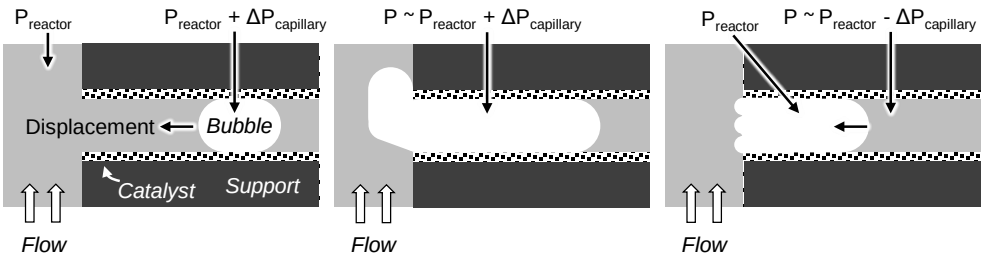

Figure 1: Scheme of bubble evolution in an ideal catalyst pore, adapted from Datsevich [9].

Some of the most remarkable consequences of the oscillation theory are the pulsating convective flow inside the pores (with speeds up to 100 m/s) which enhances internal and external mass transport [8, 16, 17]. However, this liquid motion only occurs at the proximity of the pore mouth, creating stagnant zones in the depths of the pores [17]. Additionally, the changes in pressure inside the pores may damage the catalyst structure due to cavitation [9]. According to this theory, processes could be intensified by modifying the catalyst pore structure [9, 10] or by inducing bubble generation [9, 16, 17].

2. Three phase catalytic reactions

Three phase catalytic reactions are multiphase reactions where generally gas and liquid phases are contacted with a solid catalyst. These reactions are prone to suffer mass transfer limitations since the solubility of the gases is limited and because the diffusion coefficient is typically four orders of magnitude lower in liquid phase than in gas phase. These reactions are generally performed in conventional reactors like packed bed trickle-phase reactors and slurry reactors, *i.e.* bubble columns or stirred tanks [2, 6, 18-21].

Packed bed reactors offer significant mass transfer limitations due to the relatively large size of the packing bodies (typically 1-10 mm). Generally, these sizes cannot be smaller otherwise the reactor would suffer important pressure drops. Moreover, the chaotic distribution of the liquid in the void space of the catalytic bed might create stagnant zones, channelling and/or flow maldistribution which can directly affect

conversion and selectivity. However, the catalyst loading can be very high, leading to high reaction rates per volume reactor [2, 18].

Slurry reactors are often chosen because the particle size of the catalyst is very small (typically 30 μm), leading to high external surface area and short diffusion lengths. These reactors are specially used for hydrogenation or oxidation reactions since they offer little mass transfer limitations and thus, high reaction rates per gram catalyst. However, attrition of the catalyst is a frequent problem that creates significant losses in metallic surface area. Additionally, filtration of the small particles rises as a major inconvenient since it increases the cost of the process. On the other hand, the highly active suspended catalyst particles only represent a small fraction of the total volume of the reactor, leading to low activities per unit of reactor volume [2, 18, 20].

To circumvent the disadvantages of the conventional reactors, structured catalytic systems at both micro- and meso-levels rise as an excellent alternative. Structured reactors not only enhance the reaction rates by suppressing mass and heat transfer limitations but also simplify the fluid mechanics and the scaling up [5].

3. Structured reactors

A structured reactor is a regular spatial structure [22] characterized by high accessibility to the active phase, low pressure drop and easy catalyst recovery [5, 6]. The most commonly used is the monolith due to its extensive use in environmental applications and in the automotive industry [5, 18, 23, 24]. Other types of structured reactors commonly use are membrane reactors [25, 26], foams [27-31], microreactors [32-34], cloths [35, 36], wires [37], filters [38] and fibres [39].

3.1. Membrane reactors

Catalytic membrane reactors generally consist of a layer or a catalytic bed enclosed in a membrane, and have a well-defined gas-liquid interface. Membrane reactors can be classified based on different criteria. One classification is based on the way of

combining the membrane and the catalyst which distinguishes between reactors where the catalyst is incorporated inside the membrane (catalytic membrane) and reactors where the catalyst is part of a packed bed and the membrane has purely a separation role [40].

A more widely used classification is based on the role of the membrane and divides membrane reactors into three categories, namely, extractors, contactors and distributors (figure 2) [41-43]. Extractors are the most commonly studied [40] and are used to selectively extract a product from the reaction zone through the membrane. This is especially important to accelerate consecutive or equilibrium-restricted reactions. Contactors are mainly facilitating the contact of the reactants with the catalyst *via* the use of catalytic membranes. Both reactants can be fed from the two different sides of the membrane (interfacial contactors) or can be forced from the same side (flow-through contactors) [40, 42]. For the latter case, the contact time of the reactants in the membrane pores can be adjusted by modifying the operating conditions which is hardly doable in conventional porous catalysts. Several examples in literature prove that this can enhance activity and selectivity for some gas-liquid reactions [44-46]. In distributors, the gaseous reactant is fed separately through the membrane, allowing an independent control of the gas and liquid phases [40, 42, 47-51]. As a consequence, the concentration of the gaseous reactant can be kept low and homogeneous in the axial direction of the reaction zone. This is crucial for reactions where selectivity is strongly dependent on the concentration of the gaseous reactant [43], reactions that may present flammable mixtures [50], or reactions that have high gas consumption with low gas solubility.

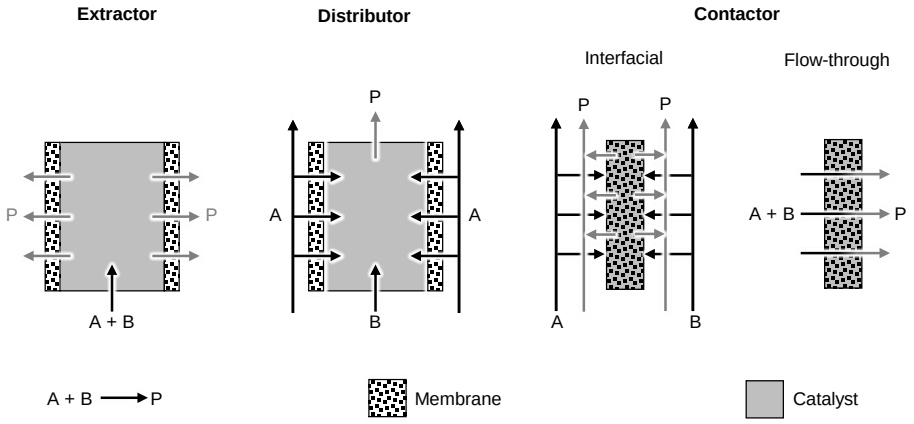

Figure 2: Different types of membrane reactors based on the role of the membrane, adapted from Miachon et al [40].

Scaling-up membrane reactors is simple, especially for tubular geometries, since many reactors can be easily integrated in one membrane module (numbering-up). One of the major inconveniences of these reactors is mass transfer limitations in the liquid due to the laminar flow. To achieve high conversions, long residence times are needed, otherwise a significant fraction of the liquid reactant will by-pass the reaction zone. Recent work carried out by Pashkova et al. [41] and Vospernik et al. [25] showed that mass transport in the liquid can be enhanced by creating turbulence of the liquid with glass beats or static mixers respectively. Another option consists on miniaturizing the membrane reactor by decreasing its characteristic length. This results in an increase of the surface area per volume reactor, leading to shorter diffusion distances for the liquid reactant.

3.2. Foams

Solid foams consist of three-dimensional networks of connected strands containing interconnected pores (figure 3). This material mimics to some degree the inverse structure of a packed bed made of dense spheres [5, 52]. Strictly speaking, foams are not structured reactors since they do not present regularity. However, they exhibit features that are typical for those types of reactor such as high and uniform

accessibility to the catalytic active sites, and low pressure drops [5]. Therefore, in this work, we treat them as structured reactors. Recently, the use of solid foams has increased due to their different possible applications as heat exchangers, chemical inert packings and catalyst supports [53]. They can be made of a wide variety of materials, namely, ceramics, metals, carbon and silicon carbide [52]. Foams exhibit a very high porosity (voidage up to 97-98%) but low specific surface areas, which are similar to those of monoliths (lower than 4 $m^2.g^{-1}$) [6]. Therefore, foams are not suitable for direct use as catalyst support since they cannot accommodate enough active sites [5]. Thus, they are generally coated with a porous material where the catalyst is located [52]. Typical coatings consist of washcoats and carbon nano-fibres (CNFs). The former, often suffers from a poor attachment, although Cristiani et al. [54] managed to solve this problem applying $Ni/MgAl_2O_4$ washcoats on FeCr alloy foams. Coatings with well-attached CNFs have been also successfully synthesized [27-29], exhibiting high porosity and low tortuosity.

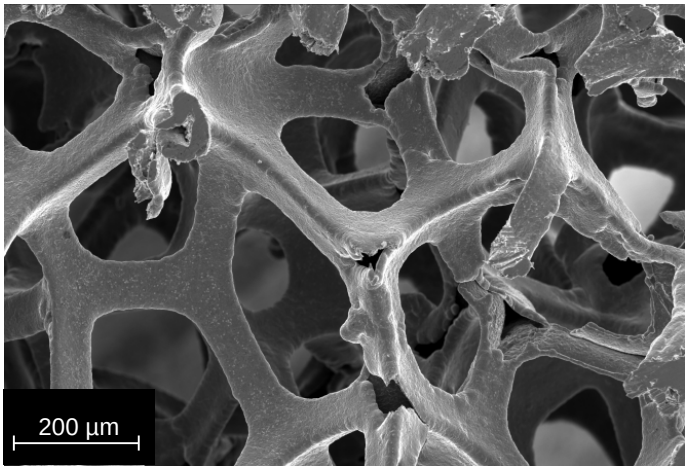

Figure 3: HRSEM image of a nickel foam.

3.3. Microreactors

Microreactors are devices with typical sizes in the sub-millimetre range used to perform chemical reactions. They present several advantages as compared to conventional reactors in the field of chemical synthesis, chemical kinetics studies and process development [34]. The high surface-to-volume ratio of microreactors enhance heat and mass transfer rates and therefore, allow exploring wider ranges of process parameters (pressure, temperature and concentrations) [32-34, 55, 56]. Additionally, higher yields and selectivities can be achieved due to the better control of reaction conditions at the catalytic sites. The small characteristic dimensions of these devices also play an important role in the safety of the process, allowing processes that at conventional bench scale are restricted by safety concerns and the use of expensive reagents [32-34, 55]. For instance, accidental spills of hazardous and toxic chemicals can be easily contained. Scaling up microreactors is simple since it only requires replication of the microreactor units rather than a complete design of the pilot and/or the industrial plant [34]. As a consequence, in case of failure, the damaged microreactor can be easily isolated and replaced without compromising the overall production. The use of this technology is especially attractive for the chemical and pharmaceutical sectors which have a relatively low production of certain fine chemicals (less than a few metric tons per year) [34, 55, 56].

4. Carbon nano-fibres (CNFs)

CNFs are nano-graphitic filaments with aspect ratios (length/diameter) greater than 100 (figure 4). CNF formation was first observed in processes involving the conversion of carbon-containing gases such as Fischer Tropsch synthesis [57]. This was detrimental for these reactions due to catalyst deactivation and mechanical damage of both catalyst and reactor. During the 1980s, Robertson [58] and Baker et al. [59] developed controlled synthesis of CNFs from supported Ni, Co or Fe catalysts. Nowadays, CNFs are used as polymer additives [60], for electronics [61], for gas storage [57], for fuel cells [57] and as catalyst supports [29, 57]. They are

synthesized using several techniques, namely, carbon-arc [62], laser vaporization and catalytic vapour deposition [57]. The latter method is widely used in literature [59, 63] because it allows relatively cheap operation and can be made in high yields [6, 52]. CNFs are catalytically grown on Ni, Fe and Co metals [57, 64], using a variety of carbon source gas (*i.e.* ethylene, CO, methane, ethane) and a typical temperature range of 400-900 °C.

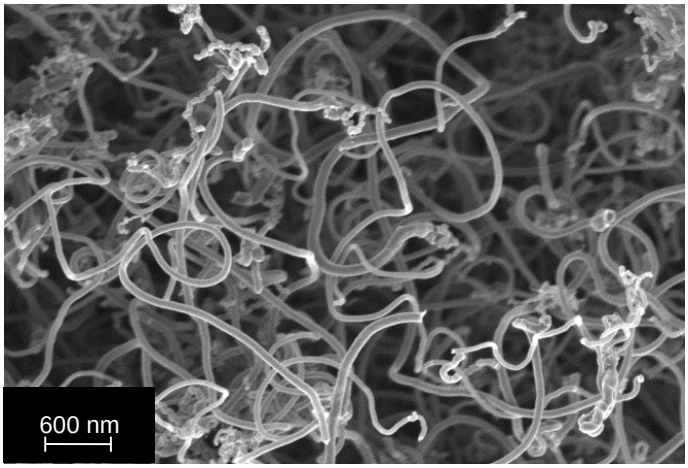

Figure 4: HRSEM image of CNFs grown from nickel catalyst.

It has been proposed in literature [59, 65, 66] that the CNF growth mechanism proceeds via three steps. In the first step, the carbon source gas (hydrocarbon) decomposes at the surface of the metal catalyst producing C and H_2. In the second step, the carbon dissolves inside the catalyst particle and diffuses to the metal-support interface where the carbon starts nucleating. In the third and last step, carbon continues precipitating, lifting up the metal particle from the support until full carbon encapsulation of the metal particle by a thick carbon layer occurs. Hoogenraad et al. [66] suggested that the initiation of the CNFs could be caused by the decomposition of a metal carbide (into carbon and metal) formed during the diffusion of the dissolved carbon in the metal particles. However, there is still some debate on the carbon diffusion mechanism before precipitation since it has also been proposed that it occurs *via* surface diffusion rather than bulk diffusion.

The resulting CNFs are characteristic for their high mechanical strength, for being chemically inert and presenting a surface chemistry that can be easily modified [57, 67]. Additionally, they present high surface area (typically 100-200 m^2/g), large pore volume (0.5-2 cm^3 /g) and absence of microporosity due to their entanglement and open structure [6, 57, 67].

Direct application of CNFs as powder support catalyst [57, 67-69] can pose some problems in conventional reactors. In slurry phase reactors, agglomeration may occur during filtration [38] while in trickle bed reactors, high pressure drops can be observed. Therefore, a very attractive option is to grow CNFs on macroporous supports such as foams [28, 30, 31, 36], monoliths [70], glass and metal filters [38, 71], carbon cloth [36], etc.

5. Nitrite hydrogenation

The concentration of nitrite (NO_2^-) and nitrate (NO_3^-) in ground water has become a critical environmental problem due to the extensive agriculture (animal excretion and fertilizers) and the industrial effluents [72]. Although nitrate is not directly harmful for humans, it leads to the formation of nitrite in the body *via* reduction processes. This can cause several health diseases such as methemoglobinemia (blue baby syndrome) and hypertension, or can cause the formation of carcinogenic nitrosamines [73-78]. Therefore, the European Environment Agency (EEA) regulated the concentration of nitrate and nitrite to a maximum of 50 and 0.1 mg/L respectively [79, 80].

These inorganic contaminants can be removed from water *via* different physicochemical techniques such as reverse osmosis, ion exchange and electrodialysis [81]. However, these techniques do not eliminate the contaminants but concentrate them in a waste stream. Biological degradation is also a viable alternative but is slow and complex. The key problem is that bacteria need other organic contaminants to grow and multiply and therefore de-nitrification of water

that only contains N-contaminants is not feasible. Hence, new routes had to be developed to efficiently remove these contaminants.

In 1989, Vorlop et al [82] developed the catalytic hydrogenation of nitrate and nitrite to nitrogen. However, the formation of the by-product ammonia could not be prevented. This rose as a main drawback since the concentration of ammonia is also strictly limited by the EEA to 0.5 mg/L. Since then, extensive research has focused on the suppression of ammonia formation.

The hydrogenation of nitrate requires a bimetallic catalyst, consisting generally of Pd-Cu or Pd-Sn [80] (Equation 3), while the hydrogenation of nitrite is performed in a noble metal, mainly Pd or Pt (Equations 4 and 5). The selectivity towards nitrogen or ammonia is strongly influenced by various reaction parameters. At low temperatures and pH values, the selectivity towards nitrogen is favoured [29, 83-85]. Low H/N ratio of reactant intermediates at the catalyst surface also enhances the formation of nitrogen since nitrogen formation requires less hydrogen than ammonia formation [29, 75, 79, 85, 86].

$$2NO_3^- + 2H_2 \xrightarrow{\text{Pd-Cu}} 2NO_2^- + 2H_2O \qquad \text{Equation 3}$$

$$2NO_2^- + 3H_2 + 2H^+ \xrightarrow{\text{Pd}} N_2 + 4H_2O \qquad \text{Equation 4}$$

$$NO_2^- + 3H_2 + 2H^+ \xrightarrow{\text{Pd}} NH_4^+ + 2H_2O \qquad \text{Equation 5}$$

6. Scope and outline of the thesis

In this work, structured reactors have been used for the study of multiphase catalytic reactions. The work aimed at improving the activity and selectivity of nitrite hydrogenation and at understanding the effect of the transport mechanisms on the reaction kinetics for the hydrogen peroxide decomposition.

Chapter 2 describes the synthesis of a CNF-based membrane reactor for selective hydrogenation of nitrite to nitrogen. First, the reactor synthesis was optimized to

achieve high surface areas while maintaining an open and homogeneous structure, and relatively low pore filling to avoid mass transfer limitations. Afterwards, the membrane reactor was tested in nitrite hydrogenation and compared with other reactor layouts. Finally, the effect of the H/N ratio of reactant intermediates at the catalyst surface on the ammonia selectivity was studied by varying the concentration of the reactants and the reactor layout.

In **Chapter 3**, three different CNF-based membrane reactors were prepared and tested in the nitrite hydrogenation. The three reactors presented egg-shell structures, varying the position of the catalyst in the membrane. This allowed studying the influence of the concentration profiles in the reaction zone within the membrane and the effect of the H/N ratio on the selectivity of the reaction. The effect of the hydrogen concentration on the activity was also investigated for each reactor.

In **Chapter 4**, nickel 'hairy' foams were synthesized without addition of any noble metals, and tested in the nitrite hydrogenation as such. A study was conducted to identify the active phase and to understand how this catalyst activates and deactivates.

In **Chapter 5**, hydrogen peroxide (H_2O_2) decomposition was performed in a microreactor simulating catalyst pores. The pores differed in the geometrical dimensions and in the amount of catalyst. The effect of these parameters and the H_2O_2 concentration on the formation of bubbles was studied. We also investigated how the formation of these bubbles affects the transport mechanisms inside the pores and the impact of these phenomena on reaction kinetics.

Finally, **Chapter 6** summarizes the main findings of the thesis and concludes with some recommendations for further work.

7. References

1. Averill, M., van Santen and van Leeuwen ed. *Catalysis: an integrated approach*. Second ed. 2000, Elsevier. 582.
2. P.A. Ramachandran, R.V.C., ed. *Three phase catalytic reactors*. ed. G.a.B.S. publishers. 1983: New York.
3. Fogler, H.S., *Elements of chemical reaction engineering*. 2006.
4. Klaewkla, R., Arend, M., and Hoelderich, W.F., *A Review of Mass Transfer Controlling the Reaction Rate in Heterogeneous Catalytic Systems*. 2011: INTECH Open Access Publisher.
5. Gascon, J., van Ommen, J.R., Moulijn, J.A., and Kapteijn, F., *Structuring catalyst and reactor – an inviting avenue to process intensification.* Catal. Sci. Technol., 2015. 5(2): p. 807-817.
6. Chinthaginjala, J.K., *Hairy foam: Thin layers of carbon nanofibers as catalyst support for liquid phase reactions*, in *CPM*. 2010, University of Twente: Enschede. p. 149.
7. Thiele, E.W., *Relation between Catalytic Activity and Size of Particle.* Industrial & Engineering Chemistry, 1939. 31(7): p. 916-920.
8. Datsevich, L.B., *Some theoretical aspects of catalyst behaviour in a catalyst particle at liquid (liquid–gas) reactions with gas production: oscillation motion in the catalyst pores.* Applied Catalysis A: General, 2003. 247(1): p. 101-111.
9. Datsevich, L.B., *Oscillation theory.* Applied Catalysis A: General, 2005. 294(1): p. 22-33.
10. Datsevich, L.B., *Oscillation theory.* Applied Catalysis A: General, 2005. 279(1-2): p. 181-185.
11. Datsevich, L.B., *Oscillation Theory.* Applied Catalysis A: General, 2004. 273(1-2): p. 151-156.
12. Datsevich, L.B., *Oscillation theory.* Applied Catalysis A: General, 2004. 262(2): p. 149-153.
13. Oehmichen, T., Datsevich, L., and Jess, A., *Influence of Bubble Evolution on the Effective Kinetics of Heterogeneously Catalyzed Gas/Liquid Reactions. Part I: Reactions with Gaseous Products.* Chemical Engineering & Technology, 2010. 33(6): p. 911-920.
14. Oehmichen, T., Datsevich, L., and Jess, A., *Influence of Bubble Evolution on the Effective Kinetics of Heterogeneously Catalyzed Gas/Liquid Reactions. Part II: Exothermic Gas/Liquid Reactions.* Chemical Engineering & Technology, 2010. 33(6): p. 921-931.

15. Blümich, B., Datsevich, L.B., Jess, A., Oehmichen, T., Ren, X., and Stapf, S., *Chaos in catalyst pores.* Chemical Engineering Journal, 2007. 134(1-3): p. 35-44.
16. Datsevich, L.B., *Alternating motion of liquid in catalyst pores in a liquid/liquid–gas reaction with heat or gas production.* Catalysis Today, 2003. 79-80: p. 341-348.
17. Datsevich, L.B., *Oscillations in pores of a catalyst particle in exothermic liquid (liquid–gas) reactions: Analysis of heat processes and their influence on chemical conversion, mass and heat transfer.* Applied Catalysis A: General, 2003. 250(1): p. 125-141.
18. A. Cybulski, J.A.M., *Structured catalysts and reactors*. Second ed, ed. M. Dekker. 2006, New York. 856.
19. Duduković, M.P., Larachi, F., and Mills, P.L., *Multiphase catalytic reactors: a perspective on current knowledge and future trends.* Catalysis Reviews, 2002. 44(1): p. 123-246.
20. Satterfield, C.C., *Trickel-bed reactors.* AIChE Journal, 1975. 21(2): p. 209-228.
21. Roy, S., Bauer, T., Al-Dahhan, M., Lehner, P., and Turek, T., *Monoliths as multiphase reactors: A review.* AIChE Journal, 2004. 50(11): p. 2918-2938.
22. J. A. Moulijn, M.M.a.A.E.v.D., ed. *Chemical Process Technology*. 2013, Wiley.
23. Pangarkar, K., Schildhauer, T.J., van Ommen, J.R., Nijenhuis, J., Kapteijn, F., and Moulijn, J.A., *Structured Packings for Multiphase Catalytic Reactors.* Industrial & Engineering Chemistry Research, 2008. 47(10): p. 3720-3751.
24. Geus, J.W. and van Giezen, J.C., *Monoliths in catalytic oxidation.* Catalysis Today, 1999. 47(1–4): p. 169-180.
25. Vospernik, M., Pintar, A., Berčič, G., Batista, J., and Levec, J., *Potentials of Ceramic Membranes as Catalytic Three-Phase Reactors.* Chemical Engineering Research and Design, 2004. 82(5): p. 659-666.
26. Aran, H.C., *Porous ceramic and metallic microreactors*, in *SFI*. 2011, University of Twente: Enschede. p. 126.
27. Jarrah, N., van Ommen, J., and Lefferts, L., *Mechanistic aspects of the formation of carbon-nanofibers on the surface of Ni foam: A new microstructured catalyst support.* Journal of Catalysis, 2006. 239(2): p. 460-469.
28. Wenmakers, P.W.A.M., van der Schaaf, J., Kuster, B.F.M., and Schouten, J.C., *"Hairy Foam": carbon nanofibers grown on solid carbon foam. A fully accessible, high surface area, graphitic catalyst support.* Journal of Materials Chemistry, 2008. 18(21): p. 2426-2436.

29. Chinthaginjala, J.K. and Lefferts, L., *Support effect on selectivity of nitrite reduction in water.* Applied Catalysis B: Environmental, 2010. 101(1-2): p. 144-149.
30. Ledoux, M.-J. and Pham-Huu, C., *Carbon nanostructures with macroscopic shaping for catalytic applications.* Catalysis Today, 2005. 102-103: p. 2-14.
31. Cordier, A., Flahaut, E., Viazzi, C., Laurent, C., and Peigney, A., *In situ CCVD synthesis of carbon nanotubes within a commercial ceramic foam.* Journal of Materials Chemistry, 2005. 15(37): p. 4041.
32. Doku, G.N., Verboom, W., Reinhoudt, D.N., and van den Berg, A., *On-microchip multiphase chemistry—a review of microreactor design principles and reagent contacting modes.* Tetrahedron, 2005. 61(11): p. 2733-2742.
33. Gavriilidis, A., Angeli, P., Cao, E., Yeong, K.K., and Wan, Y.S.S., *Technology and Applications of Microengineered Reactors.* Chemical Engineering Research and Design, 2002. 80(1): p. 3-30.
34. Jensen, K.F., *Microreaction engineering — is small better?* Chemical Engineering Science, 2001. 56(2): p. 293-303.
35. Matatov-Meytal, U. and Sheintuch, M., *Activated carbon cloth-supported Pd–Cu catalyst: Application for continuous water denitrification.* Catalysis Today, 2005. 102–103: p. 121-127.
36. Cantoro, M., Golovko, V.B., Hofmann, S., Williams, D.R., Ducati, C., Geng, J., Boskovic, B.O., Kleinsorge, B., Jefferson, D.A., Ferrari, A.C., Johnson, B.F.G., and Robertson, J., *Wet catalyst assisted growth of carbon nanofibers on complex three-dimensional substrates.* Diamond and Related Materials, 2005. 14(3–7): p. 733-738.
37. Niranjan, K. and Pangarkar, V.G., *An International Journal of Research and DevelopmentHydrodynamic and mass transfer characteristics of polypropylene multifilament wire gauze packings.* The Chemical Engineering Journal, 1983. 27(1): p. 49-57.
38. Tribolet, P. and Kiwi-Minsker, L., *Carbon nanofibers grown on metallic filters as novel catalytic materials.* Catalysis Today, 2005. 102–103: p. 15-22.
39. Tzeng, S.-S., Hung, K.-H., and Ko, T.-H., *Growth of carbon nanofibers on activated carbon fiber fabrics.* Carbon, 2006. 44(5): p. 859-865.
40. Miachon, S., Dalmon, J.-A., *Catalysis in membrane reactors: what about the catalyst?* Topics in Catalysis, 2004. 29(1-2): p. 59-65.

41. Pashkova, A., Dittmeyer, R., Kaltenborn, N., and Richter, H., *Experimental study of porous tubular catalytic membranes for direct synthesis of hydrogen peroxide.* Chemical Engineering Journal, 2010. 165(3): p. 924-933.
42. Huuhtanen, M., Seelam, P.K., Kolli, T., Turpeinen, E., and Keiski, R.L., *Advances in catalysts for membrane reactors.* 2013: p. 401-432.
43. Aran, H.C., Chinthaginjala, J.K., Groote, R., Roelofs, T., Lefferts, L., Wessling, M., and Lammertink, R.G.H., *Porous ceramic mesoreactors: A new approach for gas-liquid contacting in multiphase microreaction technology.* Chemical Engineering Journal, 2011. 169(1-3): p. 239-246.
44. González-Burillo, M., Barbosa, A.L., Herguido, J., and Santamaria, J., *The influence of the permeation regime on the activity of catalytic membranes for methane combustion.* Journal of Catalysis, 2003. 218(2): p. 457-459.
45. Ilinitch, O.M., Cuperus, F.P., Nosova, L.V., and Gribov, E.N., *Catalytic membrane in reduction of aqueous nitrates: operational principles and catalytic performance.* Catalysis Today, 2000. 56(1–3): p. 137-145.
46. Torres, M., López, L., Domínguez, J.M., Mantilla, A., Ferrat, G., Gutierrez, M., and Maubert, M., *Olefins catalytic oligomerization on new composites of beta-zeolite films supported on α-Al2O3 membranes.* Chemical Engineering Journal, 2003. 92(1–3): p. 1-6.
47. Matatov-Meytal, Y. and Sheintuch, M., *Catalytic fibers and cloths.* Applied Catalysis A: General, 2002. 231(1–2): p. 1-16.
48. Julbe, A., Farrusseng, D., and Guizard, C., *Porous ceramic membranes for catalytic reactors — overview and new ideas.* Journal of Membrane Science, 2001. 181(1): p. 3-20.
49. Dittmeyer, R., Svajda, K., and Reif, M., *A Review of Catalytic Membrane Layers for Gas/Liquid Reactions.* Topics in Catalysis, 2004. 29(1-2): p. 3-27.
50. Mota, S., Miachon, S., Volta, J.C., and Dalmon, J.A., *Membrane reactor for selective oxidation of butane to maleic anhydride.* Catalysis Today, 2001. 67(1–3): p. 169-176.
51. Dittmeyer, R., Höllein, V., and Daub, K., *Membrane reactors for hydrogenation and dehydrogenation processes based on supported palladium.* Journal of Molecular Catalysis A: Chemical, 2001. 173(1–2): p. 135-184.
52. Jarrah, N., *Microstructured catalyst support based on carbon nano-fibers (CNFs)*, in *CPM*. 2004, University of Twente: Enschede. p. 123.

53. Zhang, W., Zhang, B., and Shi, Z., *Study on hydrodynamic performance and mass transfer efficiency of nickel foam packing.* Procedia Engineering, 2011. 18: p. 271-276.
54. Cristiani, C., Finocchio, E., Latorrata, S., Visconti, C.G., Bianchi, E., Tronconi, E., Groppi, G., and Pollesel, P., *Activation of metallic open-cell foams via washcoat deposition of Ni/MgAl2O4 catalysts for steam reforming reaction.* Catalysis Today, 2012. 197(1): p. 256-264.
55. Mills, P.L., Quiram, D.J., and Ryley, J.F., *Microreactor technology and process miniaturization for catalytic reactions—A perspective on recent developments and emerging technologies.* Chemical Engineering Science, 2007. 62(24): p. 6992-7010.
56. Hessel, V., Angeli, P., Gavriilidis, A., and Löwe, H., *Gas−Liquid and Gas−Liquid−Solid Microstructured Reactors: Contacting Principles and Applications.* Industrial & Engineering Chemistry Research, 2005. 44(25): p. 9750-9769.
57. De Jong, K.P. and Geus, J.W., *Carbon Nanofibers: Catalytic Synthesis and Applications.* Catalysis Reviews, 2000. 42(4): p. 481-510.
58. Robertson, S.D., *Graphite Formation from Low Temperature Pyrolysis of Methane over some Transition Metal Surfaces.* Nature, 1969. 221(5185): p. 1044-1046.
59. Baker, R.T.K., Barber, M.A., Harris, P.S., Feates, F.S., and Waite, R.J., *Nucleation and growth of carbon deposits from the nickel catalyzed decomposition of acetylene.* Journal of Catalysis, 1972. 26(1): p. 51-62.
60. Hammel, E., Tang, X., Trampert, M., Schmitt, T., Mauthner, K., Eder, A., and Pötschke, P., *Carbon nanofibers for composite applications.* Carbon, 2004. 42(5–6): p. 1153-1158.
61. Milne, W.I., Teo, K.B.K., Amaratunga, G.A.J., Legagneux, P., Gangloff, L., Schnell, J.P., Semet, V., Thien Binh, V., and Groening, O., *Carbon nanotubes as field emission sources.* Journal of Materials Chemistry, 2004. 14(6): p. 933-943.
62. Ros, T.G., *Rhodium Complexes and Particles on Carbon Nanofibres*. 2002, University of Utrecht: Utrecht.
63. Chinthaginjala, J.K., Bitter, J.H., and Lefferts, L., *Thin layer of carbon-nano-fibers (CNFs) as catalyst support for fast mass transfer in hydrogenation of nitrite.* Applied Catalysis A: General, 2010. 383(1–2): p. 24-32.

64. Liu, B.C., Gao, L.Z., Liang, Q., Tang, S.H., Qu, M.Z., and Yu, Z.L., *A study on carbon nanotubes prepared from catalytic decomposition of C2H2 or CH4 over the pre-reduced LaCoO3 perovskite precursor.* Catalysis Letters. 71(3): p. 225-228.

65. Yang, R.T. and Chen, J.P., *Mechanism of carbon filament growth on metal catalysts.* Journal of Catalysis, 1989. 115(1): p. 52-64.

66. Hoogenraad, M.S., *Growth and utilization of carbon fibers*. 1995, University of Utrecht.

67. Serp, P., Corrias, M., and Kalck, P., *Carbon nanotubes and nanofibers in catalysis.* Applied Catalysis A: General, 2003. 253(2): p. 337-358.

68. Pham-Huu, C., Keller, N., Ehret, G., Charbonniere, L.c.J., Ziessel, R., and Ledoux, M.J., *Carbon nanofiber supported palladium catalyst for liquid-phase reactions: An active and selective catalyst for hydrogenation of cinnamaldehyde into hydrocinnamaldehyde.* Journal of Molecular Catalysis A: Chemical, 2001. 170(1–2): p. 155-163.

69. Park, C. and Baker, R.T.K., *Catalytic Behavior of Graphite Nanofiber Supported Nickel Particles. 3. The Effect of Chemical Blocking on the Performance of the System.* The Journal of Physical Chemistry B, 1999. 103(13): p. 2453-2459.

70. Jarrah, N.A., van Ommen, J.G., and Lefferts, L., *Growing a carbon nano-fiber layer on a monolith support; effect of nickel loading and growth conditions.* Journal of Materials Chemistry, 2004. 14(10): p. 1590.

71. Zinfer, R.I., Nadezhda, V.S., Vladimir, N.K., Nina, A.R., Vladimir, A.U., Nikolai, T.V., and Hubert, J.V., *Development of methods of growing carbon nanofibers on silica glass fiber supports.* Catalysis Today, 2005. 102–103: p. 85-93.

72. Zhao, Y., *Colloidal nanoparticles as catalyst and catalyst precursors for nitrite hydrogenation*. 2015, University of Twente: Enschede.

73. Pintar, A., *Catalytic processes for the purification of drinking water and industrial effluents.* Catalysis Today, 2003. 77(4): p. 451-465.

74. Pintar, A., Berčič, G., and Levec, J., *Catalytic liquid-phase nitrite reduction: Kinetics and catalyst deactivation.* AIChE Journal, 1998. 44(10): p. 2280-2292.

75. Shuai, D., Choe, J.K., Shapley, J.R., and Werth, C.J., *Enhanced Activity and Selectivity of Carbon Nanofiber Supported Pd Catalysts for Nitrite Reduction.* Environmental Science & Technology, 2012. 46(5): p. 2847-2855.

76. D'Arino, M., Pinna, F., and Strukul, G., *Nitrate and nitrite hydrogenation with Pd and Pt/SnO2 catalysts: the effect of the support porosity and the role of carbon dioxide in the control of selectivity.* Applied Catalysis B: Environmental, 2004. 53(3): p. 161-168.
77. Hörold, S., Vorlop, K.D., Tacke, T., and Sell, M., *Development of catalysts for a selective nitrate and nitrite removal from drinking water.* Catalysis Today, 1993. 17(1–2): p. 21-30.
78. Devard, A., Ulla, M.A., and Marchesini, F.A., *Synthesis of Pd/Al2O3 coating onto a cordierite monolith and its application to nitrite reduction in water.* Catalysis Communications, 2013. 34: p. 26-29.
79. Franch, C., Lammertink, R.G.H., and Lefferts, L., *Partially hydrophobized catalyst particles for aqueous nitrite hydrogenation.* Applied Catalysis B: Environmental, 2014. 156-157: p. 166-172.
80. Barrabés, N. and Sá, J., *Catalytic nitrate removal from water, past, present and future perspectives.* Applied Catalysis B: Environmental, 2011. 104(1-2): p. 1-5.
81. *Nitrate Removal From Drinking Water—Review.* Journal of Environmental Engineering, 1997. 123(4): p. 371-380.
82. Vorlop, K.-D. and Tacke, T., *Erste Schritte auf dem Weg zur edelmetallkatalysierten Nitrat- und Nitrit-Entfernung aus Trinkwasser.* Chemie Ingenieur Technik, 1989. 61(10): p. 836-837.
83. Hörold, S., Tacke, T., and Vorlop, K.-D., *Catalytical removal of nitrate and nitrite from drinking water: 1. Screening for hydrogenation catalysts and influence of reaction conditions on activity and selectivity.* Environmental Technology, 1993. 14(10): p. 931-939.
84. Höller, V., Rådevik, K., Yuranov, I., Kiwi-Minsker, L., and Renken, A., *Reduction of nitrite-ions in water over Pd-supported on structured fibrous materials.* Applied Catalysis B: Environmental, 2001. 32(3): p. 143-150.
85. Ebbesen, S.D., Mojet, B.L., and Lefferts, L., *Effect of pH on the Nitrite Hydrogenation Mechanism over Pd/Al2O3 and Pt/Al2O3: Details Obtained with ATR-IR Spectroscopy.* The Journal of Physical Chemistry C, 2011. 115(4): p. 1186-1194.
86. Wada, K., Hirata, T., Hosokawa, S., Iwamoto, S., and Inoue, M., *Effect of supports on Pd–Cu bimetallic catalysts for nitrate and nitrite reduction in water.* Catalysis Today, 2012. 185(1): p. 81-87.

Chapter 2

Carbon nano-fibre based membrane reactor for selective nitrite hydrogenation

Chapter published as:

Brunet Espinosa, R.; Rafieian, D.; Lammertink R.G.H and Lefferts, L.; Carbon nano-fiber based membrane reactor for selective nitrite hydrogenation (accepted in Catalysis Today journal, available online).

Abstract

Catalytic hydrogenation of nitrite in drinking water demands control over the selectivity towards nitrogen, minimizing the formation of ammonia. This selectivity is strongly influenced by the H/N ratio of reaction intermediates at the catalyst surface. Therefore, we fabricated a membrane reactor that feeds separately hydrogen gas and a nitrite solution. This allows dosing low but homogeneous hydrogen concentrations along the axial direction of the catalyst bed. As a consequence, low H/N ratios can be achieved, favouring the formation of nitrogen without limiting the nitrite conversion. We demonstrate that this reactor concept offers better nitrogen selectivity than conventional reactor configurations where hydrogen is pre-dissolved in the nitrite solution.

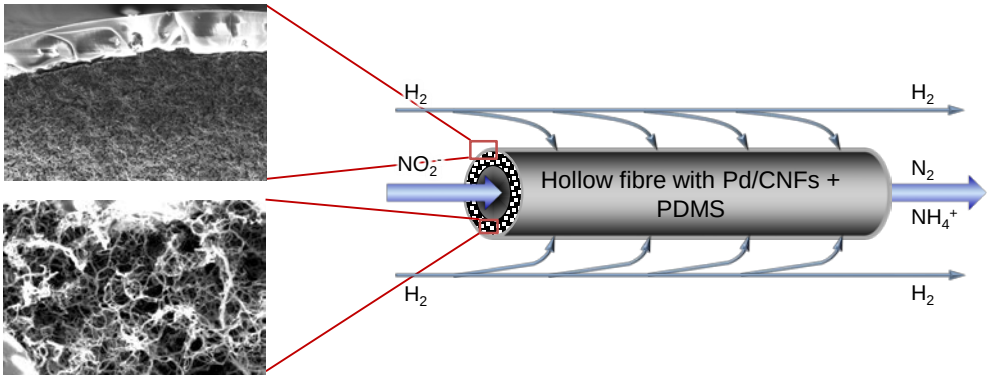

1. Introduction

During the last few decades, the use of microreactors for chemical conversion and analysis has experienced spectacular advances. With these miniaturized reaction systems, it is possible to explore wider pressure, temperature and concentration ranges as compared to conventional macroscopic reactors. Due to their small characteristic length, microreactors exhibit a high surface to volume ratio, where surface active forces dominate volume forces. This entails an enhancement in mass and heat transport that can improve activity and selectivity because the local concentrations and temperature at the active sites can be better controlled. Additionally, the small volume of the microreactors allows a safer operation, especially for the formation of hazardous and toxic chemicals [1-8].

Suppression of heat and mass transfer limitations in microreactors makes them ideal for three phase catalytic reactions. These reactions generally suffer from transport limitations caused, for example, by stagnant film resistance at the external surface area of the solid catalyst and internal diffusion in porous catalyst bodies. These effects are more prominent when the reactions are fast. To minimize resistance at the gas-liquid interface, a good dispersion of the gas in the liquid is required. This can be achieved via the use of membrane microreactors [6-10].

Micro/macro membrane reactors are usually divided in three categories, namely extractors, distributors and contactors. Extractors selectively remove a product of an equilibrium-restricted reaction to obtain higher yields as compared to conventional reactors. Distributors allow dosing the gas reactant along the reaction zone generating an optimum concentration profile. This becomes important for reaction networks where side reactions are strongly influenced by the concentration of one of the reactants. Contactors present a catalytic membrane, creating a well-defined reaction interface between two different media [11-15].

Nitrite (NO_2^-) and nitrate (NO_3^-) hydrogenation are fast liquid phase reactions that can benefit from micro-membrane technology [16-19]. These compounds are

typical water contaminants that can lead to health problems. Although nitrate is not directly harmful for humans, it can be converted in the body to nitrite via reduction processes leading to health diseases such as methemoglobinemia (blue baby syndrome) or to the formation of carcinogenic nitrosamines [20-25]. A very efficient way to remove nitrite is via catalytic hydrogenation [26]. This reaction converts nitrite to nitrogen and ammonia (NH_4^+, by-product). European Environment Agency (EEA) established a maximal ammonia concentration in water of 0.5 mg/L [27]. Therefore, significant efforts focus on the prevention of ammonia formation. The selectivity of nitrite hydrogenation is influenced by various parameters such as temperature, pH and the H/N ratio of reactant intermediates at the catalyst surface. This last parameter can be tuned by regulating the concentration of the reactants (nitrite and hydrogen). Higher H/N ratios will lead to higher ammonia selectivity while low ratios would lead to higher nitrogen selectivity [22, 27-30]. However, low hydrogen concentrations could also generate mass transfer limitations, resulting in low efficient use of the catalyst and consequently very low activity.

In the current work, we explore the use of a distributor membrane reactor for the nitrite hydrogenation reaction. This reactor consists of a hollow alumina structure partly filled with carbon nano-fibres (CNFs) loaded with palladium nanoparticles. The outer structure is covered with a polydimethylsiloxane (PDMS) membrane. This reactor can regulate the hydrogen dosed in the reaction zone by hydrogen dilution with argon to achieve low H/N ratios. The reactor configuration allows low and homogeneous hydrogen concentration along the catalyst bed, preventing hydrogen depletion since hydrogen is continuously supplied through the membrane. Although membrane reactors have been studied for nitrate and nitrite hydrogenation [18, 19, 31-33], tuning of the selectivity via manipulation of the H/N ratio has not yet been demonstrated. Operation at low H/N ratio with nitrite solution pre-saturated with hydrogen would not be efficient, as exhaustion of dissolved hydrogen would cause very low nitrite conversion.

2. Experimental

2.1. Reagents and Materials

Porous ceramic α-alumina (α-Al_2O_3) hollow fibres with a mean pore size of 800 nm were obtained from Hyflux CEPAration Technologies, Europe. These hollow fibres have an inner and outer diameter of 0.9 and 1.9 mm respectively and were cut in pieces 55 mm long. They were used as catalyst support and at the same time used to construct the reactor. Nickel was deposited using nickel nitrate hexahydrate (Merck), urea (Merck) and nitric acid (65%, Merck). CNFs were grown using ethylene (99.95% PRAXAIR), hydrogen and nitrogen (99.999% INDUGAS) without any further purification. Palladium was deposited using palladium acetylacetonate (Alfa Aesar) and toluene (> 99.9%, Merck). PDMS coating was performed using toluene (> 99.9% Merck) as solvent and a two component PDMS RTV 615 kit (Permacol B.V.) consisting of a vinyl terminated pre-polymer and a Pt-catalysed cross-linker named RTV-A and RTV-B respectively. The catalytic tests were performed using sodium nitrite (> 99%, Merck) as nitrite source.

2.2. Fabrication of the reactors

The synthesis of the membrane reactors consisted of several steps. Initially, nickel was deposited in the macropores of the alumina hollow fibre, followed by CNF growth. Any loose CNFs were removed by sonication. In the next step, palladium was deposited on the CNFs and then was calcined and reduced. Finally, the outer wall of the alumina fibre was coated with a viscous PDMS solution, forming a dense layer after curing. Several parameters of the process were studied to optimize the reactor (shown in table 1).

Nickel deposition: Homogeneous deposition-precipitation technique was used to deposit nickel on the walls of the macropores of the hollow alumina fibre. The hollow fibres were immersed as-received in a stirred nickel nitrate solution of 80

ml. Several concentrations were used: 0.02, 0.2, 1.0 and 5.0 g Ni/L. The temperature was kept constant at 100 °C and a reflux system was connected to avoid evaporation of the water. The initial pH of the solution was adjusted at pH = 3.5 using a diluted nitric acid solution. To precipitate the nickel on the alumina, 20 ml of concentrated urea solution (1.06 g / 20 ml) were added drop-wise during the first 15 minutes. After 2 h of deposition time, the sample was removed from the nickel solution, rinsed thoroughly with miliQ water and dried at 85 °C during 2 h in vacuum.

CNF growth: Catalytic chemical vapour deposition technique was used to grow CNFs from the nickel particles deposited in the previous step. The synthesis of the CNFs was performed using an in-house build quartz tube reactor with an inner diameter of 10 mm. The hollow fibre was reduced in a mixture of 20% H_2 and 80% N_2 for 2 h at different temperatures (450, 550, 750 or 850 °C) to vary the nickel particle size. The temperature was raised from 20 °C to the target temperature at 6 °C/min under 100 ml/min of N_2. After the reduction, the system was cooled down in 80 ml/min N_2 flow to the CNF synthesis temperature (350, 450, 550, 600, 700, 750 °C). The CNF synthesis was performed during 30 min with a gas mixture containing 7% H_2, 20% ethylene (C_2H_4) and 73% N_2 with a total flow rate of 100 ml/min. Finally, the system was cooled down in nitrogen flow rate of 80 ml/min.

In the last step, the sample was sonicated in miliQ water for 30 min to remove any CNFs poorly attached to the alumina fibre. After this treatment, the sample was dried at 85 °C during 2 h in vacuum.

Pd deposition: A solution of palladium acetylacetonate in toluene with a concentration of 6 mg Pd/ml was prepared for depositing palladium. The hollow fibre with CNFs was immersed in 25 ml of the prepared solution for 17 h. Next, it was removed from the solution and dried during 2 h at 85 °C in vacuum. In the next step, the sample was oxidized in air for 1 h at 250 °C and reduced for 2 h in a gas mixture of 50% H_2 and 50% N_2 also at 250 °C. Finally the system was cooled down to room temperature in nitrogen flow.

PDMS coating: Adapted from Aran et al. [19], a two component PDMS kit (RTV-A and RTV-B, 10:1 weight ratio) was dissolved in toluene at 85 wt% and heated at 60 °C in a home-made reflux setup for pre-crosslinking the PDMS/toluene solution. The viscosity of the solution was measured by a Brookfield DV-II + Pro viscometer equipped with a nr-61 spindle. When a viscosity of 100 mPa.s was reached, the cross-linking was stopped by immersing the solution in ice. The hollow alumina fibre was dip-coated with the partially cross-linked solution at a constant speed of 2.5 mm/s. To prevent the presence of PDMS inside the alumina fibre, one end of the alumina was sealed by glue and the open end was kept above the PDMS solution during the coating. In the last step, the coated sample was completely cross-linked in an oven at 80 °C for 2 h. Finally, both ends of the alumina were cut to remove the glue at one side and the non-coated part at the other side.

2.3. Catalytic test

The membrane reactor, named 'H_2 outside', was tested for the nitrite hydrogenation to assess its performance in a fast liquid phase reaction. The performance of this reactor was compared with two other reactor layouts ('H_2 inside' and 'Packed bed'), as described in detail in sections 2.3.1., 2.3.2. and 2.3.3. All reactions were carried in liquid phase at 20 °C. Inlet and outlet concentrations of nitrite and ammonia were measured with an in-line Ion Chromatograph (Dionex, ICS 1000) from which nitrite conversion and ammonia selectivity were calculated according to equation 1 and 2 respectively. It was assumed that nitrogen and ammonia are the only products [23, 27, 29], calculating nitrogen selectivity based on the mass balance. The liquid flow rate was varied between 0.1 and 3 ml/min and the gas flow rate between 100 and 200 ml/min keeping the hydrogen partial pressure between 0.04 and 1.00 bar (balanced with Ar). Experiments were done under similar nitrite conversions to allow comparing selectivities of the different reactor layouts. In all cases, the solutions were not buffered.

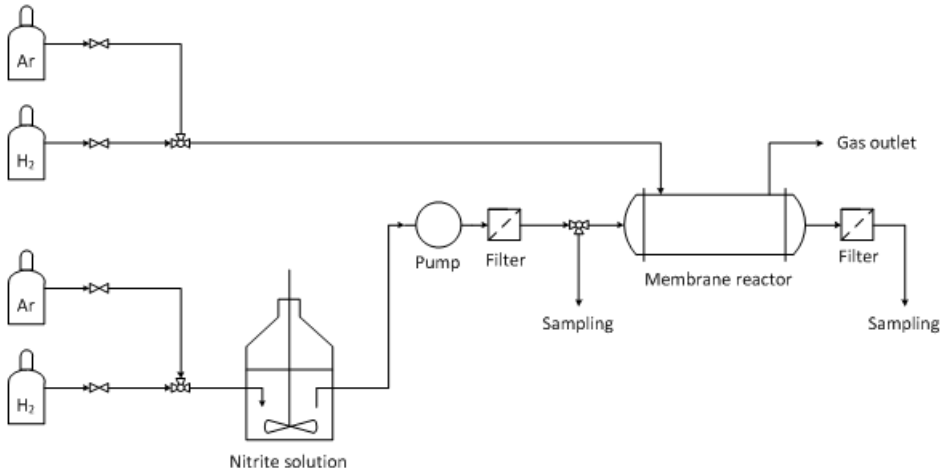

Figure 1: Setup used for the nitrite hydrogenation.

$$NO_2^- \text{ conversion} = \frac{[NO_2^-]_{initial} - [NO_2^-]_{final}}{[NO_2^-]_{initial}} \cdot 100 \qquad \text{Equation 1}$$

$$NH_4^+ \; selectivity = \frac{[NH_4^+]_{final} - [NH_4^+]_{initial}}{[NO_2^-]_{initial} - [NO_2^-]_{final}} \cdot 100 \qquad \text{Equation 2}$$

2.3.1. 'H$_2$ outside' layout

This reactor layout embodies the membrane reactor designed to supply low and homogeneous hydrogen concentrations throughout the axial direction of the catalyst bed. The liquid containing nitrite is fed into the tube of the hollow membrane reactor while the gas is fed to the shell of the reactor and is allowed to diffuse through the PDMS membrane coated on the outer wall of the reactor tube (figure 2a). Hydrogen and nitrite are expected to meet and react in the macropores of the α-Al_2O_3 where palladium is deposited on entangled CNFs. In all experiments, liquid is saturated in argon to remove oxygen and other gases present in ambient which could interfere with the reaction. The liquid flow rate used was always 0.2 ml/min with a nitrite concentration between 20 and 1000 μmol/L. The

gas flow rate was supplied with a pressure of 1 bar, feeding a mixture of hydrogen and argon with a hydrogen partial pressure varying between 0.05 and 1 bar.

2.3.2. 'H_2 inside' layout

The reactor used for this layout was physically the same as for 'H_2 outside'. However, it was operated differently. In this design, the liquid containing nitrite was pre-saturated with hydrogen at 1 bar and fed inside the tube of the hollow membrane reactor. Pure argon was supplied at 1 bar to the reactor shell to avoid any permeation of air to the reaction zone (figure 2b). The liquid flow rate was 0.2 ml/min with a nitrite and hydrogen concentrations of 220 μmol/L and 780 μmol/L respectively. Hydrogen concentration in the liquid feed was controlled by the pressure of the hydrogen used to saturate the nitrite solution and was calculated based on Henry's law constant (7.7 $mol.m^{-3}.Pa^{-1}$, [34]).

2.3.3. 'Packed bed' layout

A membrane reactor without any PDMS coating was crushed and sieved to the size of 0.5 mm particles and was tested as a packed bed reactor. The reactor was fed with a nitrite solution pre-saturated in hydrogen at 1 bar (figure 2c). The liquid flow rate was 3 ml/min to obtain the same nitrite conversion as compared to the other reactor layouts. Additionally, one experiment was performed with a low flow rate (0.4 ml/min). Nitrite and hydrogen concentrations were kept at 220 μmol/L and 780 μmol/L respectively.

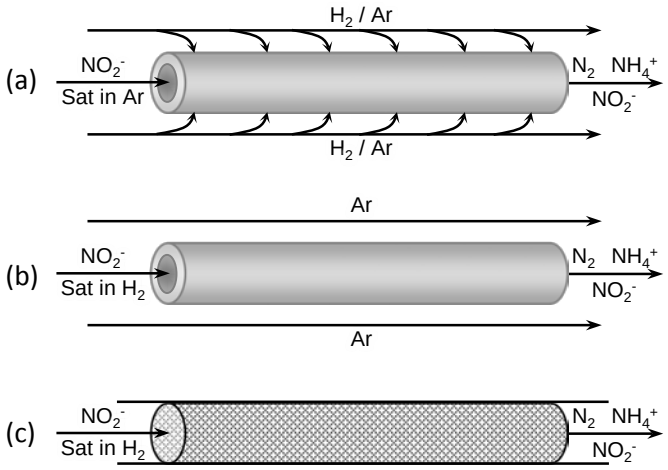

Figure 2: Flow operation during nitrite hydrogenation of the a) 'H_2 outside', b) 'H_2 inside' and c) 'Packed bed' layouts.

2.4. Characterization

The samples were sonicated for 30 min to test the mechanical stability of the grown CNFs and to remove the poorly attached CNFs. The BET surface area of the hollow alumina fibres after CNF growth was calculated from N_2-adsorption isotherm obtained at 77 K (Micromeritics Tristar). The morphology of the synthesized membrane reactors was studied with Scanning Electron Microscopy, HR-SEM (Analysis Zeiss MERLIN HR-SEM). The properties studied include the CNF diameter, the nickel particle size and the thickness of the PDMS layer. Cross-sections were prepared by cutting the samples with a scalpel. CNF diameter and nickel particle size (before CNF growth) were determined based on the average of 200 measurements on five different positions in the sample. The HR-SEM was equipped with Energy Dispersive X-Ray analysis system, EDX (Oxford Instruments X-Max80 EDX), allowing to study the distribution of nickel and carbon in the axial direction of the membrane reactor. The amount of carbon grown in the macropores of the α-Al_2O_3 was measured with an analytical balance by weighing the sample before and after CNF growth. Additionally, also elemental analysis, EA

(Elemental Analyser Inter Science Flash 2000) was used to determine the amount of carbon deposited on the α-Al_2O_3. The average pore size and the void fraction of the α-Al_2O_3 before the CNF growth were determined with Hg porosimetry (Quantachrome Poremaster PM33). The percentage of pore volume filled with CNFs was calculated from the void fraction of the α-Al_2O_3 and the amount of CNFs. The Pd loading on the membrane reactor was determined with X-ray fluorescence spectroscopy, XRF (Philips PW 1480).

3. Results

Figure 3 shows a cross-sectional view of the α-Al_2O_3 hollow fibre as-received, presenting large pore sizes of 800 nm which is in agreement with the specifications of the manufacturer. The porosity of the material, measured with Hg porosimetry is 0.13 cm^3/g and the BET surface area is typically 0.1 m^2/g [18].

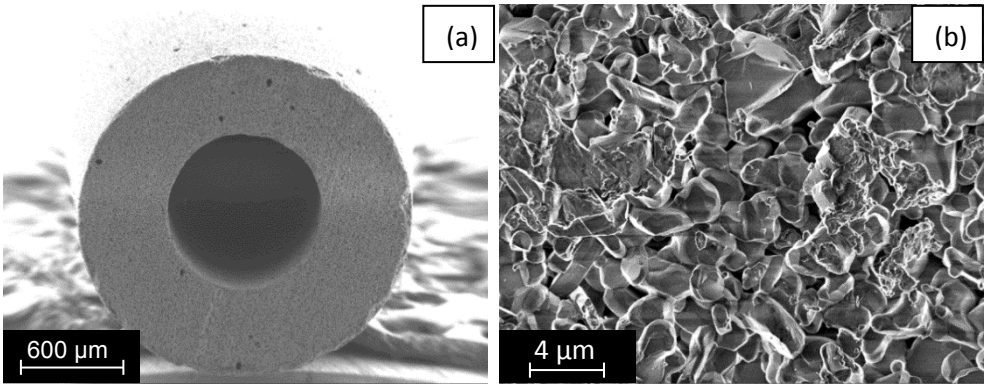

Figure 3: Cross-sectional view of the hollow alumina fibre showing a) a general view at low magnification, b) its macro porosity.

Three parameters were optimized for the synthesis of the membrane reactor: nickel concentration, reduction temperature and CNF growth temperature. The goal was to obtain a material with a high surface area, determined from BET measurements. However, to prevent mass transfer limitations, the material should maintain an open structure with a relatively low fraction of alumina pore volume filled with

CNFs (assessed with Hg porosimetry) and present curly and entangled CNFs (imaged with HRSEM). Finally, the CNFs should be distributed homogeneously in the porous alumina as judged with HRSEM. All information related with the prepared samples can be found in table 1.

3.1. Nickel deposition

Figure 4 shows cross-sections of the alumina hollow fibres, allowing the observation of the morphology of the CNFs inside the alumina macropores. All four samples were prepared using different concentrations of nickel precursor during the nickel deposition.

The sample prepared with a low nickel concentration (0.02 g Ni/L) has few CNFs partly covering the alumina walls. These CNFs can be observed in the bright spots on the alumina grains shown in figure 4a. The low carbon content of this sample (0.2 wt%) leads to a very poor filling of the alumina macropores (approx. 0.6 vol%) which results in a very low surface area of 0.4-0.5 m^2/g (table 1). The sample prepared with a high nickel concentration (5.0 g Ni/L; figure 4d) presents a macroscopic CNF layer (black region) grown on the external surface of the alumina fibre (white region) with an irregular thickness around 200 μm. This massive CNF growth mechanically damages the alumina structure making it more brittle, in agreement with previous work [35]. Moreover, this irregular and highly porous CNF layer is not beneficial for applying a thin PDMS layer free of defects. Therefore, these two samples were not suitable for the purpose of this study.

The samples prepared with 0.2 g Ni/L and 1.0 g Ni/L present a satisfactory CNF coverage (figure 4b and c). However, the 1.0 g Ni/L sample has the highest carbon content and presents the largest surface area (approx. 10 m^2/g_{sample}) combined with a modest filling of the macropores (14.8 vol%; table 1). Therefore, 1.0 g Ni/L was selected as the optimum nickel concentration and the other parameters were studied using this nickel concentration.

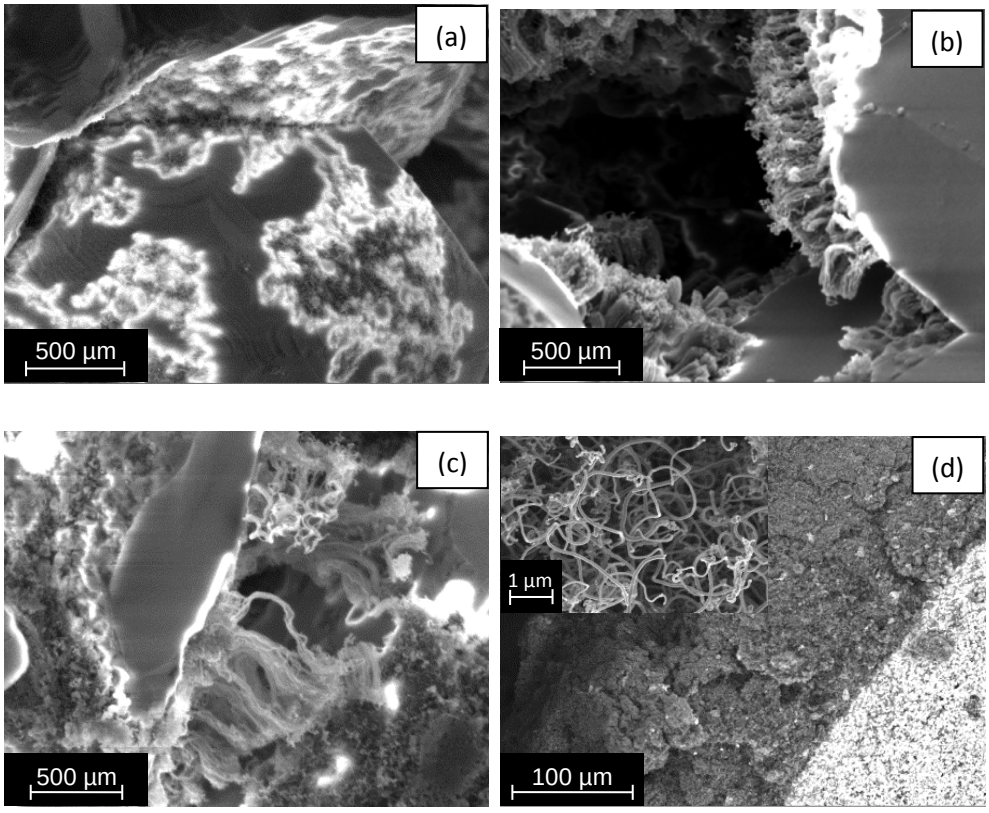

Figure 4: Cross-sectional view of four hollow alumina fibres after pre-treatment in hydrogen at 450 °C and CNF synthesis at 450 °C. Each sample was prepared with a different nickel solution a) (0.02 g Ni/L), b) (0.2 g Ni/L), c) (1.0 g Ni/L) and d) (5.0 g Ni/L). Two magnifications are shown in figure 6d.

3.2. Reduction temperature

The morphology of the CNFs is strongly affected by the nickel particle size, which can be manipulated by the reduction temperature. Four different temperatures were tested followed by CNF synthesis at 450 ˚C.

The different reduction temperatures induced significant differences in the morphology of the CNFs. When using low reduction temperatures (550 and 450 °C), straight and very thin CNFs (3.8 nm at 550 °C, table 2) grow parallel next to

each other, generating groups of packed CNFs that resemble amorphous carbon (figure 5c and d). The resulting morphology, with very small pores between the packed CNFs, would not be very suitable as catalyst support.

Table 1: Properties of all samples with varying nickel amount, reduction temperature and CNF growth temperature. Only the relevant properties were measured for every sample. In all the calculations, cylindrical CNFs with the same diameter are assumed, with a density equal to the density of graphite.

	Ni amount varied				Reduction temperature varied				CNF growth temperature varied				
Nickel concentration (gNi/L)	0.02	0.2	1.0	5.0	1.0	1.0	1.0	1.0	1.0	1.0	1.0	1.0	1.0
Reduction temperature (°C)	450	450	450	450	450	550	750	850	850	850	850	850	850
Reaction temperature (°C)	450	450	450	450	450	450	450	450	350	450	550	600	700
wt% C	0.2	2.5	5.1	7.1	5.1	2.1	1.5	1.7	0.0	1.7	6.6	7.5	3.8
Surface area (m^2/g)	-	-	-	-	-	10.2	5.6	5.4	-	5.4	21.0	16.8	7.0
Calculated surface area (m^2/g)*	0.45	5.0	10.5	-	-	-	-	-	-	-	-	13.5	-
Surface area (m^2/g_{carbon})	-	-	-	-	-	486	381	313	-	313	318	224	183
CNF diameter (nm)	3-4	3-4	3-4	-	-	-	-	-	-	-	-	10	-
Calculated CNF diameter (nm)**	-	-	-	-	-	3.8	5.0	6.0	-	6.0	6.0	8.3	10.2
Pore volume filled (vol%) ***	0.6	7.1	14.8	-	13.7	6.3	4.8	5.5	-	5.3	17.2	25.0	10.3

* The calculated surface area, based on the diameter of the CNFs and the carbon loading = 4(%C) / (CNF density × CNF diameter)

** Calculated CNF diameter , based on surface area and carbon loading = 4(%C) / (CNF density × surface area)

*** Pore volume filled, based on the carbon loading and the original pore volume determined with Hg porosimetry = (weight CNFs / CNF density) / (volume alumina pores)

In case of high reduction temperatures (850 and 750 °C), CNFs present slightly bigger diameter than at low reduction temperatures due to sintering of the nickel particles and exhibit smaller, but still significant, BET surface areas than at 550 °C. However, high reduction temperatures are preferred since CNFs offer an open structure with curly and entangled CNFs (figure 5a and b), reducing the risk of mass transfer limitations. Among the two high reduction temperatures, 850 °C was used as standard temperature for further optimization.

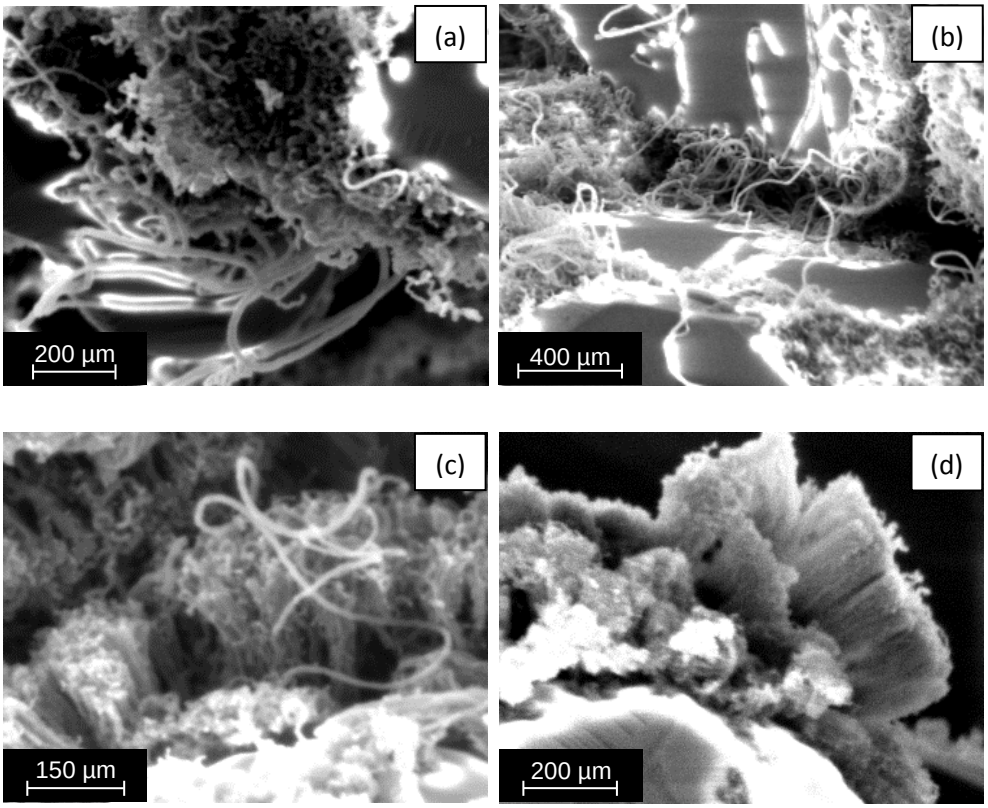

Figure 5: Cross-sectional view of four hollow alumina fibres showing the CNF morphology of the samples reduced at a) 850 °C, b) 750 °C, c) 550 °C, d) 450 °C. All samples were prepared with 1.0 gNi/L and CNFs were grown at 450 °C. Note the differences in scale bar.

3.3. CNF growth temperature

The morphology of the CNFs can also be influenced by the temperature of the CNF growth. To optimize the growth temperature, six different temperatures were tested. All samples were synthesized using a concentration of 1.0 g Ni/L for the nickel deposition and a reduction temperature of 850 °C.

CNFs were successfully grown at the reaction temperatures between 450 and 700 °C (figure 6b-e), where the highest CNF amount was obtained at 600 °C (7.5 wt%; table 1). Moreover, the surface area after growing CNFs at 600 °C is significantly high (16.8 m^2/g; table 1). Although the sample prepared at 550 °C has the highest surface area (21.0 m^2/g; table 1) and relatively low pore filling (17.2 vol%; table 1) the morphology of the CNFs is not well-defined, with some areas containing densely packed CNFs, resembling the morphology of amorphous carbon (figure 6g). At 600 °C, the CNFs are homogeneously distributed and do not agglomerate forming packed areas (figure 6h). Therefore, 600 °C was selected as the optimum CNF growth temperature.

Nickel is not able to catalyse the formation of CNFs at the lowest CNF growth temperature (350 °C), (figure 6a). Only a thin carbon layer appeared at the outer wall of the alumina fibre (figure A1, Appendix A). At 350 °C, the carbon dissolves in the nickel particles, which precipitates during the cooling, forming an amorphous layer that covers the nickel particles [36]. This phenomenon is especially visible at the outer wall of the alumina fibre because it has a higher nickel concentration and it is directly exposed to the gas flow. At the highest CNF growth temperature (750 °C), the CNF coverage was extremely low (figure 6f), showing only few long CNFs present at the internal surface of the alumina tube.

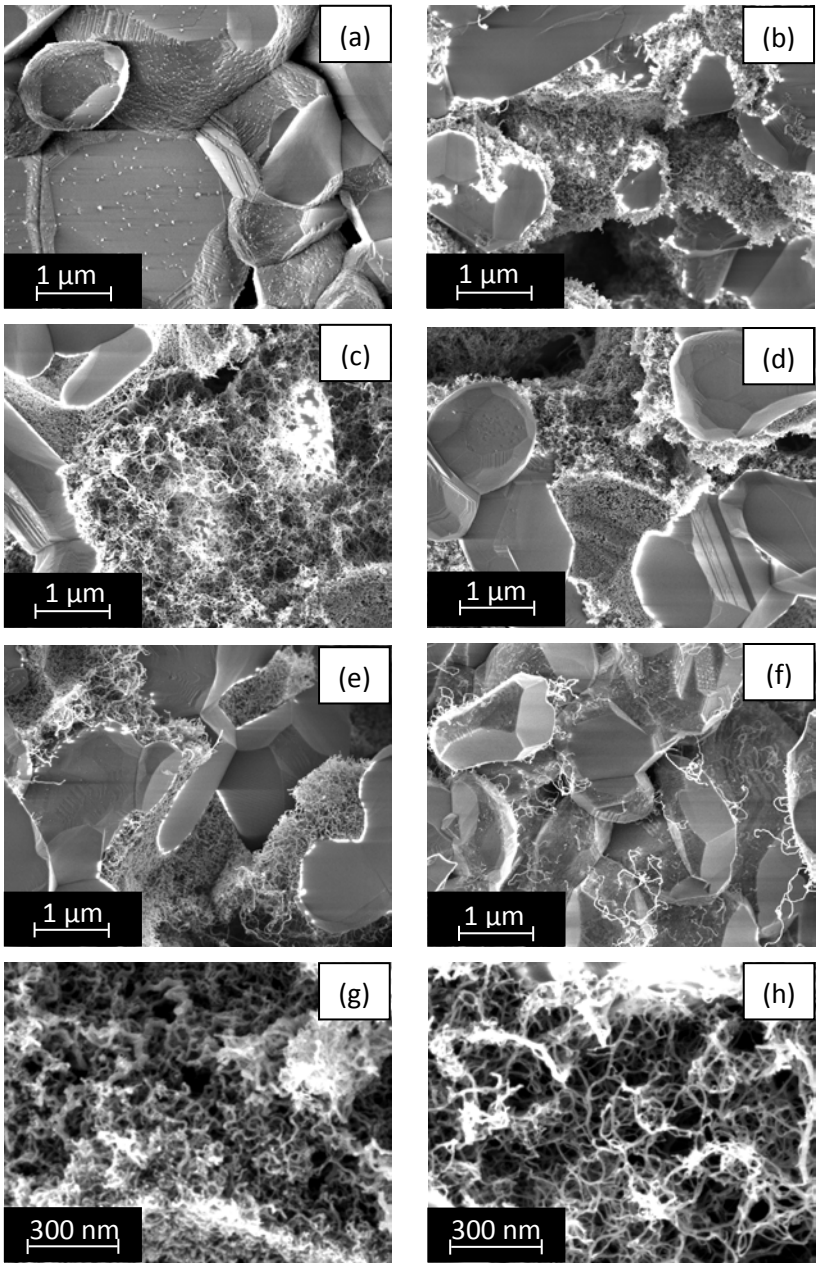

Figure 6: Cross-sectional view of six hollow alumina fibres reduced at 850 °C with CNFs grown at different temperatures, a) 350 °C b) 450 °C, c) 550 °C, d) 600 °C, e) 700 °C, f) 750 °C, g) 550 °C high magnification, h) 600 °C high magnification. All samples were synthesized using 1.0 gNi/L.

3.4. Characterization of the optimal sample

The optimal sample was characterized in more detail, including the Ni/alumina sample before the CNF growth. A homogeneous nickel distribution with an average particle size of 14.0 nm and an average CNF diameter of 10.0 nm were measured with HRSEM (figure A2 and A3, Appendix A). The estimation of CNF diameter based on HRSEM (10.0 nm) results in somewhat higher values than the CNF diameter estimated based on the surface area (8.3 nm, table 1), which is probably due to the broad distribution and the difference in averaging (local number averaged from HRSEM, global surface area averaged from BET). The differences between nickel particle size and CNF diameter is probably caused by nickel fragmentation during CNF growth. The total amount of carbon grown is 7.5 wt%, generating a total surface area of 16.8 m^2/g (table 1), 2 orders of magnitude higher than the bare alumina. Carbon and nickel are both distributed homogeneously throughout the porous alumina. Only near the outer wall, an increase in both concentrations is measured by EDX (figure A4, Appendix A), likely, because the outer alumina wall is directly exposed to the nickel solution during nickel deposition, as well as to ethylene during CNF growth as compared to the pores inside the alumina tube [19].

After palladium deposition, a loading of 0.011 gPd/gCNF was measured with XRF. The palladium loading is reproducible within 5% variation. The dispersion of the palladium particles could not be determined with H_2 or CO chemisorption because nickel is present in significantly higher concentrations than palladium, influencing any chemisorption of CO and H_2.

A SEM image of a cross-section of the sample after PDMS coating is shown in figure 7. The PDMS thickness observed was 10 ± 2 μm and is homogeneous in both axial and radial direction. The PDMS layer exhibits excellent mechanical stability and was still intact after 400 h time-on-stream.

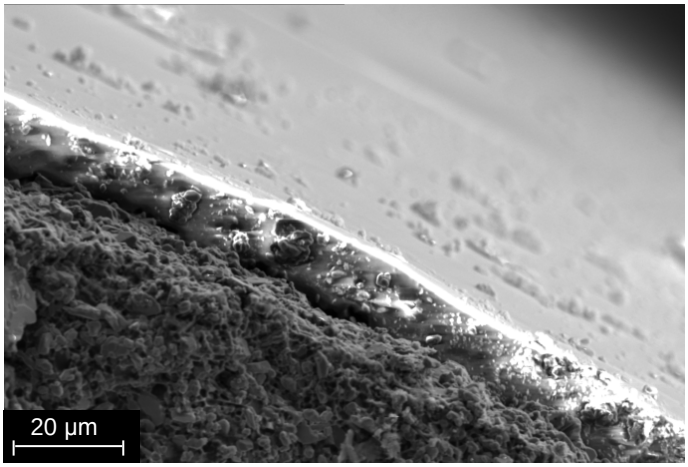

Figure 7: Cross-sectional view of a hollow alumina fibre with CNFs and a 10 µm thick PDMS layer coated on the external surface of the alumina tube.

3.5. Catalytic nitrite hydrogenation

The three reactor layouts described in the experimental section ('H_2 outside', 'H_2 inside' and 'Packed bed') were tested for nitrite hydrogenation. All reactors were synthesized identically and therefore, presented the same properties.

Figure 8 shows that at comparable nitrite conversion levels, 'H_2 outside' layout results in the lowest ammonia selectivity as compared to 'H_2 inside' and 'Packed bed' layouts. The selectivity to ammonia in the 'packed bed' layout remains unchanged when varying the liquid flow rate between 3.0 and 0.4 ml/min, which is equivalent to variation of the weight hourly space velocity (nitrite solution flow weight per hour/ catalyst weight loaded in the reactor, WHSV) between 5.19 and 0.69 h^{-1} (figure 8c and d respectively).

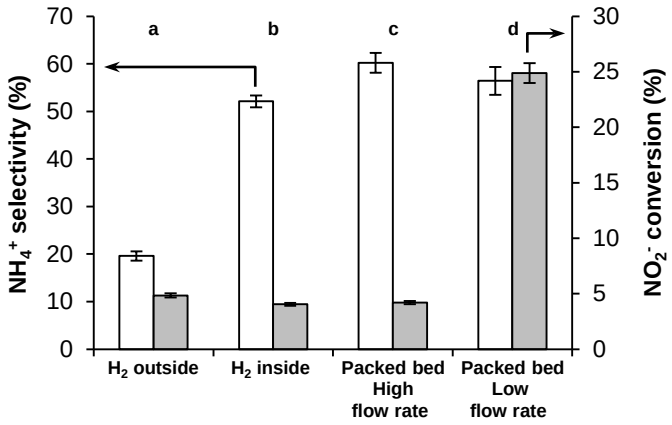

Figure 8: Nitrite conversion and ammonia selectivity of 'H_2 outside', 'H_2 inside' and 'Packed bed' layouts. a) H_2 pressure 0.2 bar, liquid flow rate 0.2 ml/min, catalyst loading 0.011 g_{Pd}/g_{CNF}, b) H_2 concentration 780 μmol H_2/L (pre-saturated at 1 bar), liquid flow rate 0.2 ml/min, catalyst loading 0.011 g_{Pd}/g_{CNF}, c) H_2 concentration 780 μmol H_2/L (pre-saturated at 1 bar), liquid flow rate 3.0 ml/min, catalyst loading 0.011 g_{Pd}/g_{CNF}, d) H_2 concentration 780 μmol H_2/L (pre-saturated at 1 bar), liquid flow rate ml/min, catalyst loading 0.011 g_{Pd}/g_{CNF}.

Figure 9 presents the influence of the hydrogen concentration in the gas feed for the 'H_2 outside' layout. WHSV as well as nitrite concentration were kept constant. The nitrite conversion level hardly changes with hydrogen concentration, except at low concentrations, whereas selectivity to ammonia strongly increases with increasing hydrogen pressure throughout the concentration window.

Figure 10 shows that ammonia selectivity decreases with increasing nitrite concentration keeping hydrogen concentration constant. Note that these experiments were performed under different flow rates, attempting to keep the nitrite conversion level as constant as possible, close to differential conditions.

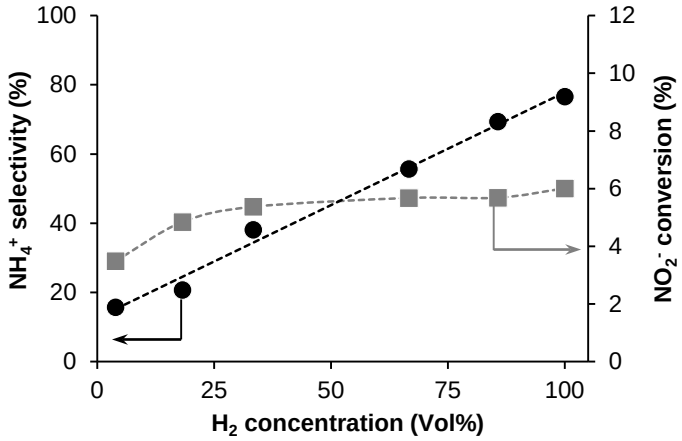

Figure 9: Nitrite conversion and ammonia selectivity of the 'H_2 outside' layout at different H_2 concentrations. WHSV (0.35 h^{-1}) and nitrite concentration (220 μmol NO_2^-/L) were kept constant. Notice that the error bars cannot be seen since they are smaller than the data symbols.

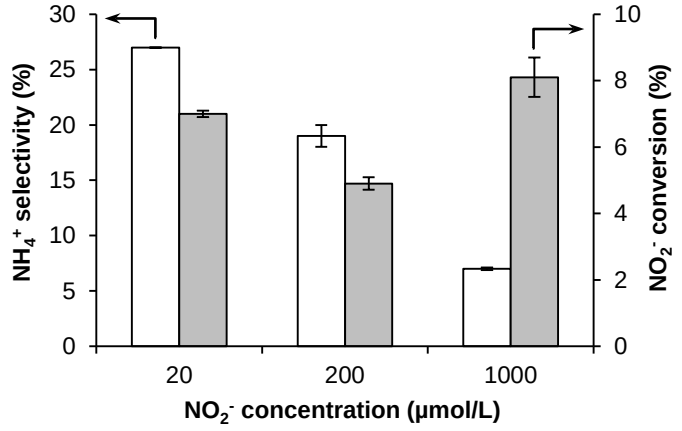

Figure 10: Nitrite conversion and ammonia selectivity of the 'H_2 outside' layout tested at different nitrite concentrations and constant hydrogen partial pressure (0.2 bar). Liquid flow rates were adjusted to obtain similar conversions: a) 1 ml/min, b) 0.2 ml/min and c) 0.1 ml/min.

4. Discussion

4.1. Optimization of the membrane reactor properties

After optimization of the fabrication parameters, it was found that 1.0 g Ni/L, a reduction temperature of 850 °C and a CNF growth temperature of 600 °C lead to the optimum membrane reactor properties. The pore filling obtained indicates that the porosity of the membrane reactor is only 25 vol% less than the porosity of the original alumina fibre while the surface area increased two orders of magnitude (from 0.1 to 16.8 m^2/g). A comparable surface area was obtained by Aran et al. [19] with hollow stainless steel fibres loaded also with CNFs. High pore fillings are detrimental since small pores will completely fill and crack, breaking the internal structure of the alumina fibre [35] and making the reactor more brittle. The CNF morphology and distribution through the material is also crucial. Somewhat thicker CNFs (10 nm) are preferred because these form an open structure with entangled CNFs, whereas thinner CNFs (3-4 nm), as a result of low reduction temperature, form too dense layers of packed CNFs. Confinement of the CNFs inside the alumina wall is preferred to avoid a macroscopic CNF layer at the outer alumina wall that would complicate the coating of a thin and defect free PDMS layer.

4.2. Effect of reactor design on ammonia selectivity

'H_2 outside' layout is more selective towards nitrogen than the other two layouts. It produces almost three times less ammonia at comparable nitrite conversion levels (figure 8). These differences in selectivities are attributed to differences in local concentrations at the palladium active sites.

'H_2 outside' layout operates at lower H/N ratios than the other layouts. The hydrogen partial pressure in the reactor shell is 0.2 bar, corresponding to 156 μmol H_2/L in the liquid according to the hydrogen solubility. However, the actual

hydrogen concentration is even lower because of the diffusion resistance of the PDMS layer for hydrogen transport from the shell to the reaction zone. 'H_2 inside' and 'Packed bed' operate both at 780 μmol H_2/L *via* hydrogen pre-saturation, providing H/N ratios more than five times higher than 'H_2 outside'. Low H/N ratios cannot be achieved with 'H_2 inside' and 'Packed bed' due to hydrogen depletion. Operation at 156 μmol H_2/L, would lead to a maximum nitrite conversion of only 30% and to very low reaction rates as a result of hydrogen depletion.

Figure 9 illustrates that the hydrogen concentration is strongly influencing the selectivity of the reaction. Moreover, figure 10 shows that the nitrite concentration also strongly influences the selectivity. This confirms that the H/N ratio plays a crucial role in determining the selectivity of the reaction. This membrane reactor allows manipulation of this ratio and therefore, to tune the selectivity towards nitrogen.

This agrees well with literature, where it is claimed that by decreasing the H/N ratio, the selectivity towards ammonia can be decreased [27-29, 37, 38]. This can be easily understood, based on the stoichiometry of the reactions to nitrogen and ammonia (equations 3 and 4 respectively), indicating that more hydrogen is needed to form ammonia as compared to nitrogen.

$$2NO_2^- + 3H_2 + 2H^+ \xrightarrow{Pd} N_2 + 4H_2O \qquad \text{Equation 3}$$

$$NO_2^- + 3H_2 + 2H^+ \xrightarrow{Pd} NH_4^+ + 2H_2O \qquad \text{Equation 4}$$

A similar reactor concept was tried by Aran et al. [18] who used a hollow alumina fibre with an internal hydrophilic γ-Al_2O_3 layer in contact with a nitrite solution and an external hydrophobic α-Al_2O_3 layer in contact with the gas, acting as membrane. Although the authors varied the hydrogen concentration from 5% to 100%, no significant difference in ammonia formation was observed under similar experimental conditions. This is attributed to the almost inexistent diffusion resistance at the gas-liquid interface at the non-wetting hydrophobic α-Al_2O_3

macropores. The high diffusivity coefficient of hydrogen in gas phase (typically 1 cm^2/s) [39] allows easy access of hydrogen to the reaction zone for all tested conditions. Instead, the low diffusivity coefficient of hydrogen in PDMS (close to 10^{-4} cm^2/s) [40] creates a higher gas diffusion resistance making the selectivity more sensitive to changes in hydrogen concentration. In another attempt by Aran et al. [19], a porous stainless steel hollow fibre was used, partially filled with CNFs, covered with a PDMS membrane, very similar to this work. Unfortunately, results cannot be compared because the performance of the reactor of Aran et al. [19] was importantly influenced by stoichiometric conversion of nitrite by iron particles, which formed during CNF synthesis on stainless steel.

4.3. Activity and hydrogen reaction order for 'H_2 outside'

Although the change in selectivity is remarkably pronounced when varying the hydrogen concentration, the activity remains almost the same, especially in the range 20-100% H_2 (figure 9). This means that the hydrogen concentration influences selectivity much more than the reaction rate. The small variation in nitrite conversion when varying the hydrogen concentration indicates a low apparent reaction order for hydrogen (0.3, figure A5, Appendix A). It should be noted that this is indeed just an apparent order because concentration gradients through the wall of the membrane reactor, as schematically shown in figure 11, will influence the apparent kinetics significantly. This will be discussed in detail in chapter 4. Nevertheless, similar low reaction orders are reported in literature for Pd-Cu/C [38] and Pd-CNF-Ni foam ('hairy' foam) [29]. Even zero-order is reported for Pd on carbon cloth [41].

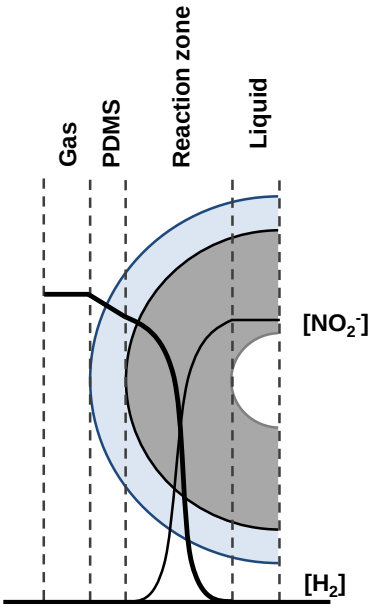

Figure 11: Qualitative nitrite and hydrogen profiles through the wall of the membrane reactor during nitrite hydrogenation.

4.4. Performance of 'Packed bed'

'H_2 outside' layout exhibits the same reaction rate than 'H_2 inside' but much lower than 'Packed bed'. Table 2 shows that 'Packed bed' layout has a much higher weight hourly space velocity (WHSV) than 'H_2 outside' and 'H_2 inside' when all the layouts present the same nitrite conversion (4-5%). The two experiments performed with the 'Packed bed' layout showed that at low liquid flow rate (high nitrite conversion) the reaction rate is lower than at high liquid flow rate (low nitrite conversion). This is probably caused by a deviation from differential conditions, where at higher nitrite conversion, averaged nitrite and hydrogen concentrations decrease, generating lower rates.

The difference in reaction rate between 'Packed bed' and the other layouts could be caused by a significant by-passing of the reactants in the 'H_2 inside' and 'H_2

outside' layouts. The low flow rates used for the experiments result in a laminar flow (Reynolds number is 283). Obviously, this will result in much more tunnelling of the liquid feed resulting in a low interaction with the catalyst as compared to a packed bed geometry. Furthermore, the geometrical surface area between liquid and solid is lower for 'H_2 outside' and 'H_2 inside' than for 'Packed bed'. The 0.5 mm particles in the 'Packed bed' layout create an external contact area one order of magnitude higher than the inner alumina wall of 'H_2 outside' and 'H_2 inside' layouts.

Table 2: Nitrite conversion, WHSV and reaction rate for the experiments shown in figure 8; note that the amount of Pd is identical in all three cases.

	H_2 outside	H_2 inside	Packed bed (1)	Packed bed (2)
Nitrite conversion (%)	4.8	4.1	4.2	24.9
WHSV (h^{-1})	0.35	0.35	5.19	0.69
Reaction rate (mmol/min)	2.1×10^{-6}	1.8×10^{-6}	2.7×10^{-5}	2.2×10^{-5}

Assuming some internal mass transfer limitations for all three layouts (Weisz-Prater criterion (C_{WP}) for hydrogen and nitrite are 0.6 and 1.5 respectively for the 'Packed bed' layout at high liquid flow rate; equation B1, Appendix B), this increase in geometrical surface area will offer a larger fraction of accessible catalyst and therefore, higher activity. The relatively low C_{WP} are caused by the low amount of palladium catalyst (0.08 wt%Pd).

'H_2 inside' and 'Packed bed' present the same high ammonia selectivity since both operate at the same high H/N ratio. The ammonia selectivity seems independent of the nitrite conversion level in the 5-25% range (figure 8c and d) confirming that consecutive reactions are not involved.

5. Conclusions

A membrane reactor that allows low and homogeneous hydrogen concentrations in the axial direction has been successfully synthesized. Experimental variables of

nickel deposition and CNF growth were optimized, allowing manipulation of the selectivity in nitrite hydrogenation by establishing a low concentration of adsorbed hydrogen at the active sites. A comparison of different reactor layouts proved that this membrane reactor is 2-3 times more selective towards nitrogen, the desired product, at identical nitrite conversion levels. This membrane reactor shows that it is possible to manipulate the selectivity towards nitrogen, the desired product.

6. References

1. Gavriilidis, A., Angeli, P., Cao, E., Yeong, K.K., and Wan, Y.S.S., *Technology and Applications of Microengineered Reactors.* Chemical Engineering Research and Design, 2002. 80(1): p. 3-30.
2. Jensen, K.F., *Microreaction engineering — is small better?* Chemical Engineering Science, 2001. 56(2): p. 293-303.
3. Doku, G.N., Verboom, W., Reinhoudt, D.N., and van den Berg, A., *On-microchip multiphase chemistry—a review of microreactor design principles and reagent contacting modes.* Tetrahedron, 2005. 61(11): p. 2733-2742.
4. Mills, P.L., Quiram, D.J., and Ryley, J.F., *Microreactor technology and process miniaturization for catalytic reactions—A perspective on recent developments and emerging technologies.* Chemical Engineering Science, 2007. 62(24): p. 6992-7010.
5. Chen, G., Yue, J., and Yuan, Q., *Gas-Liquid Microreaction Technology: Recent Developments and Future Challenges.* Chinese Journal of Chemical Engineering, 2008. 16(5): p. 663-669.
6. Hessel, V., Angeli, P., Gavriilidis, A., and Löwe, H., *Gas−Liquid and Gas−Liquid−Solid Microstructured Reactors: Contacting Principles and Applications.* Industrial & Engineering Chemistry Research, 2005. 44(25): p. 9750-9769.
7. Kashid, M.N. and Kiwi-Minsker, L., *Microstructured Reactors for Multiphase Reactions: State of the Art.* Industrial & Engineering Chemistry Research, 2009. 48(14): p. 6465-6485.
8. Aran, H.C., *Porous ceramic and metallic microreactors*, in *SFI*. 2011, University of Twente: Enschede. p. 126.
9. Biardi, G. and Baldi, G., *Three-phase catalytic reactors.* Catalysis Today, 1999. 52(2–3): p. 223-234.
10. Sirkar, K.K., Shanbhag, P.V., and Kovvali, A.S., *Membrane in a Reactor: A Functional Perspective.* Industrial & Engineering Chemistry Research, 1999. 38(10): p. 3715-3737.
11. Dittmeyer, R., Höllein, V., and Daub, K., *Membrane reactors for hydrogenation and dehydrogenation processes based on supported palladium.* Journal of Molecular Catalysis A: Chemical, 2001. 173(1–2): p. 135-184.

12. Huuhtanen, M., Seelam, P.K., Kolli, T., Turpeinen, E., and Keiski, R.L., *Advances in catalysts for membrane reactors.* 2013: p. 401-432.
13. Mota, S., Miachon, S., Volta, J.C., and Dalmon, J.A., *Membrane reactor for selective oxidation of butane to maleic anhydride.* Catalysis Today, 2001. 67(1–3): p. 169-176.
14. Dittmeyer, R., Svajda, K., and Reif, M., *A Review of Catalytic Membrane Layers for Gas/Liquid Reactions.* Topics in Catalysis, 2004. 29(1-2): p. 3-27.
15. Julbe, A., Farrusseng, D., and Guizard, C., *Porous ceramic membranes for catalytic reactors — overview and new ideas.* Journal of Membrane Science, 2001. 181(1): p. 3-20.
16. Vospernik, M., Pintar, A., Berčič, G., Batista, J., and Levec, J., *Potentials of Ceramic Membranes as Catalytic Three-Phase Reactors.* Chemical Engineering Research and Design, 2004. 82(5): p. 659-666.
17. Vospernik, M., Pintar, A., Berčič, G., and Levec, J., *Experimental verification of ceramic membrane potentials for supporting three-phase catalytic reactions.* Journal of Membrane Science, 2003. 223(1-2): p. 157-169.
18. Aran, H.C., Chinthaginjala, J.K., Groote, R., Roelofs, T., Lefferts, L., Wessling, M., and Lammertink, R.G.H., *Porous ceramic mesoreactors: A new approach for gas-liquid contacting in multiphase microreaction technology.* Chemical Engineering Journal, 2011. 169(1-3): p. 239-246.
19. Aran, H.C., Pacheco Benito, S., Luiten-Olieman, M.W.J., Er, S., Wessling, M., Lefferts, L., Benes, N.E., and Lammertink, R.G.H., *Carbon nanofibers in catalytic membrane microreactors.* Journal of Membrane Science, 2011. 381(1–2): p. 244-250.
20. Pintar, A., Berčič, G., and Levec, J., *Catalytic liquid-phase nitrite reduction: Kinetics and catalyst deactivation.* AIChE Journal, 1998. 44(10): p. 2280-2292.
21. Pintar, A., *Catalytic processes for the purification of drinking water and industrial effluents.* Catalysis Today, 2003. 77(4): p. 451-465.
22. Shuai, D., Choe, J.K., Shapley, J.R., and Werth, C.J., *Enhanced Activity and Selectivity of Carbon Nanofiber Supported Pd Catalysts for Nitrite Reduction.* Environmental Science & Technology, 2012. 46(5): p. 2847-2855.
23. Hörold, S., Vorlop, K.D., Tacke, T., and Sell, M., *Development of catalysts for a selective nitrate and nitrite removal from drinking water.* Catalysis Today, 1993. 17(1–2): p. 21-30.

24. D'Arino, M., Pinna, F., and Strukul, G., *Nitrate and nitrite hydrogenation with Pd and Pt/SnO2 catalysts: the effect of the support porosity and the role of carbon dioxide in the control of selectivity.* Applied Catalysis B: Environmental, 2004. 53(3): p. 161-168.
25. Devard, A., Ulla, M.A., and Marchesini, F.A., *Synthesis of Pd/Al2O3 coating onto a cordierite monolith and its application to nitrite reduction in water.* Catalysis Communications, 2013. 34: p. 26-29.
26. Barrabés, N. and Sá, J., *Catalytic nitrate removal from water, past, present and future perspectives.* Applied Catalysis B: Environmental, 2011. 104(1-2): p. 1-5.
27. Franch, C., Lammertink, R.G.H., and Lefferts, L., *Partially hydrophobized catalyst particles for aqueous nitrite hydrogenation.* Applied Catalysis B: Environmental, 2014. 156-157: p. 166-172.
28. Ebbesen, S.D., Mojet, B.L., and Lefferts, L., *Effect of pH on the Nitrite Hydrogenation Mechanism over Pd/Al2O3 and Pt/Al2O3: Details Obtained with ATR-IR Spectroscopy.* The Journal of Physical Chemistry C, 2011. 115(4): p. 1186-1194.
29. Chinthaginjala, J.K. and Lefferts, L., *Support effect on selectivity of nitrite reduction in water.* Applied Catalysis B: Environmental, 2010. 101(1-2): p. 144-149.
30. Wada, K., Hirata, T., Hosokawa, S., Iwamoto, S., and Inoue, M., *Effect of supports on Pd–Cu bimetallic catalysts for nitrate and nitrite reduction in water.* Catalysis Today, 2012. 185(1): p. 81-87.
31. Strukul, G., Gavagnin, R., Pinna, F., Modaferri, E., Perathoner, S., Centi, G., Marella, M., and Tomaselli, M., *Use of palladium based catalysts in the hydrogenation of nitrates in drinking water: from powders to membranes.* Catalysis Today, 2000. 55(1–2): p. 139-149.
32. Ilinitch, O.M., Cuperus, F.P., Nosova, L.V., and Gribov, E.N., *Catalytic membrane in reduction of aqueous nitrates: operational principles and catalytic performance.* Catalysis Today, 2000. 56(1–3): p. 137-145.
33. Lüdtke, K., Peinemann, K.-V., Kasche, V., and Behling, R.-D., *Nitrate removal of drinking water by means of catalytically active membranes.* Journal of Membrane Science, 1998. 151(1): p. 3-11.
34. Sander, R., *Compilation of Henry's law constants (version 4.0) for water as solvent.* Atmospheric Chemistry and Physics, 2015. 15(8): p. 4399-4981.

35. Jarrah, N.A., van Ommen, J.G., and Lefferts, L., *Growing a carbon nano-fibre layer on a monolith support; effect of nickel loading and growth conditions.* Journal of Materials Chemistry, 2004. 14(10): p. 1590.
36. Derbyshire, F.J., Presland, A.E.B., and Trimm, D.L., *Graphite formation by the dissolution—precipitation of carbon in cobalt, nickel and iron.* Carbon, 1975. 13(2): p. 111-113.
37. Hörold, S., Tacke, T., and Vorlop, K.-D., *Catalytical removal of nitrate and nitrite from drinking water: 1. Screening for hydrogenation catalysts and influence of reaction conditions on activity and selectivity.* Environmental Technology, 1993. 14(10): p. 931-939.
38. Mikami, I., Sakamoto, Y., Yoshinaga, Y., and Okuhara, T., *Kinetic and adsorption studies on the hydrogenation of nitrate and nitrite in water using Pd-Cu on active carbon support.* Applied Catalysis B: Environmental, 2003. 44(1): p. 79-86.
39. Marrero, T.R. and Mason, E.A., *Gaseous Diffusion Coefficients.* Journal of Physical and Chemical Reference Data, 1972. 1(1): p. 3-118.
40. Sadrzadeh, M., Shahidi, K., and Mohammadi, T., *Effect of operating parameters on pure and mixed gas permeation properties of a synthesized composite PDMS/PA membrane.* Journal of Membrane Science, 2009. 342(1–2): p. 327-340.
41. Matatov-Meytal, Y., *Cloth catalysts in water denitrification III. pH inhibition of nitrite hydrogenation over Pd/ACC.* Applied Catalysis B: Environmental, 2003. 45(2): p. 127-134.

Appendix A: Figures and graphs

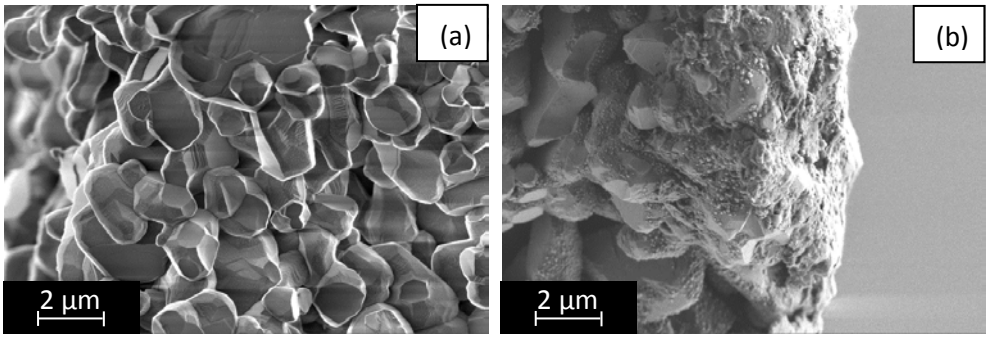

Figure A1: Cross-sectional view of the a) inner wall and b) outer wall of the sample prepared with 1.0 g_{Ni}/L, reduced at 850 °C and with CNFs grown at 350 °C. Only the outer wall presents a layer of amorphous carbon.

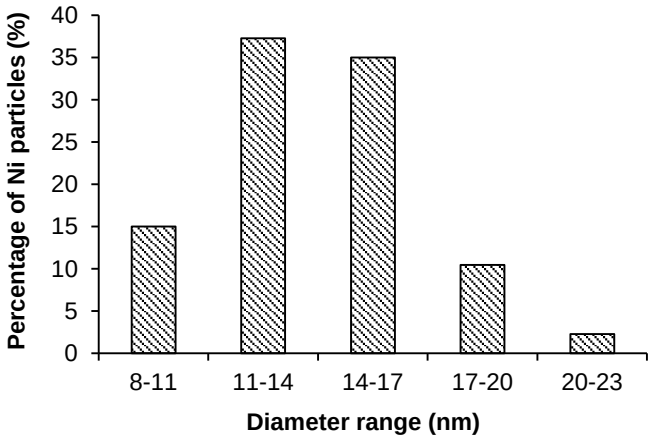

Figure A2: Nickel particle size distribution on the alumina hollow fibre after using 1.0 g_{Ni}/L and a reduction temperature of 850 °C.

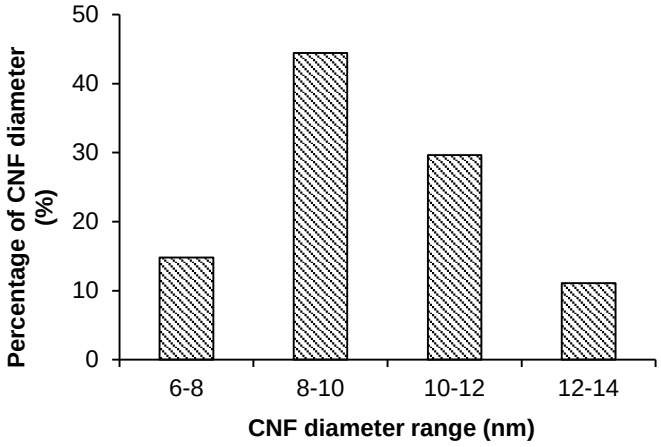

Figure A3: CNF diameter distribution on the alumina hollow fibre after using 1.0 g_{Ni}/L, a reduction temperature of 850 °C and a CNF growth temperature of 600 °C.

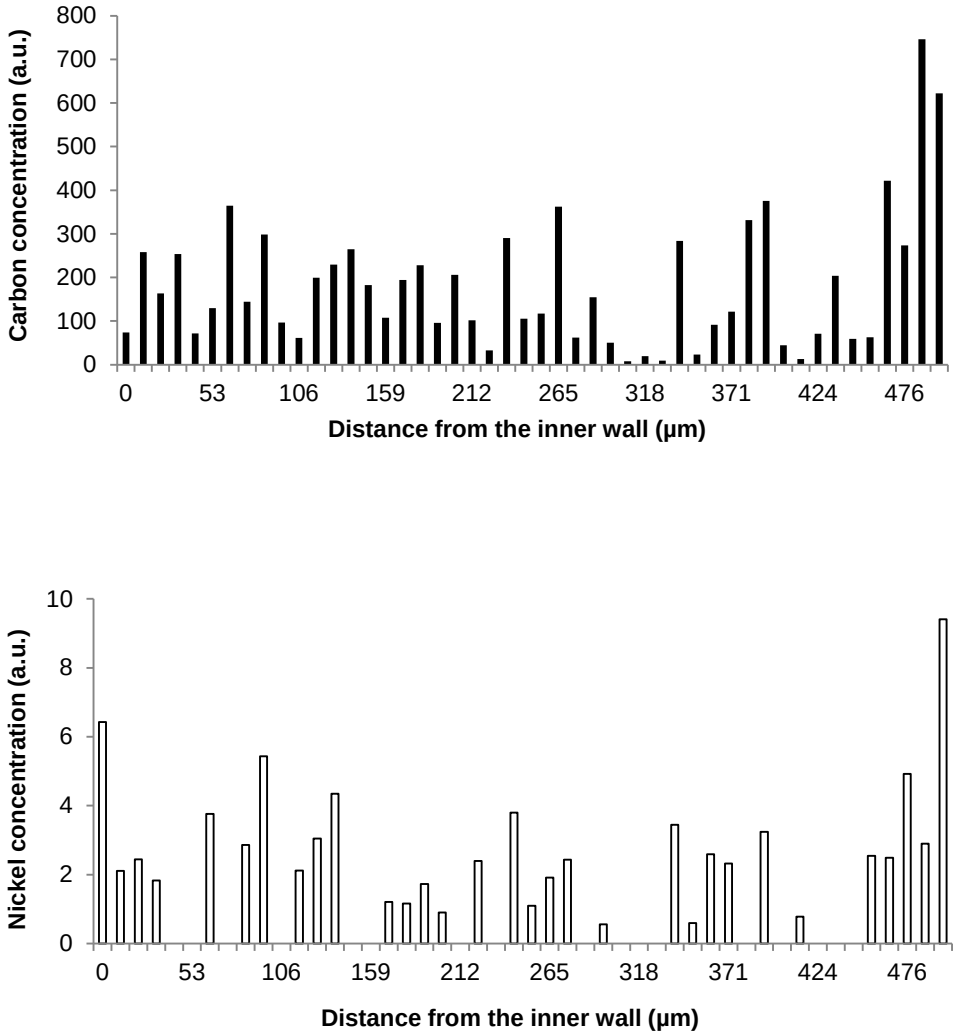

Figure A4: EDX measurements on a membrane cross-section for a) carbon distribution through the wall, b) nickel distribution through the wall. Scatter is caused by the roughness of the surface of the cross-section.

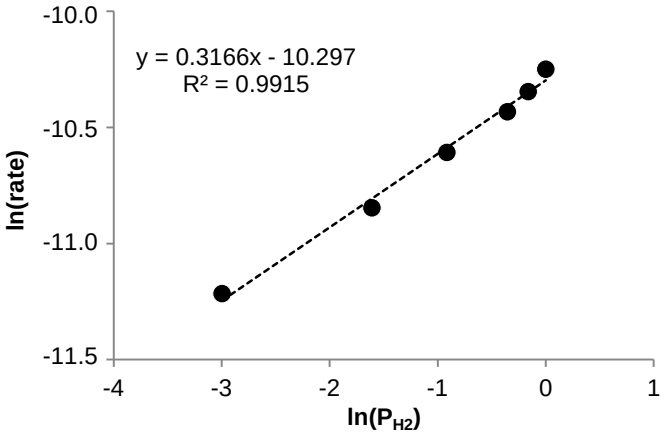

Figure A5: Effect of hydrogen partial pressure on the reaction rate. The slope of the regression line indicates a hydrogen partial reaction order of 0.3.

Appendix B: Weisz-Prater criterion (C_{wp})

C_{wp} was calculated for the 'Packed bed' layout (high flow rate) to estimate the presence of internal mass transfer limitations (equation 5). r_{obs} is the observed reaction rate (mol/(g_{cat}*s)). It was calculated from the liquid flow rate (0.4 ml/min), the average reactant concentration in the catalyst bed (210 μmolNO_2^-/L, 770 μmolH_2/L), the conversion (4.2 wt%NO_2^- and 2.8 wt%H_2) and the amount of supported catalyst (0.43 g). ϱ_P is the bulk density of the α-Al_2O_3 with the grown CNFs inside the alumina macropores (g/cm³). It was calculated from the porosity (0.34) and density (2.6 g/cm³) of the alumina and from the density (2.15 g/cm³) and amount of CNFs (7.5 wt%). R_p is the radius of the supported catalyst particles (0.025 cm). D_{AB} is the molecular diffusivity of nitrite ($1.91 * 10^{-5}$ cm²/s) or hydrogen ($5.11 * 10^{-5}$ cm²/s) in water (cm²/s). ε and τ are the total porosity and tortuosity respectively. The total porosity was calculated from the alumina porosity (0.34) and the density (2.15 g/cm³) and amount of CNFs (7.5 wt%). The total tortuosity was defined as 2, assuming that the presence of CNFs will not affect severely the tortuosity of the system since they offer an open structure. C_A is the reactant concentration (mol/cm³). For $C_{wp} << 1$, internal mass transfer limitations can be excluded while for $C_{wp} >> 1$, mass transfer limitations become significant and pronounced concentration gradients are stablished inside the catalyst particles. For C_{wp} values close to 1, mass transfer limitations cannot be excluded but are not dominant neither.

$$C_{wp} = \frac{r_{obs} * \rho_p * {R_p}^2}{\frac{\varepsilon * D_{AB}}{\tau} * C_A}$$ Equation B1

Chapter 3

Egg-shell membrane reactors for nitrite hydrogenation: manipulating kinetics and selectivity

Chapter published as:

Brunet Espinosa, R.; Rafieian, D.; Postma, R.S.; Lammertink R.G.H and Lefferts, L.; Egg-shell membrane reactors for nitrite hydrogenation: manipulating kinetics and selectivity (submitted to Applied Catalysis B: Environmental journal).

Abstract

A method to fabricate egg-shell α-alumina membrane reactors has been developed, allowing excellent control over the distribution of the active phase through the wall of the alumina tube. The performance of these membrane reactors has been assessed for nitrite hydrogenation. We have shown that manipulation of the thickness of the zone containing active phase induces different diffusion lengths for nitrite and hydrogen, strongly influencing activity and selectivity. Thick active layers have proven to be more selective to nitrogen, the desired product for purification of drinking water. Surprisingly, a thick layer with active phase also induces a negative apparent order in hydrogen, which is tentatively assigned to the fact that the ratio of nitrite and hydrogen concentrations varies extremely in the active zone.

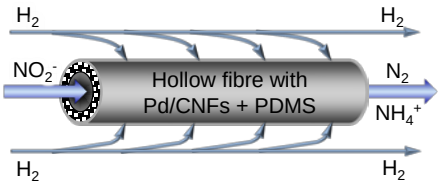

Flow operation

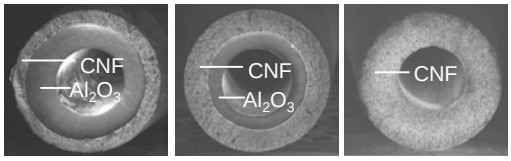

Different egg-shell membrane reactors

1. Introduction

The use of three phase catalytic reactors is very relevant in the chemical industry for heterogeneously catalysed reactions with reactants and/or products in both gas- and liquid-phase [1-4]. Conventional multiphase reactors comprise slurry reactors, *i.e.* stirred tanks or bubble columns, as well as packed bed trickle-phase reactors [4-8]. The most common problems encountered with slurry reactors concerns the filtration section which is expensive and not very robust, since *e.g.* attrition of the catalyst particles creates fines that are difficult to separate from the liquid [4]. Packed bed trickle-phase reactors usually suffer from internal mass transfer limitations due to the relatively large catalyst support particles (typically larger than 1 mm), necessary to limit the pressure drop. Additionally, the random packing of the catalyst bodies easily results in flow mal-distribution including stagnant zones and by-passes [4, 5, 9]. Structured reactors based on *e.g.* monoliths [9, 10], foams [11-14], and cloth [15, 16] have attracted special attention in the last decades since these circumvent the necessity of filtration combined with short diffusion lengths similar to slurry catalysts. However, these reactors become less suitable when the gas reactant solubility is low and/or high gas consumption is required.

Membrane reactors are an interesting alternative for multiphase reactions. One of their main advantages is the well-defined gas-liquid interface where gas and liquid meet and react on the catalyst surface. Since gas and liquid streams are fed from opposite sides of the membrane, operating with these reactors provides an independent control of both phases [6, 17-22]. Many reviews have been published attempting to describe and classify them. The most commonly used classification is based on the role of the membrane and is divided in three categories, namely extractor, contactor and distributor [20, 21, 23]. Extractors are used to increase the reaction rate of consecutive reactions or reactions that are equilibrium-restricted, by selectively extracting one of the products through the membrane. Contactors promote a good contact between the catalyst and the reactant *via* the use of catalytically active membranes. Distributors are used to control the dispersion of

one of the reactants to the reaction zone avoiding variations in concentration in the axial direction of the reactor. This becomes relevant for reactions with selectivities strongly influenced by the concentration of one of the reactants, *e.g.* nitrite hydrogenation [24] or for reactions that present flammable mixtures [20].

The major disadvantage of membrane reactors is the mass transfer limitations in the liquid phase caused by the laminar regimes of the liquid stream. Recent work carried by Pashkova et al. [25] and Vospernik et al. [26] showed how to reduce mass transfer limitations in the liquid channel by introducing glass beads or a static mixer inside the membrane tube. A different approach to minimize the transport limitations of the liquid reactants is miniaturizing the membrane reactor by decreasing its diffusion length [1, 27].

Nitrite hydrogenation was used as a model reaction to assess the performance of micro-membrane reactors. Nitrate is a common inorganic contaminant that can be found even in drinking water. In the human body, it can easily convert to nitrite, creating health endangerment *via* methemoglobinemia (blue baby syndrome) or *via* formation of some carcinogenic nitrosamines [4, 28, 29]. Catalytic hydrogenation is a very promising technique to eliminate nitrate and nitrite from drinking water since it can convert these inorganic contaminants into harmless nitrogen. However, avoiding the formation of the undesired by-product ammonia still presents a challenge. It is known that the selectivity of the nitrite hydrogenation is strongly influenced by the H/N of reaction intermediates on the catalyst surface [30-34]. Therefore the selectivity of the nitrite hydrogenation can be manipulated by controlling the reactant transport which will determine the concentration of the reactants near the catalyst surface.

In this work, we present the fabrication of three different α-alumina (α-Al_2O_3) membrane reactors with carbon nano-fibres (CNFs) and we discuss their catalytic performance in the nitrite hydrogenation using palladium as catalyst. In chapter 2 we have shown that the selectivity of the reaction benefits from the use of these membrane reactors as compared with different reactor configurations where

hydrogen and nitrite are fed together to the reaction zone. Basically, membrane reactors allow decreasing the H/N ratio in the reaction zone *via* hydrogen dosing through the membrane, resulting in higher nitrogen selectivities. The membrane reactors used in chapter 2 contained CNFs and palladium distributed throughout the α-Al_2O_3 tube. In this chapter, we report on the effect of the distribution of palladium and CNFs inside the wall of the alumina tube. We investigate the activity and selectivity caused by variation of the diffusion lengths of both reactants to the reaction zone.

2. Experimental

2.1. Materials used

Porous ceramic α-Al_2O_3 hollow fibres with a length of 200 mm and an inner and outer diameter of 0.9 and 1.9 mm respectively, were purchased from Hyflux CEPAration Technologies, Europe. They were cut in pieces of 55 mm long to be used as catalyst support and as the skeleton of the reactor. Nickel nitrate hexahydrate (Merck), urea (Merck) and nitric acid (65%, Merck) were used to deposit nickel on the alumina hollow fibres. Ethylene (99.95% PRAXAIR), hydrogen and nitrogen (99.999% INDUGAS) were used to grow CNFs without any further purification. Palladium acetylacetonate (Alfa Aesar) and toluene (>99.9%, Merck) were used to deposited palladium. Toluene (>99.9% Merck) and a two component PDMS (polydimethylsiloxane) RTV 615 kit (permacol B.V.) consisting of a vinyl terminated pre-polymer (RTV-A) and a Pt-catalysed cross-linker (RTV-B) were used for the preparation of the PDMS solution. Sodium nitrite (>99%, Merck) was used as nitrite source for the catalytic tests.

2.2. Fabrication of the reactors

The membrane reactors were synthesized as described in chapter 2. In short, a hollow α-Al_2O_3 fibre was loaded with small nickel particles using nickel

deposition-precipitation technique. Afterwards, CNFs were grown using a quartz tube reactor of 10 mm of inner diameter. The hollow alumina fibre was placed inside the quartz tube and the temperature was raised to 850 °C at 6 °C/min using 100 ml/min of nitrogen gas. After 1 h at 850 °C, a hydrogen/nitrogen mixture (50/50) was fed to the system for 2 h. Next, the temperature was cooled to 600 °C under 80 ml/min of nitrogen gas. The CNF growth was performed at 600 °C under a gas mixture containing 20% ethylene (C_2H_4), 7% H_2, and 73% N_2. Three different CNF growth times were studied: 15, 22.5 and 45 min. Next, the temperature was cooled to room temperature under 80 ml/min of nitrogen gas. Any loose CNFs were removed *via* sonication with miliQ water. After drying the sample, palladium was deposited on the CNFs using palladium acetylacetonate precursor and was then calcined and reduced at 250 °C. In the final step, the outer wall of the alumina fibre was coated with a home-made PDMS membrane. One of the reactors with CNFs grown for 45 min and without PDMS coating was crushed and sieved to a particle size of 125-250 μm.

2.3. Catalytic test

The synthesized membrane reactors were tested using the nitrite hydrogenation reaction under identical conditions. A nitrite solution (44 μmol/L NO_2^-) saturated with argon was introduced inside the tube with a flowrate of 0.05 ml/min, while the shell of the membrane reactor was exposed to a gas mixture containing between 0.02 and 1.0 bar of hydrogen, balanced with argon. In this configuration, hydrogen is allowed to diffuse to the reaction zone through the PDMS membrane located at the outer wall of the reactor. Hydrogen and nitrite meet and react at the palladium particles located at the CNFs.

The crushed reactor without PDMS was tested in a packed bed reactor. A nitrite solution (217 μmol/L NO_2^-) was pre-saturated in different hydrogen partial pressures (0.2, 0.5 and 1.0 bar) and fed to the catalytic bed.

All the tests were conducted at room temperature (20 °C). Nitrite and ammonium (NH_4^+) concentrations were measured at the inlet and outlet of the reactor with an in-line Ion Chromatograph (Dionex, ICS 1000). These values allowed calculating nitrite conversion and ammonia selectivity according to equations 1 and 2 respectively. The solutions were not buffered. Selectivity to nitrogen was calculated based on the mass balance and the fact that exclusively ammonia and nitrogen are formed under these conditions [30, 33, 35].

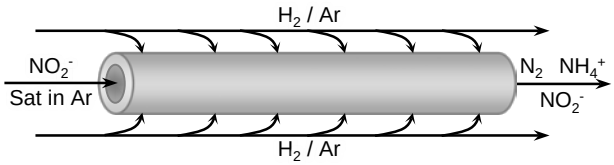

Figure 1: Flow operation of a membrane reactor.

$$NO_2^- \text{ conversion} = \frac{[NO_2^-]_{initial} - [NO_2^-]_{final}}{[NO_2^-]_{initial}} \cdot 100 \qquad \text{Equation 1}$$

$$NH_4^+ \; selectivity = \frac{[NH_4^+]_{final} - [NH_4^+]_{initial}}{[NO_2^-]_{initial} - [NO_2^-]_{final}} \cdot 100 \qquad \text{Equation 2}$$

2.4. Characterization

The BET surface areas of the membrane reactors were determined with N_2-adsorption obtained at 77 K (Micromeritics Tristar) using the BET isotherm. The location and morphology of the CNFs inside the pores in the wall of the membrane reactor as well as the palladium particle size were determined with Scanning Electron Microscopy, HR-SEM (Analysis Zeiss MERLIN HR-SEM). Palladium particle size was determined by averaging 150 measurements on three different positions in the sample. Cross-sections were prepared with the help of a scalpel. The carbon content of the membrane reactor was determined with an analytic balance by weighing the reactor before and after CNF growth. The fraction of the pore volume filled with carbon was estimated based on the amount of CNFs and

the void fraction of the α-Al_2O_3, measured with Hg porosimetry (Quantachrome Poremaster PM33). The palladium loading was determined for every membrane reactor using X-ray fluorescence spectroscopy, XRF (Philips PW 1480).

3. Results

3.1. Sample preparation

The appearance of the external surface of the samples prepared with different growth times (15, 22.5 and 45 min) is very similar, all presenting a fully and homogeneously covered surface. However, noticeable differences can be observed from the cross-sections. Figure 2 shows the location of CNFs through the wall of the alumina fibre after different CNF growth times. After 45 min, the wall is filled with 8.0 wt% CNFs (table 1) throughout the cross-section (Figure 2c). In contrast, shorter growth time results in lower CNF coverage (down to 3.2 wt% for 15 min, table 1), which is caused by preferential filling of the outer zone of the cross-section with CNFs. The thickness of the outer layer containing CNFs is presented in table 1; note that the transition between the zones with and without CNFs is remarkably sharp (figure 2a, 2b, 3a). Figure 2d, e and f show that the apparent density at a fixed location of the CNFs increases with growth time.

Figure 3a shows the interface between the regions with and without CNFs for the 22.5 min sample. Figure 3b depicts the curly and entangled morphology of the CNFs, while figure 3c shows alumina grains in the region without CNFs. These alumina grains contain small nickel particles, confirming that the lack of CNFs is not caused by absence of nickel particles.

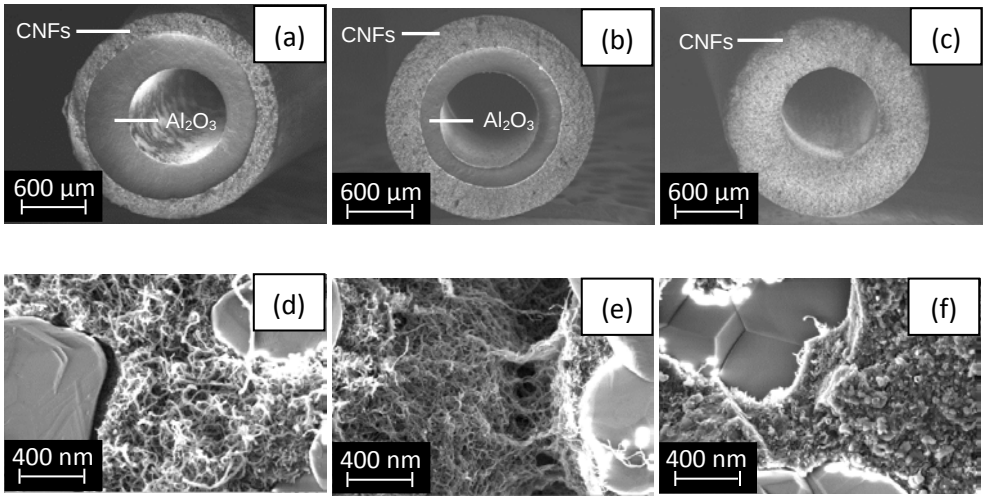

Figure 2: HRSEM pictures of cross-sections of the three membrane reactors with different CNF growth times, a) 15 min, b) 22.5 min and c) 45min. High magnification of the alumina macropores filled with CNFs are shown in d), e) and f) for the samples grown for 15, 22.5 and 45 min respectively.

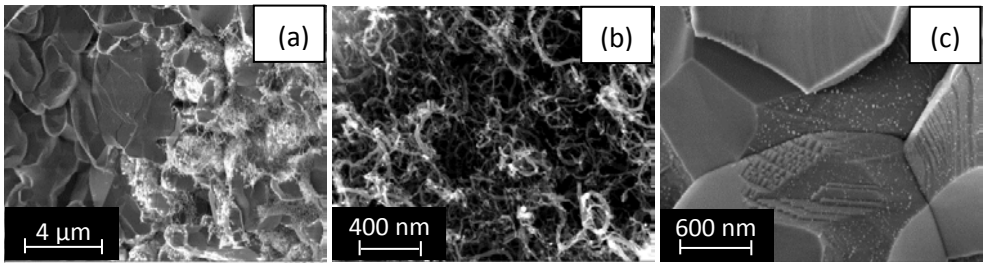

Figure 3: Cross-sectional view of the sample with a CNF growth of 22.5 min, a) interface between CNFs and bare alumina, b) CNF morphology, c) bare alumina grains with nickel particles.

Table 1: Physical properties of the membrane reactors.

CNF thickness (μm)	200	320	500
CNF growth time (min)	15	22.5	45
Carbon percentage (wt%)	3.2	5.5	8.0
Total CNF pore filling (vol%)	11	20	29
CNF pore filling in carbon region (vol%)	24	27	29
Surface area (m^2/g reactor)	6.5	10.1	22.0
Pd loading (g Pd/100 g reactor)	0.045	0.060	0.077
Pd particle size (nm)	8-9	8-9	8-9

Both the BET surface area and the amount of palladium scale with the amount of CNFs present in the alumina wall. Short CNF growth times result in a small amount of CNFs and therefore low surface area as well as low palladium loading. However, the differences in palladium loading are relatively less compared to CNF amount and surface area. The palladium particle size was very similar, typically 8-9 nm, in all the membrane reactors, based on HRSEM (not shown). Because of the low surface area of the α-Al_2O_3, it is expected that the catalytic activity will be dominantly located within the confined CNF regions.

Two different values to determine pore filling are shown in table 1. 'CNF pore filling in carbon region' takes into account exclusively the volume of the alumina pores that actually contain CNFs, while 'total CNF pore filling' represents an averaged value considering the pore volume of the entire alumina tube.

3.2. Catalytic results

Figure 4 shows that the selectivity of the ammonia by-product increases with increasing hydrogen concentration supplied through the PDMS membrane. The thinner the CNF region is, the higher the ammonia selectivity becomes. For example, the sample with a CNF thickness of 200 μm reaches 100% ammonia selectivity with high hydrogen concentrations (50-100%).

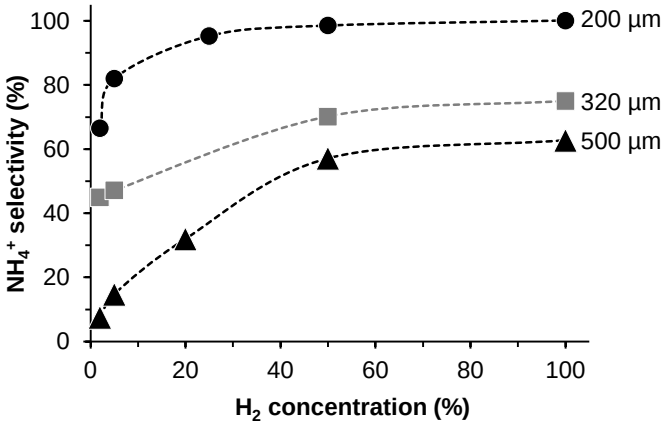

Figure 4: Effect of hydrogen concentration on ammonia selectivity for the membrane reactors with different thickness of the layer filled with CNFs. Experiments were performed with 44 µmol/L nitrite solution with a liquid flow rate of 0.05 ml/min at room temperature.

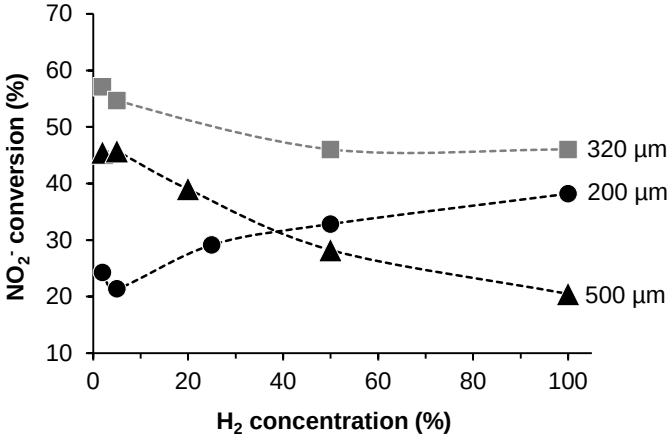

Figure 5: Effect of hydrogen concentration on the nitrite conversion for the membrane reactors with different thickness of the layer filled with CNFs. Experiments were performed with 44 µmol/L nitrite solution with a liquid flow rate of 0.05 ml/min at room temperature.

Figure 5 shows that all three samples present different activities at a given hydrogen concentration. The activity of the samples with CNF thicknesses of 320 and 500 μm decreases when increasing hydrogen concentration. The sample with a CNF thickness of 200 μm presents the opposite behaviour.

The sample with a CNF thickness of 320 μm was also tested at a higher flow rate (0.15 ml/min). Although the conversion decreased down to 25%, the ammonia selectivity remained almost unchanged (from 45% to 41%).

Figure 6 shows that the crushed sample with full CNF coverage (500 μm thickness) shows an increase in catalytic activity and ammonia selectivity when increasing hydrogen concentration. Remarkably, the surprising decrease in activity with hydrogen concentration (figure 5) changes to the opposite trend (Figure 6) by crushing the membrane, which is much more usual.

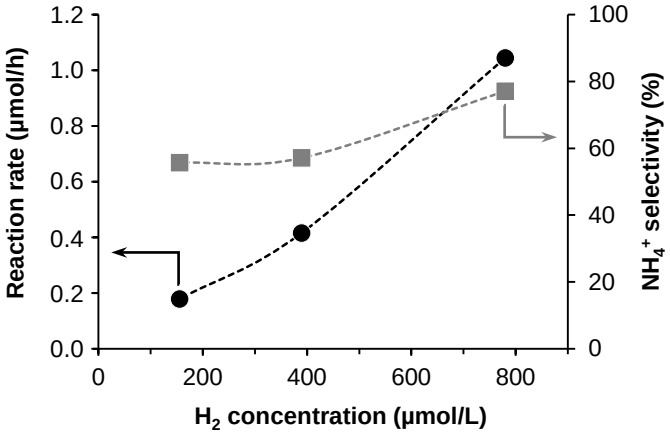

Figure 6: Effect of hydrogen concentration on the reaction rate and the ammonia selectivity for the crushed reactor with full CNF coverage (45min CNF growth). Tests were performed at room temperature with a nitrite solution of 217 μmol/L.

4. Discussion

4.1. Egg-shell catalyst induced by diffusion limitations

CNF growth initiates at the outer shell of the α-Al_2O_3 tube. The zone with CNFs moves to the centre of the tube with increasing growth time, generating egg-shell structures. This is caused by a gas flow resistance inside the alumina tube due to the small diameter of the inner tube (0.9 mm, figure 7); the area of the cross-section of the reactor tube excluding the alumina tube is two orders of magnitude larger (76 mm^2) than the area inside the tube (0.64 mm^2).

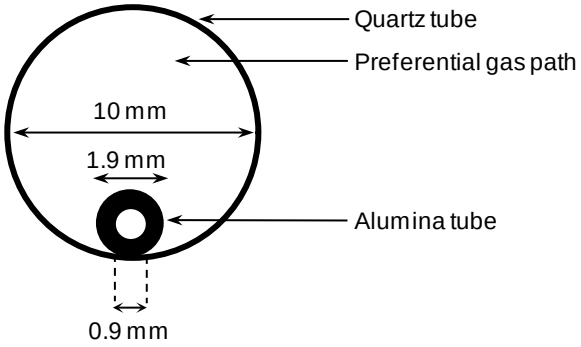

Figure 7: Scheme of the alumina tube inside the quartz reactor during CNF growth. Note that dimensions are not proportional.

Since the gas flow prefers the path with less resistance, the gas mainly flows outside of the alumina tube rather than inside. In other words, the gas inside the alumina tube will be nearly stagnant and the ethylene transport inside the tube will mainly occur *via* molecular diffusion. Therefore, CNFs will grow on the inside wall at both ends of the tube, but only for a typical distance of 2-3 mm due to ethylene exhaustion. The convective gas flow outside of the alumina tube provides reactive gas to the entire outer wall of the alumina. Ethylene and hydrogen diffusing through the outside surface of the alumina tube generate a CNF layer growing from the outside inwards the macropores in the alumina wall. It is well known that nickel particles deactivate during CNF synthesis [36]; figure 8 confirms

the same for this study. Thus, after deactivation of the outer layer, ethylene penetrates deeper in the alumina wall, shifting the zone where CNFs form inwards. Nevertheless, CNFs become more densely packed at longer growth times (23% and 29% of pore volume filled in the CNF region after 15 and 45 min respectively, table 1). Figure 2d, e and f visually confirm that CNFs grown during 45 min appear denser, filling a larger fraction of the alumina macropores. However, the remaining pore volume is still significant (>70%), enabling diffusion of ethylene and hydrogen to the deeper layer *via* the more densely filled outer layer.

The presence of nickel particles near the inner wall of the alumina tube (figure 3c) strongly confirms that the CNF distribution in the alumina tube after 15 and 22.5 min is not due to mal-distribution of nickel particles. Instead, diffusion limitation of ethylene inside the macropores in the wall of the alumina tube is likely responsible. This is further supported by the observation that the alumina tube contains homogeneously distributed CNFs throughout the wall at both outer ends over a distance of typically 3 mm as discussed above. Notice that the outer ends of every sample were removed before catalytic testing to suppress these heterogeneities.

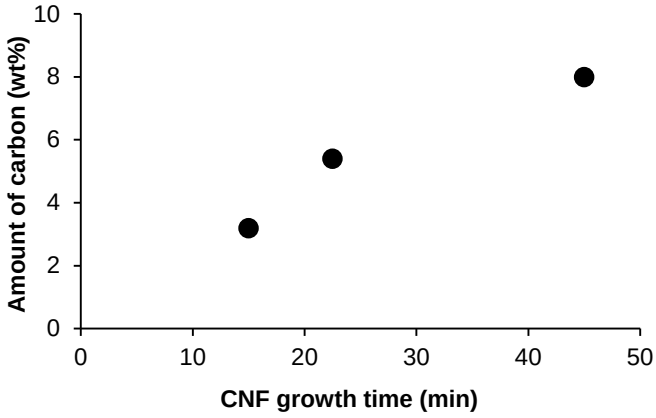

Figure 8: Amount of carbon in the alumina tube when varying the CNF growth time.

4.2. Ammonia selectivity

Ammonia selectivity is strongly influenced by the H/N ratio of reaction intermediates on the surface of the catalyst [30, 33, 34]. High H/N ratios lead to high ammonia selectivities while low ratios favour the formation of nitrogen. Clearly, the selectivity to ammonia increases with increasing hydrogen concentration (Figure 4). In fact, ammonia formation requires three hydrogen molecules per nitrite (equation 4) while formation of nitrogen requires only one and a half (equation 3). Accordingly, low H coverage of the palladium catalyst is needed to suppress ammonia formation. Obviously, an optimum value exists, as too low H-surface coverage would induce very low rates.

$$2NO_2^- + 3H_2 + 2H^+ \xrightarrow{Pd} N_2 + 4H_2O \qquad \text{Equation 3}$$

$$NO_2^- + 3H_2 + 2H^+ \xrightarrow{Pd} NH_4^+ + 2H_2O \qquad \text{Equation 4}$$

Remarkably, all samples present very different selectivities, although all follow the same trend with hydrogen concentration (figure 4). The sample with a CNF thickness of 320 μm was also tested at lower conversion (25%) by increasing the flow rate. It was found that the ammonia selectivity slightly decreased from 45% to 41% when operating with 2% hydrogen concentration. This slight decrease in ammonia selectivity on lowering the conversion is caused by a decrease in pH, as less protons are consumed (equation 3 and 4). As reported in literature [28, 32, 33], low pH values suppress ammonia formation. However, this decrease is minor and cannot explain the differences in selectivity between the three samples. Instead, these differences are attributed to different reactant concentration profiles through the wall of the membrane reactor.

Figure 9 shows qualitatively the profiles of concentrations of hydrogen and nitrite inside the wall of the membrane reactor. As discussed above, the selectivity is controlled by the H/N ratio on the catalyst surface. This ratio varies strongly with the radial position (due to concentration gradients through the wall) as well as along the axial position, as conversion levels are well above differential conditions.

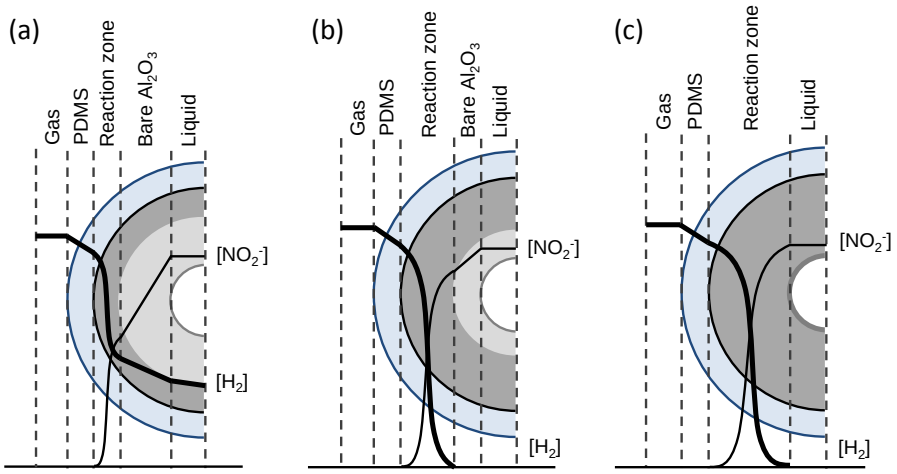

Figure 9: Qualitative concentrations profiles for hydrogen and nitrite inside the wall of the membrane reactor for the three different reactors with CNF thicknesses of a) 200 μm, b) 320 μm and c) 475 μm. The zones correspond to the gas phase, the PDMS membrane, the reaction zone, the bare alumina and the liquid phase in the central channel, all separated by doted lines.

Figure 9a shows that for thin CNF thicknesses (200 μm), nitrite concentration reaching the palladium active sites will be relatively low since the molecular flux through the macropores in the bare alumina zone is inversely proportional to the diffusion distance, *i.e.* the thickness of the bare alumina zone. Clearly, nitrite needs to diffuse through the alumina macropores filled with stagnant water before reaching the region with CNFs and active palladium particles. It was estimated that when operating at 2% hydrogen concentration, the nitrite concentration reaching the reaction zone will decrease by 80% (Appendix C). Additionally, the relatively low nitrite concentration will meet with a relatively high hydrogen concentration since the diffusion distance of hydrogen is short due to the proximity of the CNF layer to the PDMS membrane. Additionally, the PDMS membrane does not induce a significant hydrogen gradient because the membrane is very thin (10-15 μm) and the hydrogen permeability is large (~ 10^{-4} cm^2/s [37]); a concentration

decrease in the order of only 1% was estimated (Appendix C). As a result, a high hydrogen concentration is combined with a low nitrite concentration, leading to high H/N ratios and consequently high selectivity to ammonia.

In contrast, when the CNFs are located throughout the wall of the membrane reactor (figure 9c), nitrite concentration entering the reaction zone is significantly higher than for thin CNF layers. Additionally, the hydrogen flux will be affected by a larger reaction zone and therefore a lower averaged hydrogen concentration is expected. In this scenario, relatively low H/N ratios are expected causing low selectivity to ammonia (figure 4).

Figure 9b (CNF thickness of 320 μm) depicts an intermediate situation between figure 9a and c. Nitrite concentration entering the reaction zone will be higher than in figure 9a but lower than in figure 9c. On the other hand, the average hydrogen concentration in the reaction zone will be higher than in figure 9c but lower than in figure 9a. This will lead to intermediate values of both the H/N as well as the ammonia selectivity (figure 4).

Ideally, to minimize the formation of ammonia, the location of the CNFs should be closer to the inner wall rather than to the outer wall of the membrane reactor. However, this could not be achieved since CNFs start growing from the reactor shell. Future work will focus on the synthesis of a reactor that presents the active phase near the liquid stream. An option that is being explored is using a CNF layer at the outer surface (15 min of CNF growth) combined with a PDMS membrane at the inner surface. In this configuration, the liquid flow would be fed to the reactor shell and the hydrogen gas stream to the inner tube. Alternatively, a thicker PDMS membrane can be coated to further increase the resistance to hydrogen diffusion.

4.3. Catalytic activity

The difference in activity for the three different membrane reactors (figure 5) is also determined by the concentration gradients of the reactants inside the reaction zone.

The reaction rate per mol palladium (figure 10) shows that the minor variations in palladium loading (table 1) are not responsible for this difference in activity. It should be noted that the palladium particle size was also constant.

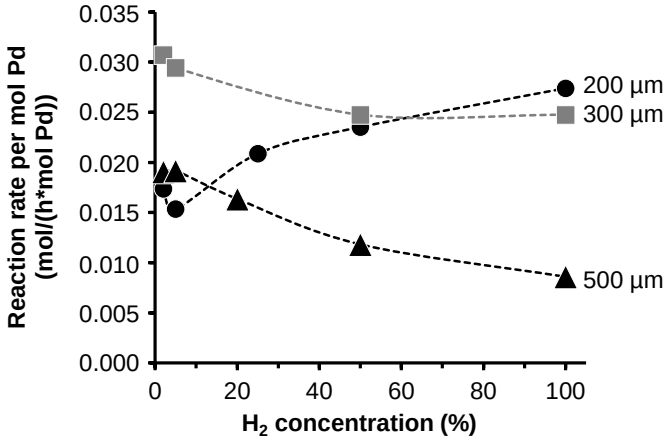

Figure 10: Average reaction rate of nitrite per mol of palladium as a function of hydrogen concentration.

Surprisingly, hydrogen concentration shows quite different effects on catalyst activity in the three reactors. Figures 5 and 10 show that the samples with CNF thickness of 320 and 500 µm are negatively affected by increasing hydrogen concentration, while the activity of the sample with a CNF thickness of 200 µm clearly benefits from an increase in hydrogen concentration, as would be expected. In other words, the apparent order in hydrogen is negative for the thicker CNF layers. This effect is clearly caused by the design of the membrane reactor and certainly not by the catalyst itself because a crushed reactor, operated as fixed bed, shows a positive apparent order in hydrogen (Figure 6), in agreement with literature [33, 38, 39].

The nitrite concentration in this study is similar to the lowest concentrations applied in the kinetic studies in literature, whereas the hydrogen concentrations are very similar. This would suggest that the kinetic descriptions in literature should also be valid for the conditions applied in this study, as temperature and

pH are similar as well. However, kinetic experiment in conventional reactors have in common that concentration gradients in the catalyst particles, if any, can be qualitatively described as in figure 11a, quite different for the membrane reactor presented in figure 11b. Clearly, the ratio hydrogen/nitrite varies in a much wider window in the membrane reactors than in catalyst particles, not only because the diffusion distance in the membrane is larger, but especially because the profiles are opposite instead of parallel in catalyst particles. In other words, in the membrane reactor, some of the palladium particles are exposed to extremely low hydrogen concentration in combination with usual nitrite concentration, as well as at the same time the opposite situation occurs at a different position in the catalytic membrane. Consequently, surface coverage of H and nitrite, or any stable N-intermediate surface compound [32, 40] will vary strongly locally; much stronger than in fixed bed or slurry experiments.

It is well known that, assuming a Langmuir-Hinshelwood mechanism [29], surface coverages influence experimental kinetic parameters including reaction orders and activation energies. The apparent order in e.g. hydrogen can become negative in the case of competitive adsorption with nitrite, when the H-surface-coverage would approach 100%. The observation that the reactors with a thick active zone exhibit a negative order in hydrogen, indicates that the performance of these reactors is importantly dominated by the zone in the active layer that is rich in hydrogen and poor in nitrite. In fact, the H/N ratio is apparently extremely high as competitive adsorption and negative order in hydrogen was never reported in studies using catalyst particles, with concentration gradients as in figure 11a. Mimicking the situation in the H-rich zone in the membrane reactor experimentally is apparently not possible as extremely low nitrite concentrations would be required.

Clearly, the reactor with the thin active zone exhibits usual kinetics, *i.e.* a positive order in hydrogen. This may indicate that the concentration gradients do not develop completely, preventing complete exhaustion of the reactants. In addition, the metal loading is lower (see table 1), causing less developed concentration

gradients. A full description of the performance of the membrane reactors would ask for modelling of both radial gradients, as discussed above, as well as axial gradients as the conversion levels are significant. This, however, would require a kinetic description for the full window of concentrations and concentration ratios, which is not available at this time.

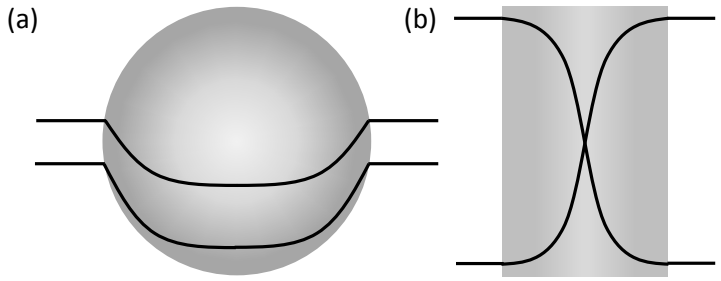

Figure 11: Reactant profiles in a) catalyst particles, b) membrane reactors.

5. Conclusions

Three membrane reactors were fabricated with different well-controlled distributions of the active phase through the alumina wall. Egg-shell distribution of CNFs was obtained due to diffusion limitation of ethylene during CNF growth, diffusing from the outside of the alumina tube towards the inside. As the nickel catalyst particles, responsible for CNF synthesis, deactivate slowly, the reaction front of CNF-growth slowly moves inside the tube of the alumina wall. The diffusion lengths of both nitrite and hydrogen during nitrite hydrogenation are determined by the CNF distribution because palladium is deposited on the CNFs. It was proven that, inducing different concentration gradients of nitrite and hydrogen, the activity and selectivity of nitrite hydrogenation can be manipulated, *i.e.* thicker reactive zones are more selective towards nitrogen. The thicker reactive zones cause exhaustion of hydrogen an especially nitrite, resulting in a negative apparent order in hydrogen.

6. References

1. Aran, H.C., Klooster, H., Jani, J.M., Wessling, M., Lefferts, L., and Lammertink, R.G.H., *Influence of geometrical and operational parameters on the performance of porous catalytic membrane reactors.* Chemical Engineering Journal, 2012. 207–208: p. 814-821.
2. Biardi, G. and Baldi, G., *Three-phase catalytic reactors.* Catalysis Today, 1999. 52(2–3): p. 223-234.
3. Chen, G., Yue, J., and Yuan, Q., *Gas-Liquid Microreaction Technology: Recent Developments and Future Challenges.* Chinese Journal of Chemical Engineering, 2008. 16(5): p. 663-669.
4. Chinthaginjala, J.K., *Hairy foam: Thin layers of carbon nanofibers as catalyst support for liquid phase reactions*, in *CPM*. 2010, University of Twente: Enschede. p. 149.
5. A. Cybulski, J.A.M., *Structured catalysts and reactors*. Second ed, ed. M. Dekker. 2006, New York. 856.
6. Duduković, M.P., Larachi, F., and Mills, P.L., *Multiphase catalytic reactors: a perspective on current knowledge and future trends.* Catalysis Reviews, 2002. 44(1): p. 123-246.
7. P.A. Ramachandran, R.V.C., ed. *Three phase catalytic reactors*. ed. G.a.B.S. publishers. 1983: New York.
8. Satterfield, C.C., *Trickel-bed reactors.* AIChE Journal, 1975. 21(2): p. 209-228.
9. Gascon, J., van Ommen, J.R., Moulijn, J.A., and Kapteijn, F., *Structuring catalyst and reactor – an inviting avenue to process intensification.* Catal. Sci. Technol., 2015. 5(2): p. 807-817.
10. Pangarkar, K., Schildhauer, T.J., van Ommen, J.R., Nijenhuis, J., Kapteijn, F., and Moulijn, J.A., *Structured Packings for Multiphase Catalytic Reactors.* Industrial & Engineering Chemistry Research, 2008. 47(10): p. 3720-3751.
11. Cordier, A., Flahaut, E., Viazzi, C., Laurent, C., and Peigney, A., *In situ CCVD synthesis of carbon nanotubes within a commercial ceramic foam.* Journal of Materials Chemistry, 2005. 15(37): p. 4041.
12. Wenmakers, P.W.A.M., van der Schaaf, J., Kuster, B.F.M., and Schouten, J.C., *"Hairy Foam": carbon nanofibers grown on solid carbon foam. A fully accessible, high surface area, graphitic catalyst support.* Journal of Materials Chemistry, 2008. 18(21): p. 2426-2436.

13. Jarrah, N., van Ommen, J., and Lefferts, L., *Mechanistic aspects of the formation of carbon-nanofibers on the surface of Ni foam: A new microstructured catalyst support.* Journal of Catalysis, 2006. 239(2): p. 460-469.
14. Chinthaginjala, J.K., Bitter, J.H., and Lefferts, L., *Thin layer of carbon-nano-fibres (CNFs) as catalyst support for fast mass transfer in hydrogenation of nitrite.* Applied Catalysis A: General, 2010. 383(1–2): p. 24-32.
15. Cantoro, M., Golovko, V.B., Hofmann, S., Williams, D.R., Ducati, C., Geng, J., Boskovic, B.O., Kleinsorge, B., Jefferson, D.A., Ferrari, A.C., Johnson, B.F.G., and Robertson, J., *Wet catalyst assisted growth of carbon nanofibers on complex three-dimensional substrates.* Diamond and Related Materials, 2005. 14(3–7): p. 733-738.
16. Matatov-Meytal, Y. and Sheintuch, M., *Catalytic fibres and cloths.* Applied Catalysis A: General, 2002. 231(1–2): p. 1-16.
17. Aran, H.C., *Porous ceramic and metallic microreactors*, in *SFI*. 2011, University of Twente: Enschede. p. 126.
18. Julbe, A., Farrusseng, D., and Guizard, C., *Porous ceramic membranes for catalytic reactors — overview and new ideas.* Journal of Membrane Science, 2001. 181(1): p. 3-20.
19. Dittmeyer, R., Svajda, K., and Reif, M., *A Review of Catalytic Membrane Layers for Gas/Liquid Reactions.* Topics in Catalysis, 2004. 29(1-2): p. 3-27.
20. Mota, S., Miachon, S., Volta, J.C., and Dalmon, J.A., *Membrane reactor for selective oxidation of butane to maleic anhydride.* Catalysis Today, 2001. 67(1–3): p. 169-176.
21. Huuhtanen, M., Seelam, P.K., Kolli, T., Turpeinen, E., and Keiski, R.L., *Advances in catalysts for membrane reactors.* 2013: p. 401-432.
22. Dittmeyer, R., Höllein, V., and Daub, K., *Membrane reactors for hydrogenation and dehydrogenation processes based on supported palladium.* Journal of Molecular Catalysis A: Chemical, 2001. 173(1–2): p. 135-184.
23. Miachon, S., Dalmon, J.-A., *Catalysis in membrane reactors: what about the catalyst?* Topics in Catalysis, 2004. 29(1-2): p. 59-65.
24. Aran, H.C., Chinthaginjala, J.K., Groote, R., Roelofs, T., Lefferts, L., Wessling, M., and Lammertink, R.G.H., *Porous ceramic mesoreactors: A new approach for gas-liquid contacting in multiphase microreaction technology.* Chemical Engineering Journal, 2011. 169(1-3): p. 239-246.

25. Pashkova, A., Dittmeyer, R., Kaltenborn, N., and Richter, H., *Experimental study of porous tubular catalytic membranes for direct synthesis of hydrogen peroxide.* Chemical Engineering Journal, 2010. 165(3): p. 924-933.
26. Vospernik, M., Pintar, A., Berčič, G., Batista, J., and Levec, J., *Potentials of Ceramic Membranes as Catalytic Three-Phase Reactors.* Chemical Engineering Research and Design, 2004. 82(5): p. 659-666.
27. Aran, H.C., Pacheco Benito, S., Luiten-Olieman, M.W.J., Er, S., Wessling, M., Lefferts, L., Benes, N.E., and Lammertink, R.G.H., *Carbon nanofibers in catalytic membrane microreactors.* Journal of Membrane Science, 2011. 381(1–2): p. 244-250.
28. Hörold, S., Tacke, T., and Vorlop, K.-D., *Catalytical removal of nitrate and nitrite from drinking water: 1. Screening for hydrogenation catalysts and influence of reaction conditions on activity and selectivity.* Environmental Technology, 1993. 14(10): p. 931-939.
29. Pintar, A., Berčič, G., and Levec, J., *Catalytic liquid-phase nitrite reduction: Kinetics and catalyst deactivation.* AIChE Journal, 1998. 44(10): p. 2280-2292.
30. Franch, C., Lammertink, R.G.H., and Lefferts, L., *Partially hydrophobized catalyst particles for aqueous nitrite hydrogenation.* Applied Catalysis B: Environmental, 2014. 156-157: p. 166-172.
31. Shuai, D., Choe, J.K., Shapley, J.R., and Werth, C.J., *Enhanced Activity and Selectivity of Carbon Nanofiber Supported Pd Catalysts for Nitrite Reduction.* Environmental Science & Technology, 2012. 46(5): p. 2847-2855.
32. Ebbesen, S.D., Mojet, B.L., and Lefferts, L., *Effect of pH on the Nitrite Hydrogenation Mechanism over Pd/Al2O3 and Pt/Al2O3: Details Obtained with ATR-IR Spectroscopy.* The Journal of Physical Chemistry C, 2011. 115(4): p. 1186-1194.
33. Chinthaginjala, J.K. and Lefferts, L., *Support effect on selectivity of nitrite reduction in water.* Applied Catalysis B: Environmental, 2010. 101(1-2): p. 144-149.
34. Wada, K., Hirata, T., Hosokawa, S., Iwamoto, S., and Inoue, M., *Effect of supports on Pd–Cu bimetallic catalysts for nitrate and nitrite reduction in water.* Catalysis Today, 2012. 185(1): p. 81-87.
35. Hörold, S., Vorlop, K.D., Tacke, T., and Sell, M., *Development of catalysts for a selective nitrate and nitrite removal from drinking water.* Catalysis Today, 1993. 17(1–2): p. 21-30.

36. Toebes, M.L., Bitter, J.H., Jos Van Dillen, A., and De Jong, K.P., *Impact of the structure and reactivity of nickel particles on the catalytic growth of carbon nanofibers.* Catalysis Today, 2002. 76(1): p. 33-42.
37. Sadrzadeh, M., Shahidi, K., and Mohammadi, T., *Effect of operating parameters on pure and mixed gas permeation properties of a synthesized composite PDMS/PA membrane.* Journal of Membrane Science, 2009. 342(1–2): p. 327-340.
38. Mikami, I., Sakamoto, Y., Yoshinaga, Y., and Okuhara, T., *Kinetic and adsorption studies on the hydrogenation of nitrate and nitrite in water using Pd-Cu on active carbon support.* Applied Catalysis B: Environmental, 2003. 44(1): p. 79-86.
39. Matatov-Meytal, Y., *Cloth catalysts in water denitrification III. pH inhibition of nitrite hydrogenation over Pd/ACC.* Applied Catalysis B: Environmental, 2003. 45(2): p. 127-134.
40. Zhao, Y., *Colloidal nanoparticles as catalyst and catalyst precursors for nitrite hydrogenation*, in *CPM*. 2015, University of Twente: Enschede. p. 133.

Appendix C: Calculation of nitrite concentration

To calculate the concentration gradient of hydrogen through the PDMS membrane, it was assumed that all the hydrogen that diffuses through the membrane reacts at the catalyst particles. Therefore, the rate of hydrogen diffusion inside the PDMS should be the same as the reaction rate of hydrogen consumption. Equation C1 describes this situation where D is the diffusion coefficient of hydrogen in the PDMS (~10^{-8} m^2/s), ΔC is the concentration gradient inside the PDMS (mol/m^3), Δl is the thickness of the PDMS (10^{-5} m), A is the cylindrical area through which hydrogen diffuses (1,9 * 10^{-3} m diameter, 5,5 * 10^{-2} m length), q is the liquid flow rate (8,3 * 10^{-7} L/s), C_0 is the initial nitrite concentration (4.3 * 10^{-5} mol/L), C_f is the final nitrite concentration (mol/L) and $\%_{NH_4^+}$ is the ammonia selectivity.

To calculate the concentration gradient of nitrite through the alumina grains without CNFs, it was assumed that the rate of nitrite reacted is equivalent to the molecular flux of nitrite through the alumina wall. Equation C2 describes this situation. Here, D is the diffusion coefficient of nitrite in water (1.91 * 10^{-9} m^2/s), ε is the porosity of the alumina (0.34) and τ is the tortuosity (assumed 2).

The percentage of concentration decrease was calculated from equation C3 for both, nitrite and hydrogen, where C_m is the average concentration at the inner alumina wall for nitrite and the concentration at the outer alumina wall for hydrogen. The C_m value for hydrogen will be independent on the conversion since no hydrogen concentration gradients are expected in the axial direction. Contrary, nitrite concentration in the liquid will vary in the axial direction since conversions are well above differential conditions.

$$-D * \frac{\Delta C}{\Delta l} * A = q * (C_0 - C_f) * \%_{NH_4^+} * 3 + q * (C_0 - C_f) * (1 - \%_{NH_4^+}) * 1.5 \qquad \text{Equation C1}$$

$$-\varepsilon * \frac{D}{\tau} * \frac{\Delta C}{\Delta l} * A = q * (C_0 - C_f) * \%_{NH_4^+} * 3 + q * (C_0 - C_f) * (1 - \%_{NH_4^+}) * 1.5 \qquad \text{Equation C2}$$

$$\frac{C_m - \Delta C}{C_m} \qquad \text{Equation C3}$$

Note that these calculations provide just an order of magnitude of the concentration gradients of hydrogen and nitrite in the PDMS and the alumina respectively, and not an exact number since several assumptions were made. In particular, the averaged nitrite concentration was calculated assuming a linear decrease in nitrite concentration through the axial direction of the reactor.

It was calculated that the nitrite concentration entering the CNF region of the thin egg-shell reactor (200 μm), is decreased with about 80% compared to the nitrite concentration in the liquid feed when operating with 2% hydrogen and 44 μmol NO_2^-/L. The gradient in the hydrogen concentration through the PDMS membrane causes an insignificant decrease in concentration in the order of 1%.

Chapter 4

Ni in CNFs: highly active for nitrite hydrogenation

Chapter published as:

Brunet Espinosa, R.; Lefferts, L., Ni in CNFs: highly active for nitrite hydrogenation (submitted to ACS Catalysis journal).

Abstract

Nickel 'hairy' foam, consisting of carbon nano-fibres (CNFs) grown on the surface of nickel foam, is catalytically active in nitrite hydrogenation in absence of any noble metal, which is attributed to the formation of nickel particles with high carbon content during CNF growth. These nickel particles have catalytic properties similar to noble metals, but easily deactivate when exposed to oxygen. This deactivation is attributed to nickel passivation as well as carbon oxidation. Partial reactivation of the nickel particles can be achieved *via* reduction in gas or liquid phase, although the remaining catalytic activity is lower, depending on the remaining concentration of dissolved carbon.

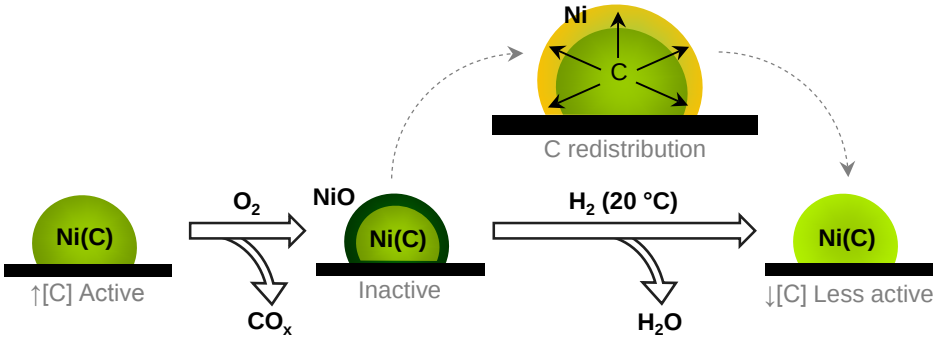

1. Introduction:

Three phase catalytic reactions (G-L-S) are becoming more important in the chemical industry, especially in the petrochemical, bulk and fine chemical processes [1-4]. Usually, in these G-L-S reactions, the efficiency of the chemical reaction is significantly influenced by external (gas-liquid and liquid-solid) and/or internal mass transport [5], and only partly determined by the intrinsic activity and selectivity of the catalyst. Existing technologies to perform these reactions are slurry and trickle/fixed bed reactors [6]. The small catalyst particles in slurry reactors (typically in the order of 50 μm) are usually separated from the product stream by filtration, elevating significantly the operation costs [1]. In addition, attrition of the small catalyst particles usually causes the formation of fines, further complicating the operation of the filtration. In trickle/fixed beds, the catalyst bodies have typical sizes larger than 1 mm to prevent excessive pressure drop. These large catalyst particles can easily induce internal mass transfer limitations, decreasing the overall rate. Additionally, mal-distribution of the feed stream due to random packing of the catalyst particles can create channeling/by-passing of the feed and stagnant zones [1, 7, 8].

Structured reactors are an attractive alternative for these conventional reactor configurations, consisting of an structured internal made of metal, ceramic or carbon [4]. These are characterized by high regularity, low pressure drop, easy catalyst recovery and high accessibility to the catalyst active phase [1, 7]. Monoliths are one of the most widely studied structured reactors due to their extensive use in the automotive industry and for environment applications [4, 8, 9]. However, other structured reactors based on foams [10-14], cloths [15, 16], wires [17], filters [18] and fibres [19] have also been explored.

Recently, solid foams have been attracting attention as structured packings since they can be used as catalyst support, heat exchanger and chemically inert packings [20]. Foams can be made from numerous materials comprising metals, ceramics, carbon and silicon carbide, mimicking the inverse structure of a packed bed made

of dense spheres (figure 1a) [21]. Although foams present similar specific surface areas as monoliths, they exhibit higher voidage (up to 97-98%) [1]. The main disadvantage is that the geometrical surface area of the solid foams is insufficient for direct application as catalyst support. Therefore, the surface of the foam has to be coated with a thin and highly-porous layer to increase the total surface area of the foam [21]. Covering the walls of the foam with an uniform washcoat is not trivial since the attachment of the coating is sometimes poor [21, 22]. However, Tronconi et al. successfully managed to deposit f $Ni/MgAl_2O_4$ washcoats on FeCr alloy foams [23]. An alternative to applying washcoats is growing carbon nano-fibres (CNFs) on metallic foams [11, 12] or on *e.g.* carbon foams loaded with nickel, iron or cobalt nano-particles [10]. CNFs present excellent mechanical stability, are chemically inert and their surface chemistry can be modified, making them very suitable for catalyst support applications. Importantly, CNFs grown on nickel foam are strongly attached to the foam, preventing catalyst loss [11]. Additionally, thin layers of entangled CNFs exhibit open structures with high surface areas (100-200 m^2/g) and large pore volumes (0.5-2 cm^3/g), minimizing the chance that internal mass transfer limitations occur during application as catalyst support [1, 14].

Nitrite hydrogenation is a fast G-L-S reaction that can benefit from minimizing mass transfer limitations, by using Pd or Pt supported on metal foams with a thin layer of grown CNFs (metal 'hairy' foam) [1]. Generally, nitrate is an inorganic contaminant found in water. Nitrate can be easily converted to nitrite inside the human body, creating important health issues like methemoglobinemia (blue baby syndrome) or can form nitrosamines which are known to be carcinogenic [1, 24, 25]. Catalytic hydrogenation using noble metals is a technique that has been developed in 1989 to convert nitrate to, preferably, nitrogen or to ammonia as an unwanted by-product. Nitrate is converted by first converting it to nitrite as the first intermediate product, which is rapidly further converted to the final products, nitrogen and ammonia. Many efforts have been directed to prevent the formation of ammonia [24, 26, 27], whereas previous work in our group reported on the same starting form nitrite [11, 28]. However, all these studies have in common that noble

metal based catalysts are needed, the only exception being catalysts containing metallic Fe, that actually act as a stoichiometric reducing agent [29-32].

In this work we perform catalytic hydrogenation of nitrite with nickel 'hairy' foam without the use of noble metal. We demonstrate that carbon dissolution in the nickel induces catalytic activity, providing a cost-effective alternative for conventional hydrogenation of nitrite with Pd or Pt.

2. Experimental

2.1. Materials used

Polycrystalline nickel foam (99% purity, Recemat) was used as catalyst for the growth of carbon nano-fibres (CNFs). The foam consists of a three dimensional network of connected strands (figure 1 a). Nickel foam cylinders of 4.3 mm in diameter were cut from sheets with a size of 100x100 mm^2 and 5 mm thickness using wire-cut Electrical Discharge Machining (AGIECUT CHALLENGE 2). The surface area per gram sample was estimated by Jarrah et al. [12] to be less than 1 m^2/g. γ-Alumina (γ-Al_2O_3) spheres (Engelhard) with a total surface area of 250 m^2/g were used as catalyst support for nickel. Ethylene (99.95% PRAXAIR), hydrogen and nitrogen (99.999% INDUGAS) were used for the growth of the CNFs on the nickel foam. Nickel nitrate hexahydrate (Merck), urea (Merck) and nitric acid (65%, Merck) were used for nickel deposition on γ-Al_2O_3. Palladium acetylacetonate (Alfa Aesar) and toluene (>99.9%, Merck) were used for depositing Pd on the nickel foam. Sodium nitrite (>99%, Merck) was used as nitrite source for the catalytic experiments.

2.2. Sample preparation

2.2.1. Nickel 'Hairy' foam

2.2.1.1. CNF growth

Nickel foam cylinders were used as received after being cut. A similar procedure as described in [33] was used to grow CNFs. In this work, 46 cylinders (1.7 g) were placed simultaneously in an in-house-build quartz reactor of 50 mm inner diameter with a porous quartz plate to hold the nickel foam cylinders. The foam cylinders were first pre-treated at 700 °C for 1 h in static air followed by a reduction step of 2 h under a mixture of 20%H_2 in N_2 at 700 °C with a total flow rate of 100 ml/min. Next, the temperature was lowered to 440 °C under 80 ml/min of N_2. The CNF growth was performed at 440 °C for 0.7 h with a mixture of 25% C_2H_4 in N_2 (100 ml/min of total flow rate). The nickel foam cylinders with CNFs (nickel 'hairy' foam) were then cooled down to room temperature under N_2 atmosphere.

Any loose CNFs were removed by applying a pressurized N_2 flow. Almost no change in weight was observed (<1%), consistent with previous work [12, 34].

2.2.1.2. Palladium deposition

Palladium was deposited on some of the nickel 'hairy' foam *via* wet impregnation technique. To achieve a loading about 2 wt%, 4.0 mg of palladium acetylacetonate was dissolved in 40 ml of toluene and nickel 'hairy' foam cylinders (0.2 g) were placed inside the solution. The solution was then poured in a round bottom flask connected to a vacuum rotary evaporator. The temperature of the solution was kept at 50 °C using an oil bath. Progressively, vacuum was applied leading to toluene evaporation. Palladium acetylacetonate was left behind, deposited on the nickel 'hairy' foam. Finally, the samples were dried at 85 °C for 2 h in vacuum.

2.2.1.3. Oxidation-reduction

All nickel 'hairy' foam cylinders (with and without palladium) were placed inside an oven and calcined in air at 250 °C for 2 h with a flow rate of 50 ml/min. Next, the samples were reduced for 2 h at the same temperature in a mixture of 50%H_2 in N_2 with a total flow rate of 50 ml/min. Finally, the samples were cooled down in N_2 atmosphere.

2.2.1.4. Oxidation

Some of the nickel 'hairy' foam cylinders without palladium were oxidized in static air at different temperatures (50, 100, 150 and 200 °C) before catalytic testing. The samples were placed in a furnace and the temperature was raised by 10 °C/min under static air until the final oxidizing temperature was reached. After 2 h the samples were cooled down to room temperature, also in static air.

2.2.2. Detached CNFs

Some of the prepared nickel 'hairy' foam cylinders were immersed in a flask containing miliQ water and were magnetically stirred at 500 rpm for 72 h to partially remove the grown CNFs. After stopping the stirring, the temperature was raised to 90 °C for 10 h to evaporate all the water. Next, the detached CNFs were collected from the bottom of the flask and separated from the nickel 'hairy' foam cylinders that lost more than twice (58.2%) of their CNF content during the stirring process. Then, the detached CNFs and the nickel 'hairy' foam partially covered with CNFs were reduced separately at room temperature under a mixture of 50% H_2 and 50% N_2 with a total flow-rate of 100 ml/min.

Some of the detached CNFs were compressed as a pellet under 3 bar pressure at room temperature and were oxidized successively at different temperatures (50, 100, 150, 200, 250, 300, 350, 400, 450 and 500 °C) under static air for 2 h. The heating rate used was 5 °C/min.

2.2.3. γ-Al_2O_3

Homogeneous deposition-precipitation technique was used to deposit nickel on γ-Al_2O_3. First, 1.7 g γ-Al_2O_3 was immersed in a stirred three-neck round bottom flask containing 80 ml nickel nitrate solution with a concentration of 1.3 g Ni/L. The temperature of the solution was kept constant at 100 °C with an oil bath. A reflux system was connected to the three-neck round bottom flask to condensate the evaporated water. The pH of the solution was initially adjusted to 3.5 using a diluted nitric acid solution (0.65 vol%). To precipitate the nickel on the alumina, 20 ml of urea solution (53.0 g/L) was added drop-wise to the solution containing the alumina during the initial 15 minutes. After 2 h, the alumina was removed from the nickel solution, washed with miliQ water and dried at 85 °C in vacuum during 2 h.

Subsequently, an oxidation and reduction step was performed according to the procedure described for the nickel 'hairy' foam.

2.3. Characterization techniques

The BET surface area of the prepared materials was determined from N_2-adsorption isotherm obtained at 77K (Micromeritics Tristar). The amount of CNFs on the sample was determined with an analytical balance by weighing the sample before and after CNF growth. The morphology of the nickel 'hairy' foam was analysed with two different Scanning Electron Microscopes, HR-SEM (Analysis Zeiss MERLIN HR-SEM and Jeol JSM-6010LA). CNF diameter was calculated by averaging the size of 300 fibres at five different locations in the sample. Transmission Electron Microscopy, HR-TEM (Philips CM300ST-FEG) was used to study the morphology of the nickel particles located inside the CNFs. X-Ray diffraction technique, XRD (Bruker D2 Phaser diffractometer) with a Cu Kα radiation (λ= 0.1544 nm) was used to identify the phases present in the samples.

2.4. Catalytic tests

The catalytic activity for nitrite hydrogenation was measured at 20 °C in a fixed bed reactor made of PEEK (polyether-ether-ketone). The internal diameter of the reactor was 4.7 mm, which fits exactly with the diameter of the nickel 'hairy' foam cylinders. The length of the reactor was 25 mm which could contain four pieces of nickel 'hairy' foam. The same reactor was used to test detached CNFs, nickel 'hairy' foam with partial CNF removal and nickel on γ-Al_2O_3. The liquid feed had always a nitrite concentration between 425 and 445 μmol/L and was saturated at 1 bar with H_2 (780 μmol/L). Nitrite solutions were pumped through the fixed bed reactor with a flow rate of 3 ml/min with a HPLC pump (DIONEX, Ultimate 3000). This generated a pressure drop lower than 0.4 bar for all experiments. Nitrite (NO_2^-) and ammonium (NH_4^+) concentrations were measured with an Ion Chromatograph (Dionex, ICS 1000) in both the feed and outlet of the reactor. NO_2^- conversion and NH_4^+ selectivity were calculated according to equation 1 and 2, respectively. Since ammonia is the only by-product of the reaction, nitrogen was calculated based on the mass balance [11, 28].

$$NO_2^- \text{ conversion} = \frac{[NO_2^-]_{initial} - [NO_2^-]_{final}}{[NO_2^-]_{initial}} \cdot 100 \qquad \text{Equation 1}$$

$$NH_4^+ \ selectivity = \frac{[NH_4^+]_{final} - [NH_4^+]_{initial}}{[NO_2^-]_{initial} - [NO_2^-]_{final}} \cdot 100 \qquad \text{Equation 2}$$

3. Results

3.1. Characterization

Figure 1a and b shows the morphology of nickel foam, consisting of hollow strands shaped as prisms. Every strand has a wall thickness around 10-15 μm. The calculated porosity of the material based on volume, weight and density of nickel is 94 vol% which agrees with the specifications of the manufacturer (95 vol%). Figure 1c and d shows complete coverage of the nickel strands with a

homogeneous CNF layer around 20 μm thick at the outer surface of the strands. The hollow part of the strand also accommodates CNFs, completely filling the inner space with compressed CNFs (figure 1c). After CNF growth, the thickness of the nickel strands is decreased to 5-8 μm (figure 1d) due to nickel consumption during CNF growth. Between the nickel (bright in figure 1d) and the CNF layer, a thin layer of amorphous carbon was observed (Appendix A, and also reported elsewhere [33]).

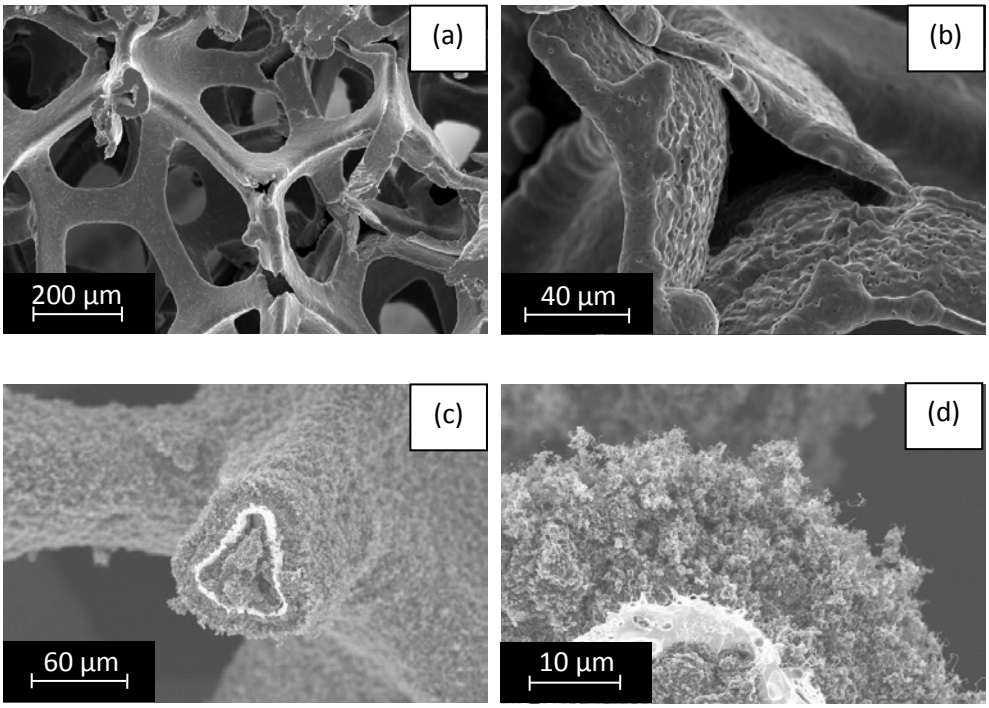

Figure 1: Cross-sectional views with HRSEM of nickel foam before CNF growth (a and b) and after CNF growth (c and d).

The total carbon loading is 27 wt%, creating a BET surface area of 22 m^2/g and a BET surface area per gram carbon of 81 m^2/g_{Carbon}, similar to the results reported by Kumar et al. [11]. The average CNF diameter is 95 nm based on HRSEM, containing nickel particles of the same size incorporated inside the CNF structure,

see figure 2a. The location and shape of the nickel particles suggests a fishbone solid type of CNF structure [35-37].

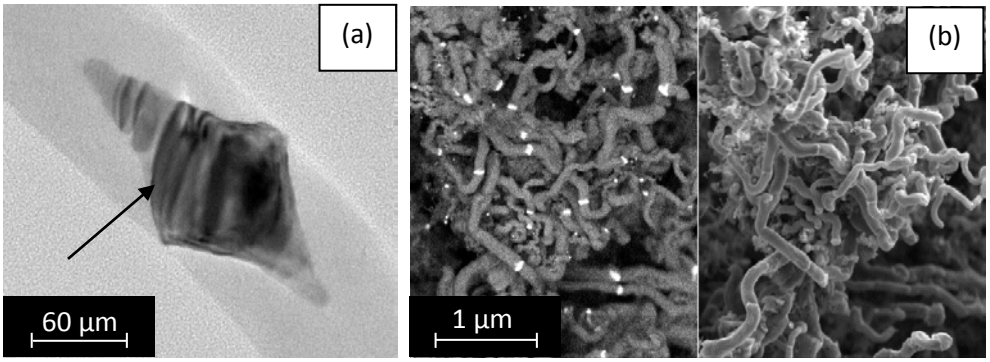

Figure 2: a) HRTEM image of a nickel particle contained inside the CNF structure of nickel 'hairy' foam with an arrow indicating the border between the exposed and buried nickel, b) HRSEM measurement with ESB (left) and in-lens (right) detectors of a cross sectional view of a nickel 'hairy' foam cylinder. Bright discs indicate the presence of nickel particles inside the CNF structure.

Figure 2b shows that most of the CNFs contain a nickel particle (bright disk) inside their structure. The thin disc suggests that a fraction of the nickel is not covered by carbon. Figure 2a suggests that the outer sharp parts of the nickel particle are buried in the CNF whereas the middle part seems to stick out, especially when looking at the sharp border between the upper part and the middle part of the particle, as indicated by the arrow. Unfortunately, the nickel content in the CNFs could not be determined due to the presence of much larger amount of nickel in the foam structure, which could not be separated.

3.2. Catalytic tests

Nickel 'hairy' foam without palladium is active in nitrite hydrogenation. As shown in figure 3, at steady state (50 min of time-on-stream), nickel 'hairy' foam presents 16% nitrite conversion. This surprising observation demonstrates that nickel 'hairy'

without any noble metal can hydrogenate nitrite. Figure 3 shows that the conversion observed with nickel 'hairy' foam without palladium is one third of the conversion at steady state of the nickel 'hairy' foam loaded with ~2 wt% palladium (47%). Therefore, the actual contribution of palladium is only two third of the total conversion. For both samples, ammonia selectivity is around 70% suggesting that palladium and 'hairy' foam exhibit similar selectivity. The activity of nickel 'hairy' foam remained constant and without any sign of deactivation during two weeks of operation.

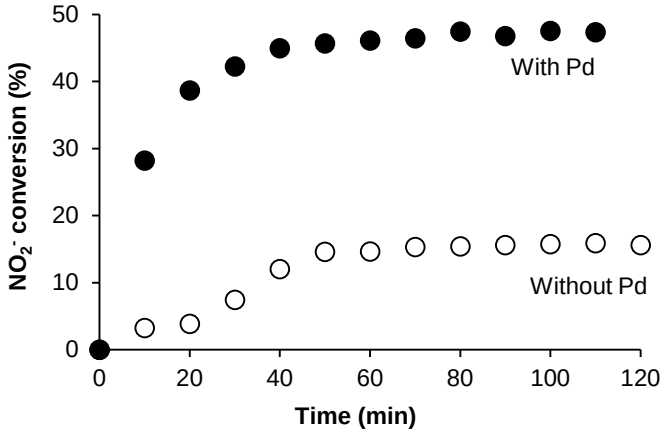

Figure 3: Nitrite conversion over nickel 'hairy' foam with 2 wt% Pd and without palladium. Experiments were performed with 0.18 g of nickel 'hairy' foam with a solution of 435 μmol NO_2^-/L and 780 μmol H_2/L, and a flow rate of 3 ml/min.

Nickel 'hairy' foam was also tested in absence of dissolved hydrogen. No activity was observed, confirming that nitrite hydrogenation is catalysed by nickel 'hairy' foam and that the activity is not due to any stoichiometric reaction between nickel and nitrite. Nickel foam reduced at 700 °C without CNFs and nickel supported on γ-Al_2O_3 with a loading of 6.5 wt% and a surface area of 0.4 m^2/g showed no activity, indicating that nickel is not an active catalyst for this reaction. Similar results were observed for nickel foam covered with a layer of amorphous carbon,

proving that the amorphous carbon layer between the CNFs and the surface of the nickel foam is also not a catalytic active phase for nitrite hydrogenation.

Figure 4 compares catalytic activity of nickel 'hairy' foam, nickel 'hairy' foam with partial CNF removal (58.2 % removed) and all detached CNFs (0.024 g) from the same sample. Clearly, the nickel 'hairy' foam is the most active, but both detached CNFs and the remaining CNFs on the 'hairy' foam exhibit similar and significant activity.

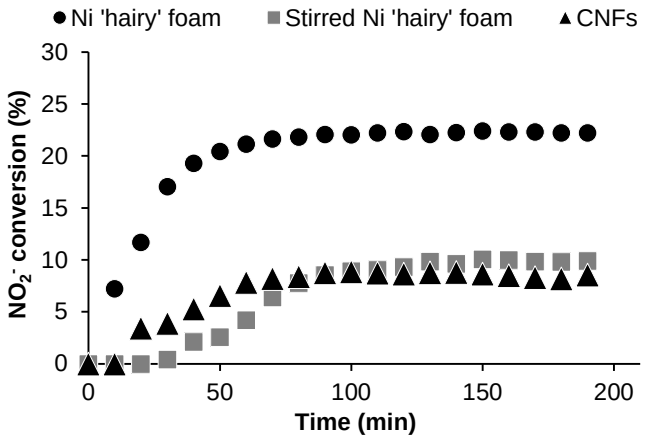

Figure 4: Nitrite conversion over nickel 'hairy' foam (0.20 g), the stirred 'hairy' foam (0.17 g) and the CNFs (0.024 g). Experiments were performed with a solution of 435 μmol NO_2^-/L and 780 μmol H_2/L, and a flow rate of 3 ml/min.

Nickel 'hairy' foam cylinders oxidized at different temperatures (from ambient to 200 °C) were tested in the nitrite hydrogenation reaction. Figure 5 shows that the steady state conversion decreases when the oxidation temperature of the nickel 'hairy' foam is increased. Moreover, the activation time of the sample becomes longer when the sample is oxidized at high temperatures. Oxidation at 200 °C seems to deactivate the material completely, although an activation effect that would take longer than 8 h cannot be excluded.

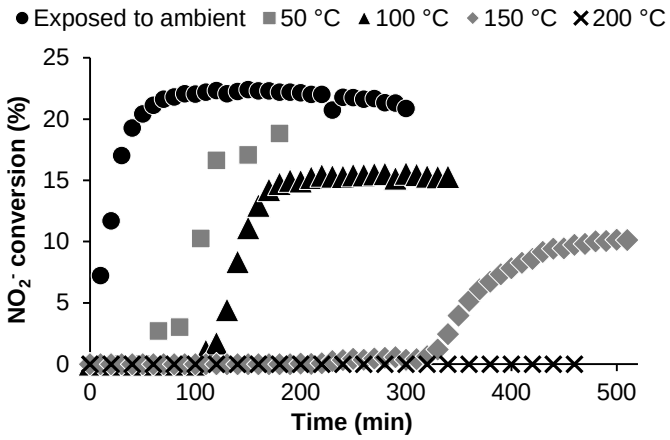

Figure 5: Nitrite conversion over different nickel 'hairy' foam oxidized at different temperatures. Experiments were performed with 0.18 g of nickel 'hairy' foam with a solution of 435 μmol NO_2^-/L and 780 μmol H_2/L, and a flow rate of 3 ml/min.

The sample oxidized at 100 °C after the catalytic experiment reported in figure 5, was dried at room temperature under vacuum and re-oxidized for 2 h at 100 °C. Next, catalytic activity was again measured, followed by an identical third cycle of drying-oxidation-catalyst test. Figure 6 shows a decreasing steady state activity and an increasing activation time with the number of cycles. The difference between the first two runs is minor while the third run shows a more pronounced increase in activation time and a significant loss of steady state activity. The deactivation of the sample cannot be attributed to a thermal effect since a pre-treatment in nitrogen at the same temperature (100 °C) does not induce any deactivation.

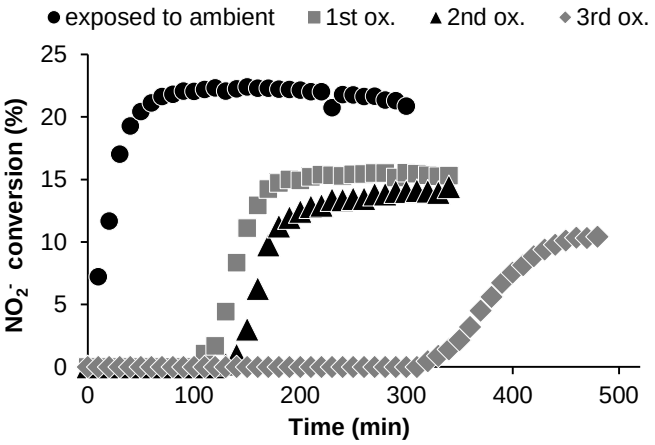

Figure 6: Nitrite conversion over nickel 'hairy' foam, after exposure to ambient and after repetitive oxidation at 100 °C in three consecutive cycles. Experiments were performed at room temperature with 0.18 g of nickel 'hairy' foam with a solution of 435 μmol NO_2^-/L and 780 μmol H_2/L, and a flow rate of 3 ml/min.

Fresh nickel 'hairy' foam cylinders, oxidized at 50 °C, were pre-treated for 2 h with a continuous flow of 3 ml/min of either miliQ water saturated with 1 bar hydrogen, or with a nitrite solution saturated with argon at 1 bar. Figure 7 shows that during subsequent catalytic testing, nickel 'hairy' foam pre-treated in hydrogen exhibits immediate activity. In contrast, the sample pre-treated in the nitrite solution shows identical catalytic behaviour as nickel 'hairy' foam oxidized at 50 °C, without any further pre-treatment. This indicates that dissolved hydrogen is able to activate the sample, in contrast to nitrite. The initial activity of 'hairy' foam pre-treated in hydrogen is even higher than the steady state activity, probably due to high hydrogen coverage of the active sites at the beginning of the reaction. Pre-treatment of the oxidized 'hairy' foam with hydrogen in gas phase at 20 °C also induces catalyst activation, although a short activation time is still observed, because exposure to ambient after the reduction treatment causes mild re-oxidation.

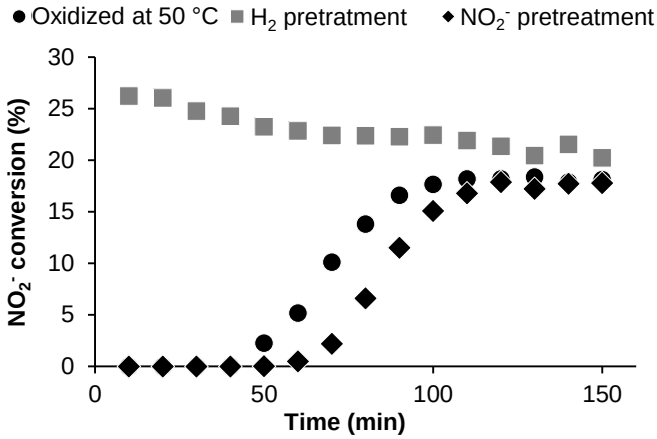

Figure 7: Effect of the pre-treatment on the nitrite conversion over nickel 'hairy' foam oxidized at 50 °C. Experiments were performed with 0.18 g of nickel 'hairy' foam with a solution of 435 μmol NO_2^-/L and 780 μmol H_2/L, and a flow rate of 3 ml/min.

3.3. XRD measurements

Figure 8 shows the XRD pattern of nickel foam, nickel 'hairy' foam and detached CNFs. Only four diffraction peaks are visible. The peak present at 25.8° is assigned to graphitic carbon [38, 39]. This peak is clearly present in the detached CNFs but also in nickel 'hairy' foam, although with a very low intensity (figure 8b). The other three peaks correspond to different nickel planes. Nickel foam presents peaks at 44.7°, 52.1°, 76.7° which are assigned to the (111), (002) and (022) nickel planes respectively [40, 41]. Nickel 'hairy' foam and detached CNFs present the same diffraction peaks, but the peaks appear significantly shifted, as can be clearly seen in Figure 8c for the (111) reflection. The diffraction peak shifts to lower 2θ values in the order: CNF < nickel 'hairy' foam < nickel foam. The other two nickel diffraction peaks exhibit similar changes.

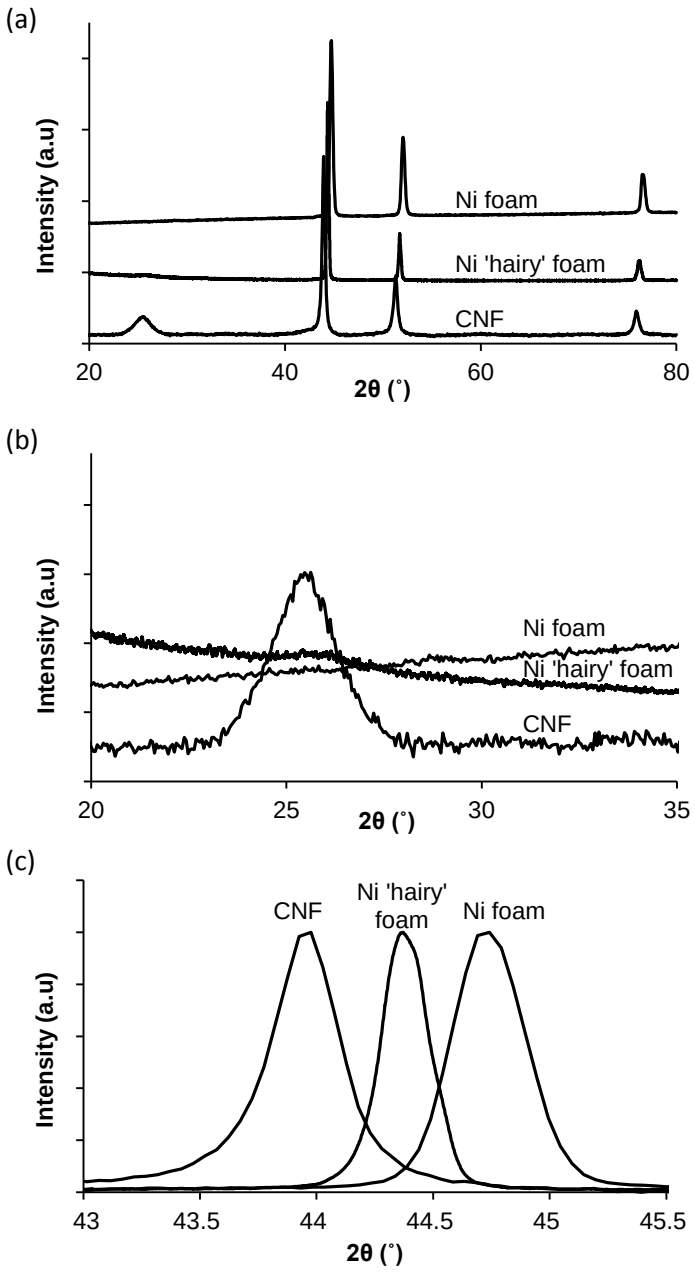

Figure 8: XRD patterns of the nickel foam, nickel 'hairy' foam and detached CNFs a) full pattern range, b) graphite peak, c) (111) nickel plane. Each spectrum was normalized by the intensity of the highest peak.

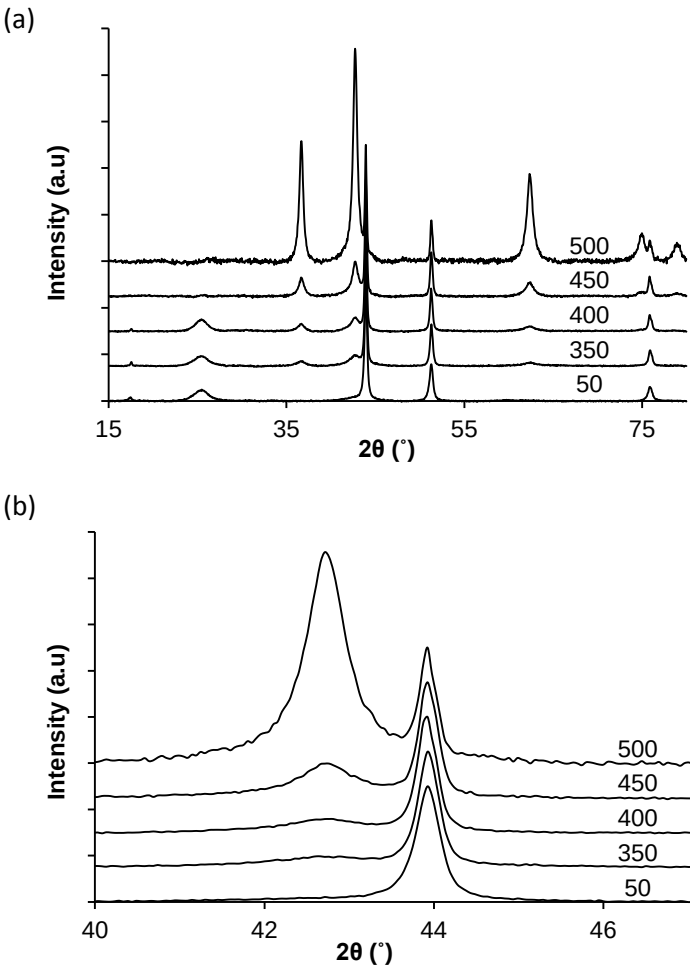

Figure 9: XRD spectra of the detached CNFs after different oxidation temperatures, a) full diffractogram, b) zoom in on main nickel oxide and nickel peaks (42.7° and 43.9° respectively). Spectra were normalized by the intensity of the peak at 43.9°.

Figure 9 shows the XRD patterns of the detached CNFs, oxidized at different temperatures. All the patterns were normalized by the intensity of the nickel peak at 43.9 °C. Between 50 and 300 °C, no significant differences were observed. However, above 350 °C, new peaks appeared (36.6, 42.8, 62.4, 75.0 and 79.0), indicating the formation of nickel oxide [42, 43]. In fact, at high oxidation

temperatures, the ratio nickel oxide/nickel increases as expected. The peak at 43.9° in figure 9b demonstrates that during oxidation at high temperature, nickel peaks do not shift.

Figure 10 shows a shift of the main nickel peak towards higher 2θ values when nickel 'hairy' foam cylinders undergo oxidation-reduction cycles, which consist of oxidation in air followed by reduction during catalytic testing at room temperature. Both, the sample oxidized three consecutive times in air at 100 °C (followed by catalytic testings, figure 6) and the sample oxidized in air at 150 °C (followed by catalytic testing, figure 5) show a peak position between the nickel 'hairy' foam and the nickel foam peak position. The other two nickel peaks at 52.1° and 76.7° present similar shifts.

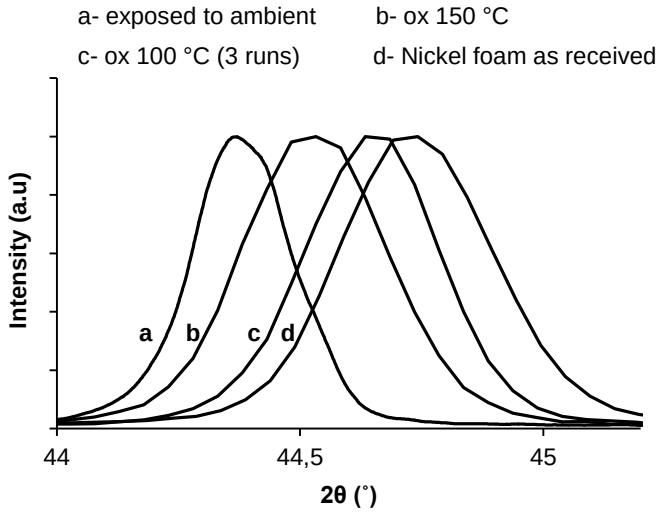

Figure 10: XRD spectra of the (111) nickel peak for the nickel foam and for nickel 'hairy' foam cylinders oxidized at different temperatures (100 and 150 °C) followed by catalytic testing. Notice that the sample oxidized at 100 °C underwent three oxidation-testing cycles.

4. Discussion

Nickel 'hairy' foam without noble metal exhibits catalytic activity for nitrite hydrogenation (figure 3). Similarly, detached CNFs and nickel 'hairy' foam with partial CNF removal also show some activity, although significantly lower (figure 4). However, normalizing the conversions reported in figure 4 by the amount of CNFs, all three samples show a very similar activity (figure 11), indicating that the CNFs are responsible for the surprising activity of the nickel 'hairy' foam. Since carbon is not active for nitrite hydrogenation [44], nickel particles present in the CNFs must somehow induce this catalytic activity.

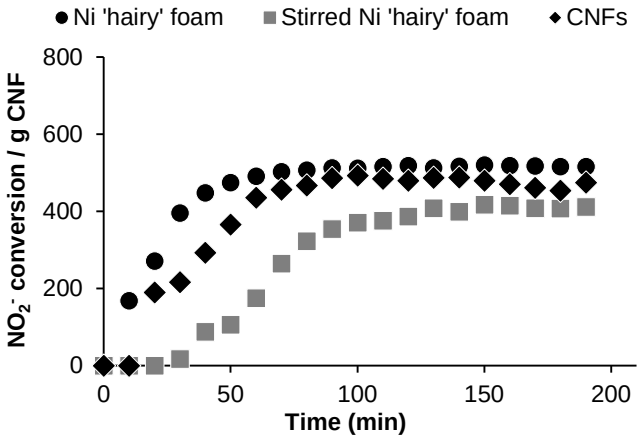

Figure 11: Nitrite conversion per gram CNF of the nickel 'hairy' foam (0.043 g CNF), the stirred 'hairy' foam (0.024 g CNF) and the CNFs (0.018 g CNF). Experiments were performed with a solution of 435 μmol NO_2^-/L and 780 μmol H_2/L, and a flow rate of 3 ml/min.

However, it is known that nickel exhibits very poor activity in nitrite hydrogenation at room temperature [24] since base metals require higher temperatures and/or pressures than noble metals in hydrogenation reactions [45]. Experiments performed with nickel on γ-Al_2O_3 (0.4 m^2 Ni/g) and with bare nickel foam confirmed no measurable nitrite conversion after any time-on-stream. The experiment performed with nickel on γ-Al_2O_3 contained 0.4 m^2 Ni. This value is in

the same order of magnitude as the maximum nickel surface area corresponding to the nickel particles present in a catalytic experiment with nickel 'hairy' foam, *i.e.* 0.6 m^2 Ni. This surface area was estimated based on the decrease in thickness of the nickel foam wall (figure 1d) and the nickel particle size (95 nm), assuming that all the nickel that disappears from the wall of the strands ends up as nickel nano-particles on the CNFs. The value obtained is therefore a gross overestimation because a significant part of the surface of the nickel particles is covered by graphitic carbon of the CNFs. In any case, the relatively high activity of the nickel 'hairy' foam can clearly not be explained by the activity of metallic nickel.

XRD reveals that the nickel particles present in the CNFs contain dissolved carbon (figure 8a and c) since all nickel peaks of the detached CNFs present a shift to lower 2θ values as compared to the peaks of the nickel foam. This effect has been attributed to lattice expansion due to dissolved carbon [40]. Nickel peaks from nickel 'hairy' foam also present a negative shift as compared to nickel foam. However, the change is less pronounced than for the detached CNFs (figure 8a and c). This suggests that nickel particles in the CNFs contain more dissolved carbon than the nickel in the nickel 'hairy' foam.

Even though the nickel particles are embodied in the CNF structure as can be seen in figure 2, the HRTEM image (figure 2a) seems to indicate than the centre part of the nickel particle is not covered by carbon, as usually reported for CNFs with a fishbone solid type structure [36]. In addition, the bright white narrow discs observed in the CNFs (figure 2b) also suggest that a fraction of the nickel is not buried inside the CNFs, but might be exposed and accessible for the reactants. Obviously, there is no direct proof from microscopy that part of the nickel surface is completely free of carbon; however, the activity observed in nitrite hydrogenation clearly indicates that a fraction of the nickel particles is indeed not covered by carbon, as otherwise no catalytic activity would be observed.

The activity of nickel 'hairy' foam decreases and the activation time becomes longer after oxidation treatments (figures 5 and 6). This effect is more pronounced

at high oxidation temperatures. The same effect is observed when nickel 'hairy' foam is oxidized multiple times at a constant temperature: activity decreases and the activation time increases with the number of oxidation treatments (figure 6). This indicates that during the oxidation pre-treatments, the surface of the nickel particles is oxidized, forming a nickel oxide passivation layer. This nickel oxide layer is apparently catalytically inactive, since all oxidized nickel 'hairy' foam need significant activation time before showing any catalytic activity. This activation time is longer after oxidation at higher temperatures, indicating that thicker nickel oxide layers need more time to get reduced. However, these layers remain thin for oxidation temperatures between 20 and 200 °C, since NiO cannot be detected with XRD, in contrast to oxidation temperatures above 350 °C (figure 9).

According to literature [46], nickel passivation with low oxygen partial pressure at room temperature creates typically 2 to 4 monolayers of nickel oxide, which indeed would not be detectable with XRD. Since all samples are initially passivated at room temperature, it could be that they are somehow protected against subsequent oxidation at higher temperatures and therefore, the thickness of the nickel oxide does not increase dramatically. This could explain why even after oxidation at 200 °C, no nickel oxide peak can be detected with XRD.

Even though a nickel oxide layer passivates the nickel particles, after some time, catalytic activity is recovered, induced by reduction of the nickel oxide layer by the hydrogen dissolved in the nitrite solution. This follows from the observation that *in-situ* reduction in hydrogen saturated water, results in complete reactivation of nickel 'hairy' foam oxidized at 50 °C (figure 7). If the sample is reduced at room temperature with hydrogen *ex-situ*, it is also activated but due to exposure to ambient before catalytic testing, still 1 h time-on-stream is needed to reach steady state activity. Nickel 'hairy' foam oxidized at 200 °C resulted in no activity during 460 min time-on-stream. Although we cannot rule out that activation would take place after longer time-on-stream, it is quite clear that high oxidation temperatures have a detrimental effect on the catalytic activity.

Surprisingly, a pre-treatment in hydrogen at room temperature in both liquid and gas phase can reactivate the sample by reducing the passivation layer. In literature, higher temperatures (250-500 °C) are reported for the reactivation of passivated nickel [47-49]. We propose that the dissolution of carbon modifies the electronic structure of nickel, similar to the effect of carbon on other metals from the group VI like molybdenum and tungsten carbide [50-53]. It is reported that reactant molecules bind too strongly to these metals thus, not satisfying the Sabatier's principle. However, by introducing interstitial carbon, the reactivity of these metals is increased due to the increasing electron density, inducing similarity to noble metals [51]. Analogously, carbon dissolution could also induce nickel to mimic precious metals, facilitating both hydrogen activation and reduction of the surface oxide at room temperature, which has not been reported before, to the best of our knowledge. This results in catalytic activity for nitrite hydrogenation at room temperature.

However, the activity of the nickel particles after activation decreases irreversibly with the intensity of the oxidation treatment (figures 5 and 6). This is attributed to a decrease in carbon content in the nickel particles *via* carbon oxidation, which is supported by the shift in the XRD peak observed in figure 10. Unfortunately, TPO experiment of nickel 'hairy' foam cylinders could not be used to quantify the amount of carbon oxidized to CO or CO_2 due to insufficient sensitivity of the equipment. Remarkably, removal of carbon cannot be completely achieved by high temperature oxidation only, as can be seen in figure 9: the (111) nickel peak shows no significant shift during oxidation at temperatures as high as 500 °C. Apparently, passivation of these particles is highly efficient and carbon can be removed only *via* formation of nickel oxide. Reduction of the passivating layer is needed to allow the carbon to redistribute, leading to a lower overall carbon concentration and additional carbon removal during a next exposure to oxygen.

Previous catalytic results using nickel 'hairy' foam cylinders loaded with palladium [11] for nitrite hydrogenation showed very high turnover frequencies (TOFs) that could not be entirely explained. Possibly, the high TOFs are partly

caused by the additional catalytic activity of the nickel particles present in the CNF structure, which had not been considered at that time.

5. Conclusions

'Hairy' foam, consisting of well attached CNFs containing nickel nano-particles and supported on nickel foam, is surprisingly active for nitrite hydrogenation. This is very surprising as normally precious metal particles are required to generate activity at the conditions in this study, *i.e.* room temperature. Nickel particles are located in the graphitic structure of the CNFs and act as catalyst for this hydrogenation reaction. The catalytic activity is assigned to the presence of dissolved carbon in the nickel particles, which is highly sensitive to oxidation, causing removal of dissolved carbon and irreversible deactivation of the catalyst.

6. References

1. Chinthaginjala, J. K. Hairy foam: Thin layers of carbon nanofibers as catalyst support for liquid phase reactions. University of Twente, Enschede, 2010.
2. Duduković, M. P.; Larachi, F.; Mills, P. L., Multiphase catalytic reactors: a perspective on current knowledge and future trends. *Catalysis Reviews* **2002,** *44* (1), 123-246.
3. Aran, H. C.; Klooster, H.; Jani, J. M.; Wessling, M.; Lefferts, L.; Lammertink, R. G. H., Influence of geometrical and operational parameters on the performance of porous catalytic membrane reactors. *Chemical Engineering Journal* **2012,** *207–208*, 814-821.
4. Pangarkar, K.; Schildhauer, T. J.; van Ommen, J. R.; Nijenhuis, J.; Kapteijn, F.; Moulijn, J. A., Structured Packings for Multiphase Catalytic Reactors. *Industrial & Engineering Chemistry Research* **2008,** *47* (10), 3720-3751.
5. Bruehwiler, A.; Semagina, N.; Grasemann, M.; Renken, A.; Kiwi-Minsker, L.; Saaler, A.; Lehmann, H.; Bonrath, W.; Roessler, F., Three-Phase Catalytic Hydrogenation of a Functionalized Alkyne: Mass Transfer and Kinetic Studies with in Situ Hydrogen Monitoring. *Industrial & Engineering Chemistry Research* **2008,** *47* (18), 6862-6869.
6. Aran, H. C. Porous ceramic and metallic microreactors. University of Twente, Enschede, 2011.
7. Gascon, J.; van Ommen, J. R.; Moulijn, J. A.; Kapteijn, F., Structuring catalyst and reactor – an inviting avenue to process intensification. *Catal. Sci. Technol.* **2015,** *5* (2), 807-817.
8. A. Cybulski, J. A. M., *Structured catalysts and reactors*. Second ed.; New York, 2006; p 856.
9. Geus, J. W.; van Giezen, J. C., Monoliths in catalytic oxidation. *Catalysis Today* **1999,** *47* (1–4), 169-180.
10. Wenmakers, P. W. A. M.; van der Schaaf, J.; Kuster, B. F. M.; Schouten, J. C., "Hairy Foam": carbon nanofibers grown on solid carbon foam. A fully accessible, high surface area, graphitic catalyst support. *Journal of Materials Chemistry* **2008,** *18* (21), 2426-2436.
11. Chinthaginjala, J. K.; Lefferts, L., Support effect on selectivity of nitrite reduction in water. *Applied Catalysis B: Environmental* **2010,** *101* (1-2), 144-149.

12. Jarrah, N.; van Ommen, J.; Lefferts, L., Mechanistic aspects of the formation of carbon-nanofibers on the surface of Ni foam: A new microstructured catalyst support. *Journal of Catalysis* **2006,** *239* (2), 460-469.
13. Cordier, A.; Flahaut, E.; Viazzi, C.; Laurent, C.; Peigney, A., In situ CCVD synthesis of carbon nanotubes within a commercial ceramic foam. *Journal of Materials Chemistry* **2005,** *15* (37), 4041.
14. Ledoux, M.-J.; Pham-Huu, C., Carbon nanostructures with macroscopic shaping for catalytic applications. *Catalysis Today* **2005,** *102-103*, 2-14.
15. Cantoro, M.; Golovko, V. B.; Hofmann, S.; Williams, D. R.; Ducati, C.; Geng, J.; Boskovic, B. O.; Kleinsorge, B.; Jefferson, D. A.; Ferrari, A. C.; Johnson, B. F. G.; Robertson, J., Wet catalyst assisted growth of carbon nanofibers on complex three-dimensional substrates. *Diamond and Related Materials* **2005,** *14* (3–7), 733-738.
16. Matatov-Meytal, U.; Sheintuch, M., Activated carbon cloth-supported Pd–Cu catalyst: Application for continuous water denitrification. *Catalysis Today* **2005,** *102–103*, 121-127.
17. Niranjan, K.; Pangarkar, V. G., An International Journal of Research and DevelopmentHydrodynamic and mass transfer characteristics of polypropylene multifilament wire gauze packings. *The Chemical Engineering Journal* **1983,** *27* (1), 49-57.
18. Tribolet, P.; Kiwi-Minsker, L., Carbon nanofibers grown on metallic filters as novel catalytic materials. *Catalysis Today* **2005,** *102–103*, 15-22.
19. Tzeng, S.-S.; Hung, K.-H.; Ko, T.-H., Growth of carbon nanofibers on activated carbon fiber fabrics. *Carbon* **2006,** *44* (5), 859-865.
20. Zhang, W.; Zhang, B.; Shi, Z., Study on hydrodynamic performance and mass transfer efficiency of nickel foam packing. *Procedia Engineering* **2011,** *18*, 271-276.
21. Jarrah, N. Microstructured catalyst support based on carbon nano-fibers (CNFs). University of Twente, Enschede, 2004.
22. Matatov-Meytal, Y.; Sheintuch, M., Catalytic fibers and cloths. *Applied Catalysis A: General* **2002,** *231* (1–2), 1-16.
23. Cristiani, C.; Finocchio, E.; Latorrata, S.; Visconti, C. G.; Bianchi, E.; Tronconi, E.; Groppi, G.; Pollesel, P., Activation of metallic open-cell foams via washcoat deposition

of Ni/MgAl2O4 catalysts for steam reforming reaction. *Catalysis Today* **2012,** *197* (1), 256-264.

24. Hörold, S.; Tacke, T.; Vorlop, K.-D., Catalytical removal of nitrate and nitrite from drinking water: 1. Screening for hydrogenation catalysts and influence of reaction conditions on activity and selectivity. *Environmental Technology* **1993,** *14* (10), 931-939.
25. Pintar, A.; Berčič, G.; Levec, J., Catalytic liquid-phase nitrite reduction: Kinetics and catalyst deactivation. *AIChE Journal* **1998,** *44* (10), 2280-2292.
26. Barrabés, N.; Sá, J., Catalytic nitrate removal from water, past, present and future perspectives. *Applied Catalysis B: Environmental* **2011,** *104* (1-2), 1-5.
27. D'Arino, M.; Pinna, F.; Strukul, G., Nitrate and nitrite hydrogenation with Pd and Pt/SnO2 catalysts: the effect of the support porosity and the role of carbon dioxide in the control of selectivity. *Applied Catalysis B: Environmental* **2004,** *53* (3), 161-168.
28. Franch, C.; Lammertink, R. G. H.; Lefferts, L., Partially hydrophobized catalyst particles for aqueous nitrite hydrogenation. *Applied Catalysis B: Environmental* **2014,** *156-157*, 166-172.
29. Shukla, A.; Pande, J. V.; Bansiwal, A.; Osiceanu, P.; Biniwale, R. B., Catalytic Hydrogenation of Aqueous Phase Nitrate Over Fe/C Catalysts. *Catalysis Letters* **2009,** *131* (3-4), 451-457.
30. Cheng, I. F.; Muftikian, R.; Fernando, Q.; Korte, N., Reduction of nitrate to ammonia by zero-valent iron. *Chemosphere* **1997,** *35* (11), 2689-2695.
31. Huang, Y. H.; Zhang, T. C., Nitrite reduction and formation of corrosion coatings in zerovalent iron systems. *Chemosphere* **2006,** *64* (6), 937-943.
32. Hu, H.-Y.; Goto, N.; Fujie, K., Effect of ph on the reduction of nitrite in water by metallic iron. *Water Research* **2001,** *35* (11), 2789-2793.
33. Chinthaginjala, J. K.; Thakur, D. B.; Seshan, K.; Lefferts, L., How Carbon-Nano-Fibers attach to Ni foam. *Carbon* **2008,** *46* (13), 1638-1647.
34. Chinthaginjala, J. K.; Bitter, J. H.; Lefferts, L., Thin layer of carbon-nano-fibers (CNFs) as catalyst support for fast mass transfer in hydrogenation of nitrite. *Applied Catalysis A: General* **2010,** *383* (1–2), 24-32.

35. Martin-Gullon, I.; Vera, J.; Conesa, J. A.; González, J. L.; Merino, C., Differences between carbon nanofibers produced using Fe and Ni catalysts in a floating catalyst reactor. *Carbon* **2006,** *44* (8), 1572-1580.

36. Rodriguez, N. M.; Chambers, A.; Baker, R. T. K., Catalytic Engineering of Carbon Nanostructures. *Langmuir* **1995,** *11* (10), 3862-3866.

37. Serp, P.; Corrias, M.; Kalck, P., Carbon nanotubes and nanofibers in catalysis. *Applied Catalysis A: General* **2003,** *253* (2), 337-358.

38. García-Diéguez, M.; Pieta, I. S.; Herrera, M. C.; Larrubia, M. A.; Alemany, L. J., Nanostructured Pt- and Ni-based catalysts for CO2-reforming of methane. *Journal of Catalysis* **2010,** *270* (1), 136-145.

39. de Sousa, F. F.; de Sousa, H. S. A.; Oliveira, A. C.; Junior, M. C. C.; Ayala, A. P.; Barros, E. B.; Viana, B. C.; Filho, J. M.; Oliveira, A. C., Nanostructured Ni-containing spinel oxides for the dry reforming of methane: Effect of the presence of cobalt and nickel on the deactivation behaviour of catalysts. *International Journal of Hydrogen Energy* **2012,** *37* (4), 3201-3212.

40. Portnoi, V. K.; Leonov, A. V.; Mudretsova, S. N.; Fedotov, S. A., Formation of nickel carbide in the course of deformation treatment of Ni-C mixtures. *The Physics of Metals and Metallography* **2010,** *109* (2), 153-161.

41. García-Cerda, L. A.; Bernal-Ramos, K. M.; Montemayor, S. M.; Quevedo-López, M. A.; Betancourt-Galindo, R.; Bueno-Báques, D., Preparation of hcp and fcc Ni and Ni/NiO Nanoparticles Using a Citric Acid Assisted Pechini-Type Method. *Journal of Nanomaterials* **2011,** *2011*, 1-6.

42. Macdonald, T.; Xu, J.; Elmas, S.; Mange, Y.; Skinner, W.; Xu, H.; Nann, T., NiO Nanofibers as a Candidate for a Nanophotocathode. *Nanomaterials* **2014,** *4* (2), 256-266.

43. Gonzalez-DelaCruz, V. M.; Holgado, J. P.; Pereñíguez, R.; Caballero, A., Morphology changes induced by strong metal–support interaction on a Ni–ceria catalytic system. *Journal of Catalysis* **2008,** *257* (2), 307-314.

44. Matatov-Meytal, Y.; Shindler, Y.; Sheintuch, M., Cloth catalysts in water denitrification: III. pH inhibition of nitrite hydrogenation over Pd/ACC. *Applied Catalysis B: Environmental* **2003,** *45* (2), 127-134.

45. Rase, H. F., *Handbook of Commercial Catalysts: Heterogeneous Catalysts*. CRC Press: 2000; p 488.
46. Montes, M.; Penneman de Bosscheyde, C.; Hodnett, B. K.; Delannay, F.; Grange, P.; Delmon, B., Influence of metal-support interactions on the dispersion, distribution, reducibility and catalytic activity of Ni/SiO2 catalysts. *Applied Catalysis* **1984,** *12* (4), 309-330.
47. Alzamora, L. E.; Ross, J. R. H.; Kruissink, E. C.; van Reijen, L. L., Coprecipitated nickel-alumina catalysts for methanation at high temperature. Part 2.-Variation of total and metallic areas as a function of sample composition and method of pretreatment. *Journal of the Chemical Society, Faraday Transactions 1: Physical Chemistry in Condensed Phases* **1981,** *77* (3), 665-681.
48. Gil, A.; Diaz, A.; Montes, M., Passivation and reactivation of nickel catalysts. *Journal of the Chemical Society, Faraday Transactions* **1991,** *87* (5), 791-795.
49. Bartholomew, C. H.; Farrauto, R. J., Chemistry of nickel-alumina catalysts. *Journal of Catalysis* **1976,** *45* (1), 41-53.
50. Oyama, S. T., Preparation and catalytic properties of transition metal carbides and nitrides. *Catalysis Today* **1992,** *15* (2), 179-200.
51. Lee, J. S.; Yeom, M. H.; Lee, D. S., Catalysis by Molybdenum Carbide in Activation of C-C, C-O and C-H bonds. *Journal of Molecular Catalysis* **1990,** *62* (3), L45-L51.
52. Leclercq, L.; Provost, M.; Pastor, H.; Leclercq, G., Catalytic properties of transition metal carbides. *Journal of Catalysis* **1989,** *117* (2), 384-395.
53. Frauwallner, M.-L.; López-Linares, F.; Lara-Romero, J.; Scott, C. E.; Ali, V.; Hernández, E.; Pereira-Almao, P., Toluene hydrogenation at low temperature using a molybdenum carbide catalyst. *Applied Catalysis A: General* **2011,** *394* (1–2), 62-70.

Chapter 5

Hydrogen peroxide decomposition in a microreactor: effect of bubble formation on reaction rate

Abstract

H_2O_2 decomposition experiments on Pt were performed in a glass microreactor that simulated arrays of catalyst pores. The formation of bubbles inside the model pores was followed with an optical microscope. It was found that the bubble initiation time strongly depends on the diffusion length and the H_2O_2 concentration. The amount of catalyst did not have a significant effect, suggesting that the reaction is diffusion limited. Results showed that bubble formation can decrease the reaction rate by physically blocking the active sites, but also can accelerate the reaction by creating a forced convective flow inside the nanochannels due to bubble migration. This behaviour is likely to occur in a real catalyst and thus, a smart design of the catalytic support could be used to enhance reaction rates.

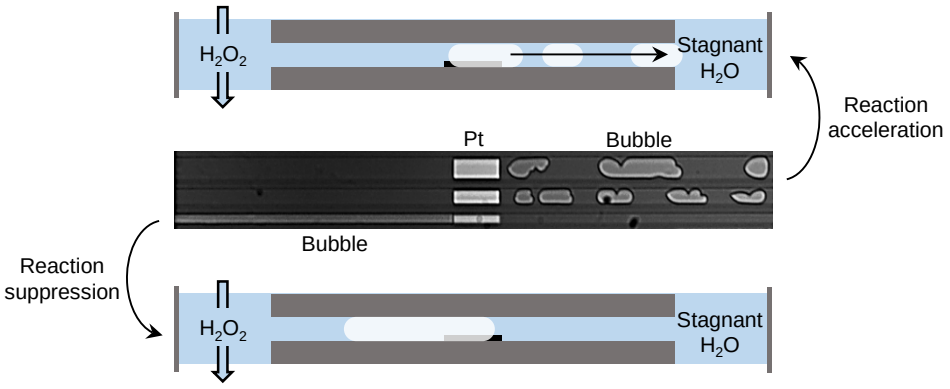

1. Introduction

Heterogeneous catalysis is a multidisciplinary subject, merging the fields of physics and chemistry. Over the last decades, advanced techniques have been developed to gain new insights in the fundamentals of catalysis and the reaction mechanisms. Chemical processes on the surface of catalysts, as well as the influence of the surface structure are increasingly understood. However, there is still an important lack of understanding of the processes occurring inside catalyst pores as direct observations are generally not available.

As described by Thiele [1] and Zeldovich [2] in 1939, a reaction inside a catalyst pore combines diffusion of the reactants and products, as described *e.g.* by Fick's law, and the catalytic reaction on the active sites supported on the pore wall. It is assumed that the liquid inside the catalyst pores remains stagnant, inducing slow molecular diffusion of reactants from the pore mouth to active sites deeper in the pore, leading to decreasing reactant concentration and thus reaction rate [3-6].

However, the Thiele/Zeldovich description does not apply for the chemical reactions where an important amount of gas or heat is generated and cannot be removed *via* diffusivity or thermal conductivity respectively [7-16]. In these cases, gas or vapour bubbles may be generated if their partial pressure exceeds the maximum pressure in the pores. These bubbles grow and displace the liquid inside the pore towards the bulk of the reactor. Once a bubble reaches the pore mouth, the pressure of the bubble equilibrates with the pressure of the reactor, dragging new liquid inside the pore [8-10, 14]. This creates a chaotic movement of the liquid inside the pore network of the catalyst with velocities that can reach 100 m/s [8-10]. This behaviour was described theoretically by Datsevich and was named the 'oscillation theory' [9].

One of the most remarkable consequences of this oscillatory movement is the enhancement of the external (500-fold increase) [7-10, 14] and internal mass transport (mainly in the outer shell of the catalyst particles) [7, 8, 10]. Other

peculiarities are the notorious increase in the temperature difference between the centre and the surface of the catalyst (almost one order of magnitude higher than predicted by the Thiele/Zeldovich model) [10, 11] and the change in reaction orders [9, 10]. However, this chaotic movement of the liquid only happens near the pore mouth, leading to stagnant zones at the deeper parts of the pores, where the reaction is suppressed [10]. Furthermore, it can also damage the catalyst due to cavitation in the pores [14].

These concepts have been proven experimentally based on kinetic data but a visualization of gas bubbles and liquid motion inside the pores is still lacking. In this work we study the catalytic decomposition of hydrogen peroxide (H_2O_2) on Pt in a glass chip that models an array of catalyst pores. H_2O_2 decomposition was chosen as model reaction since it is a fast reaction in aqueous phase, forming a gaseous product (O_2) without any side reactions [16, 17]. The formation and behaviour of bubbles was observed with an optical microscope. The study reports on the effect of the geometry of the nanochannel, the amount of catalyst and the H_2O_2 concentration on the formation of bubbles and the impact of those on the reaction rate.

2. Experimental:

2.1. Chip fabrication

The nano –and microfluidic channels were fabricated on two separate substrates and then bonded. The bottom substrate (figure 2A) contains the nanochannels, which have a Pt patch on the bottom. The top substrate (figure 2B) contains the microchannels and the access holes.

A <100> silicon wafer (figure 2A-1) was thermally oxidized to obtain a layer of 450 nm SiO_2 (figure 2A-2). This thickness defines the depth of the nanochannels. Nanochannels were then patterned by UV lithography and the exposed SiO_2 was

etched in a buffered hydrofluoric acid (BHF) solution composed of hydrofluoric acid (HF) and ammonium fluorite (NH_4F) until the silicon surface was reached (figure 2A-3). A second UV lithography step was performed to create the catalyst patch area (figure 2A-4). Afterwards, a layer of Ti/Pt was deposited by sputtering (figure 2A-5). The excess metal was removed by a lift-off process (figure 2A-6).

The top substrate consists of a 500 μm thick borofloat glass wafer (figure 2B-1). A Cr/Au layer was deposited to act as an etching mask during the glass etching process (figure 2B-2). Next, the microchannel pattern was defined and the wafer was etched in 25% HF solution to create 100 μm deep microchannels (figure 2B-3). Through holes were made from the back side of the wafer by powderblasting of 29 μm diameter alumina grid (figure 2B-5).

Both substrates were cleaned thoroughly, aligned and pressed together (figure 2C). Finally, the stack was annealed in a furnace at 450 °C. The resulting chip is shown in figure 3a.

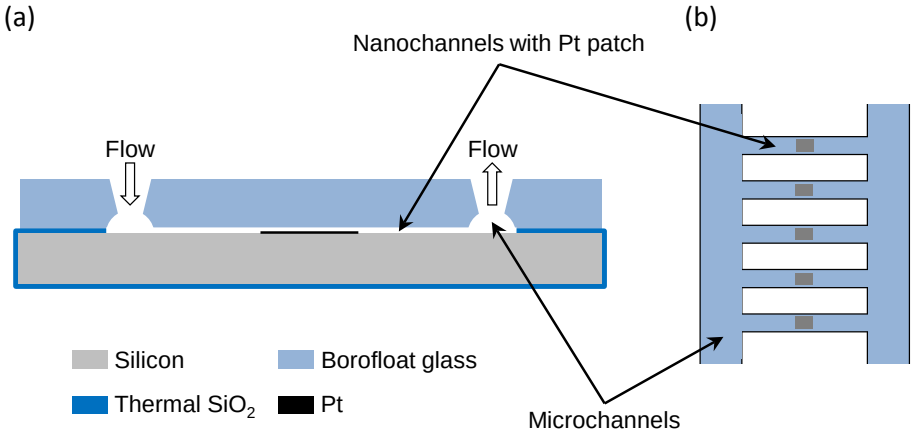

Figure 1: a) Cross-sectional and b) top view of the chip.

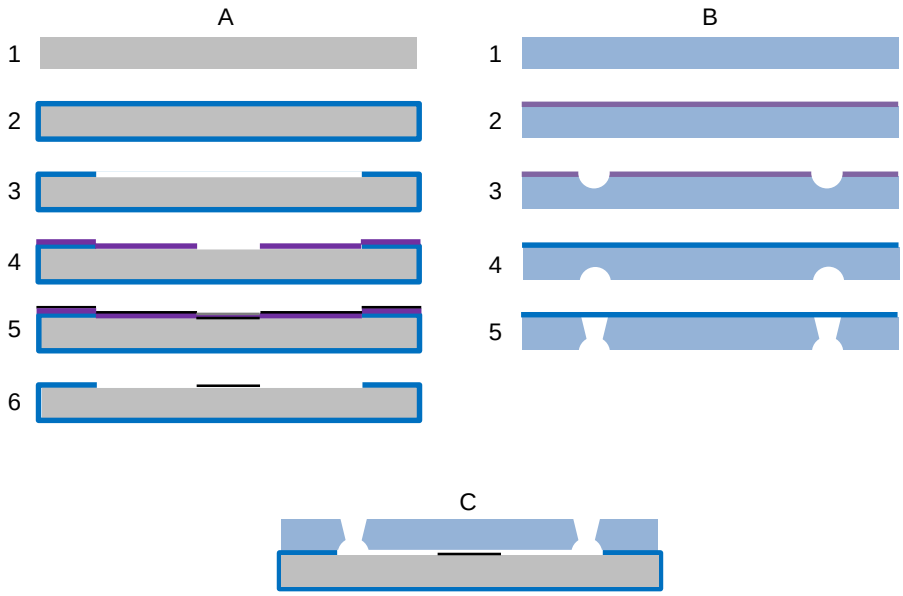

Figure 2: Schematic description of the fabrication steps of the chip.

2.2. Description of the chip

The fabricated chip (figure 3a) consists of two symmetric meandering microchannels interconnected with an array of 96 parallel nanochannels varying in width, length and amount of catalyst. The shortest nanochannels are positioned in the center of the chip. The other nanochannels are distributed symmetrically at both sides of the shortest nanochannels with the exception of the longest set of nanochannels, which are only present at one side. The different nanochannel lengths are 2900, 8500, 14000, 20000 and 25000 μm. For every length there are four different widths: 10, 30, 50 and 70 μm (figure 3b). For every width there are three different Pt sizes, varying in length (35, 250 and 3140 μm). All Pt patches have a height of 10 nm and a width 4 μm narrower than the nanochannel. The shortest nanochannels have shorter Pt lengths (35, 180 and 250 μm). For a full overview of all dimensions of the nanochannels used in this work, and the Pt catalysts, see Table D1 in Appendix D.

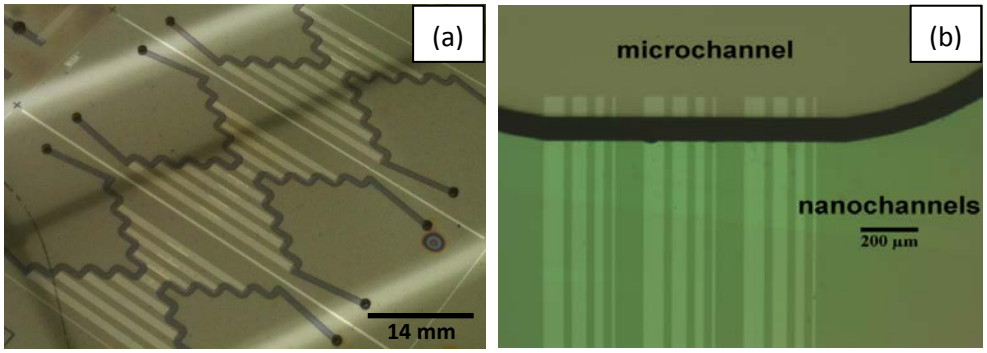

Figure 3: a) Picture of the final device prior to dicing, b) Optical microscope image of the microchannels substrate aligned and fusion bonded to the nanochannels substrate.

2.3. Catalytic tests

MiliQ water contained in a glass bottle was degassed to remove any trace of gases. Next, the miliQ water was introduced into the chip and placed in a metallic holder (Micronit ®Fluidic connect pro). The water flow was generated *via* a hydrostatic pressure of 0.4 bar. The water was first directed to one of the microchannels and then to the other *via* a PEEK tubing that connected both microchannels in series. The nanochannels were filled by capillarity. After 24 h flowing water through the chip to ensure full wetting, one of the microchannels was bypassed and closed, keeping water flow only on one microchannel. Next, water was replaced by a H_2O_2 solution, as shown in figure 4. The experiments were designed in this way to supply H_2O_2 to the catalyst *via* molecular diffusion exclusively, ensuring the liquid in the nanochannels is stagnant. Co-feeding H_2O_2 *via* both microchannels in parallel or connecting both microchannels in series resulted in some convection inside the nanochannels.

Experiments were all performed at room temperature (20 °C) with different H_2O_2 concentrations (0, 0.04, 0.13, 0.64, 1.49 and 2.35 mol/L). A microscope (Nikon, Eclipse L150) equipped with a camera (PCO Pixelfly) was positioned above the chip to record formation of any bubbles. The amount of O_2 formed was estimated

from the volume of the bubbles. The volume of a bubble was calculated as the product of the axial cross-sectional area of the bubble and the height of the nanochannel. This value results in a slight overestimation since it does not consider the curvature of the bubble.

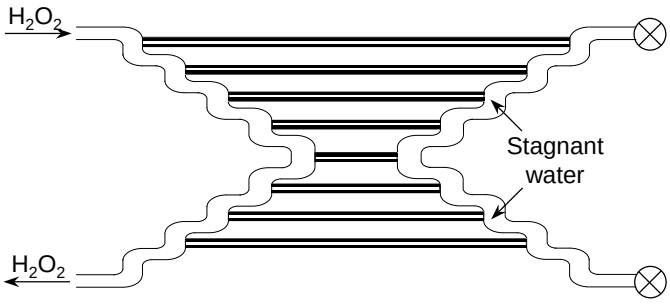

Figure 4: Flow operation of the chip during reaction.

2.4. Equations

Molecular diffusion fluxes of H_2O_2 and O_2 were calculated based on Equation 1, assuming no transport due to convection.

$$J = -D * \frac{\Delta C}{\Delta l} \qquad \text{Equation 1}$$

Where J is the diffusion flux in mol * s^{-1} * m^{-2}, D is the diffusion coefficient of H_2O_2 or O_2 in water in m^2 * s^{-1}, ΔC de concentration gradient of H_2O_2 or O_2 in mol * m^{-3} and Δl the diffusion length in m.

The rate of O_2 formation can be estimated with Equation 2.

$$R = k * [H_2O_2]^{\alpha} * (W_{Pt} * L_{Pt}) \qquad \text{Equation 2}$$

Where R is the reaction rate in mol * s^{-1} * m^{-3}, k the rate constant in mol * s^{-1} * m^{-2}, $[H_2O_2]$ the concentration of H_2O_2 in mol * m^{-3}, α the reaction order (assumed 1) [16], W_{Pt} and L_{Pt} the width and the length of the Pt patch respectively, both in m.

The Laplace pressure between the inside and outside surface of an O_2 bubble was calculated with the Young-Laplace equation (Equation 3).

$$\Delta P = \gamma * \left(\frac{1}{R_1} + \frac{1}{R_2}\right) \quad \text{Equation 3}$$

Where ΔP is the Laplace pressure in Pa, γ is the surface tension (0.072 N/m for pure water) and R_1 and R_2 the two radii of curvature of the bubble in m.

The maximum O_2 concentration in the liquid inside the nanochannel is determined by the Henry´s law (Equation 4):

$$[O_2] = H_{O_2} * (P_{reactor} + \Delta P) \quad \text{Equation 4}$$

Where $P_{reactor}$ is the pressure in the microchannel (1 bar) and H_{O_2} is the Henry's coefficient for pure O_2 in water.

3. Results

The experiments performed with 0.64, 1.49 and 2.35 mol H_2O_2/L presented bubbles in all nanochannels. No bubbles were observed within 5 h of reaction in the case of low H_2O_2 concentrations (0.04 and 0.13 mol H_2O_2/L). It was observed that the time needed for initiation of bubble formation strongly varies for different nanochannels and for the different H_2O_2 concentrations studied. Figure 5 shows a typical example of bubble formation at different times. Notice that the bright rectangles located at the centre of the nanochannels correspond to the Pt patches while the light grey areas at either right or left side of the Pt correspond to the bubbles. The full size of the bubbles cannot be seen in all cases due to the high magnification.

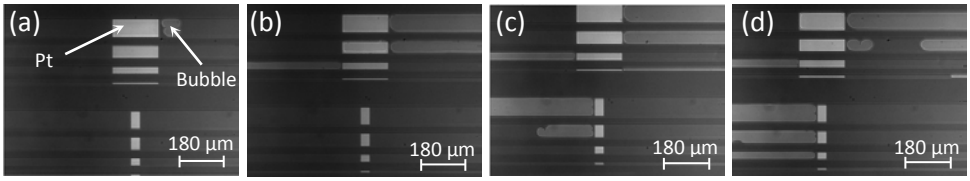

Figure 5: Bubble formation in the shortest nanochannels (2900 µm), with two different platinum lengths (35 and 180 µm) and four different widths (10, 30, 50 and 70 µm) using 0.64 mol H_2O_2/L after a) 1h18min, b) 1h35min, c) 1h45min, d) 1h53min.

Figures 6a and b show the effect of the diffusion length (distance from the microchannel to the Pt front) on the time needed to initiate bubble formation for the experiments performed with 0.64 and 1.49 mol H_2O_2/L. It reveals that bubbles initiation time increases with the diffusion length. This is observed independently of the amount of Pt and the width of the nanochannel. Figures 6a and b also show that the length of the Pt has no significant effect on the bubble initiation time. The only exception is the shortest Pt length (35 µm) for the experiment with 0.64 mol H_2O_2/L, which exhibits longer initiation times than the other Pt lengths (figure 6a). The same behaviour can be observed in figure D1 in supporting information.

Figure 7 shows the effect of the nanochannel width on the bubble initiation time for the experiment performed with 0.64 mol H_2O_2/L. It can be observed that the width of the nanochannel has only a weak effect on the bubble initiation time as compared to the diffusion length. For narrower nanochannels, bubble initiation time is slightly shorter. This effect was observed independently of the amount of Pt or the H_2O_2 concentration.

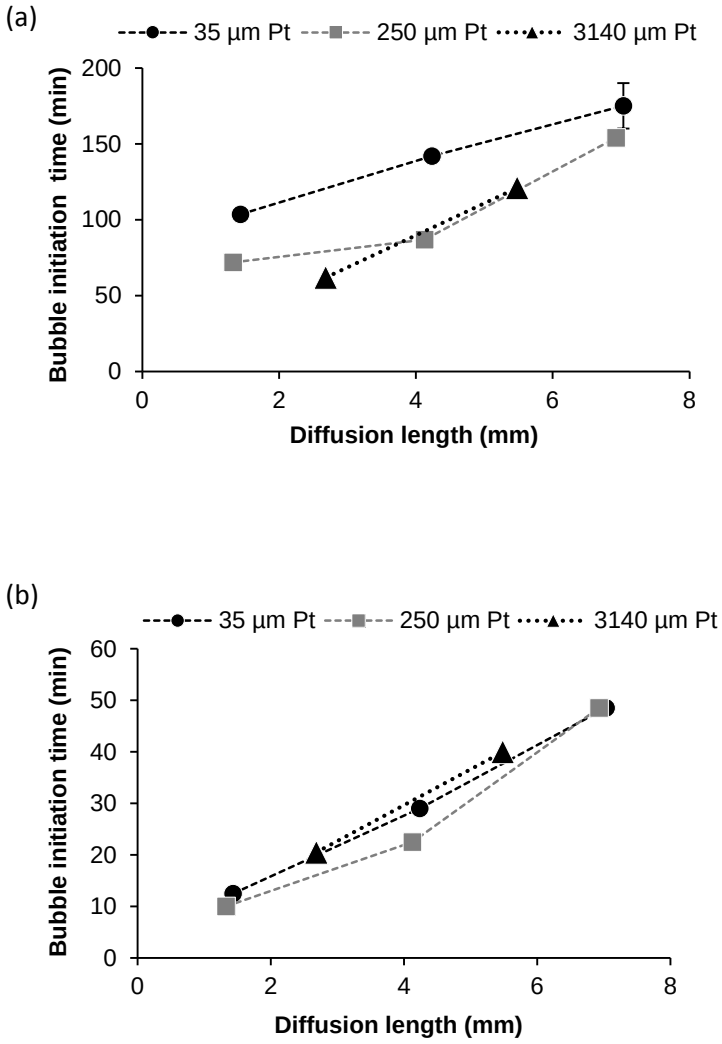

Figure 6: Effect of the diffusion length and the Pt length on the bubble initiation time for a constant nanochannel width of 70 µm and different Pt lengths (35, 250 and 3140 µm). The experiments were performed with a) 0.64 mol H_2O_2/L, b) 1.49 mol H_2O_2/L.

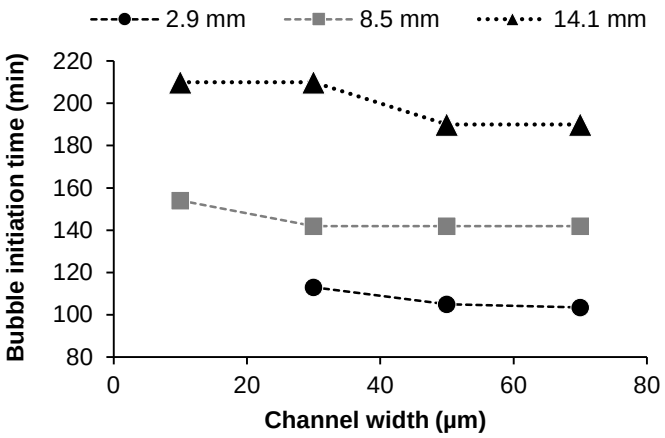

Figure 7: Effect of the nanochannel width on the bubble initiation time for a constant Pt patch length of 35 μm and different nanochannel lengths (2.9, 8.5 and 14.1 mm). The experiment was performed with 0.64 mol H_2O_2/L.

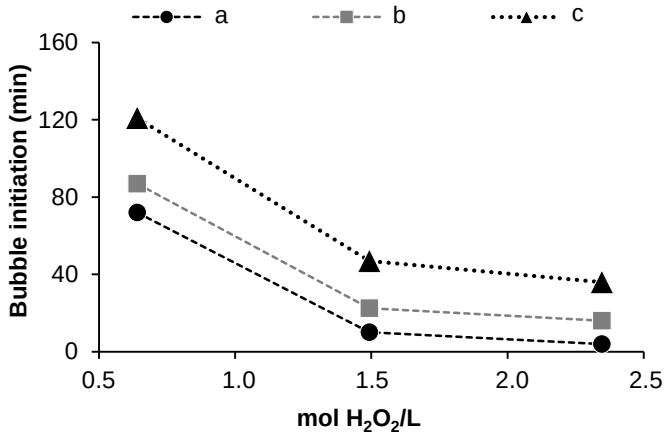

Figure 8: Effect of the H_2O_2 concentration on the bubble initiation time, a) 2.9 mm nanochannel length, 70 μm nanochannel width and 250 μm Pt patch length; b) 8 .5 mm nanochannel length, 70 μm nanochannel width and 250 μm Pt patch length; c) 14.1 mm nanochannel length, 70 μm nanochannel width and 3140 μm Pt patch length.

Figure 8 shows that bubble formation occurs faster at high H_2O_2 concentrations. At concentrations below 0.13 mol H_2O_2/L, no bubbles were observed within 5 hours of experiment. For the concentrations 0.64, 1.49 and 2.35 mol H_2O_2/L, all nanochannels showed bubbles and presented similar trends in bubble initiation time.

Figure 9 shows that bubble formation can occur in both directions *i.e.,* towards the microchannel filled with stagnant water as well as towards the microchannel filled with the H_2O_2 solution. In few nanochannels, bubbles also grow in both directions simultaneously but in most cases bubbles form either in one or the other direction.

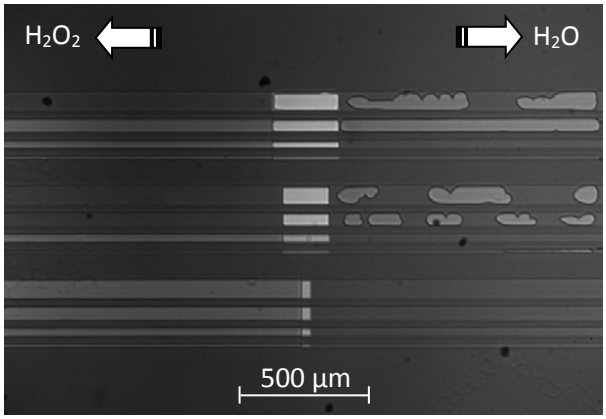

Figure 9: Nanochannels with a length of 2.9 mm after 5.5 h of experiment with a solution of 0.64 mol H_2O_2/L

Figure 10 shows that bubbles forming towards the microchannel filled with H_2O_2 have a growth rate that decreases abruptly during the initial minutes of reaction, becoming extremely low at long reaction times. The rate of formation is estimated based on the volume of the gas bubbles that are observed (see section 3.3). The initial values of the O_2 formation rate are overestimated since they include the O_2 required to saturate the liquid before bubble nucleation occurs.

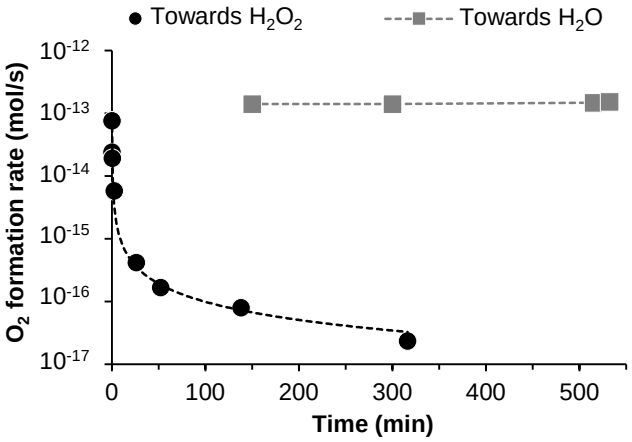

Figure 10: Evolution of O_2 formation rate in time for two nanochannels forming bubbles towards different directions. Experiment was performed with 0.64 mol H_2O_2/L. Both nanochannels were 2.9 mm long, 50 μm wide and Pt lengths of 35 μm (towards H_2O_2) and 180 μm (towards H_2O).

Figure 10 also shows that when bubbles form towards the microchannel filled with water, reaction rates are various orders of magnitude higher than when bubbles form towards the microchannel filled with H_2O_2. Furthermore, reaction rates stay constant after more than 500 min of reaction. These bubbles form above the catalyst patch and continuously grow until the catalyst is entirely covered. A fraction of the bubble detaches and migrates to the microchannel. The bubble remaining above the Pt continues growing and the process repeats (Figure E1 in Appendix E).

4. Discussion

4.1. Bubble formation

Catalytic decomposition of H_2O_2 occurs at the Pt patches deposited in the centre of the nanochannels, producing water and O_2 as the only products of the reaction

(Equation 5). As result of the balance between the diffusion of H_2O_2 and O_2, and the reaction rate, concentration profiles will develop in time along the nanochannels, leading to a pseudo steady state. At pseudo steady state, the highest O_2 concentration in the nanochannel will occur above the Pt patch. If this O_2 concentration is higher than the O_2 saturation concentration, bubbles will form. For lower O_2 concentrations, no bubbles will form.

$$2\ H_2O_2 \xrightarrow{\text{Catalyst}} 2\ H_2O + O_2 \qquad \text{Equation 5}$$

No bubbles were observed in the experiments with 0.04 and 0.13 mol H_2O_2/L. This indicates that the maximum O_2 concentration above the Pt was lower than 5.5 mol O_2/m^3. This value is larger than the saturation concentration at 1 bar (1.3 mol O_2/m^3) due to the high curvature of the bubbles induced by their confinement (estimated from Equation 4; $H_{O_2} = 1.3 * 10^{-5}$ mol * m^{-3} * bar^{-1} [18]). Therefore, the maximum O_2 flux (J_{O_2} max) without formation of bubbles can be derived from Equation 1 (J_{O_2} max = D_{O_2}* 5.5/Δx).

According to figure 6a (0.64 mol H_2O_2/L), the amount of Pt has a minor effect on the bubble initiation time, especially for the medium (250 μm) and large Pt patches (3140 μm). For higher H_2O_2 concentrations (1.49 mol H_2O_2/L), the bubble initiation time was not influenced by the amount of Pt in the nanochannel, even for the small Pt patches (figure 6b). Thus, the reaction is diffusion limited and by-passing of H_2O_2 over the Pt patch is negligible. Therefore, the concentration profiles of O_2 and H_2O_2 in the nanochannels can be depicted as in figure 11. It is worth stressing that, before bubble formation, the O_2 concentration in the microchannels is negligible.

Since the reaction is fast and H_2O_2 reaching the Pt is completely converted to O_2 in most cases, the balance between the H_2O_2 flux ($J_{H_2O_2}$= $D_{H_2O_2}$*[H_2O_2]/Δx) and the J_{O_2} max will determine whether bubbles will form or not above the Pt patch (Equation

6). For ratios greater than 1, bubbles are expected to form while for ratios lower than 1, O_2 will stay dissolved in the liquid.

$$\frac{0.5 * J_{H_2O_2}}{2 * J_{O_2\,max}} = \frac{D_{H_2O_2} * \frac{\Delta[H_2O_2]}{\Delta x} * A}{D_{O_2} * \frac{\Delta[O_2]}{\Delta x} * A * 4} = \frac{D_{H_2O_2} * [H_2O_2]}{[O_2]_{sat} * D_{O_2} * 4}$$ Equation 6

$D_{H_2O_2}$ (9.8 * 10^{-10} m^2/s, [19]) and D_{O_2} (2.0 * 10^{-9} m^2/s, [20]) are the diffusion coefficients of H_2O_2 and O_2 in water respectively, $\Delta[H_2O_2]$ and $\Delta[O_2]$ are the concentration gradients (in mol/m^3), Δx is the diffusion distance (in m) and A is the diffusion area (in m^2). The J_{O_2} max is corrected by a factor of two because O_2 diffuses in two directions (towards both microchannels) and the $J_{H_2O_2}$ is corrected by a factor of 0.5 because of the stoichiometry of the reaction.

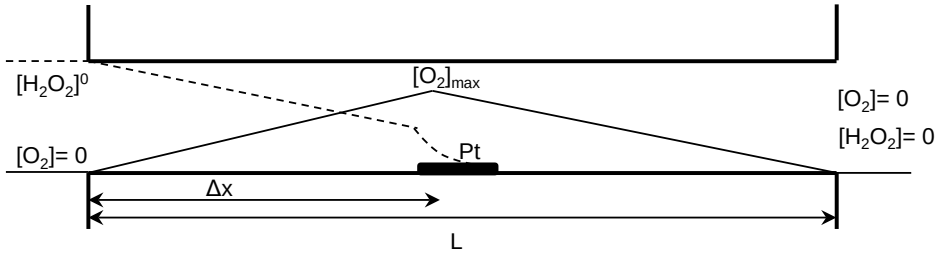

Figure 11: O_2 and H_2O_2 concentration profiles inside a nanochannel in case of a high reaction/diffusion rate ratio.

Table 1 shows that bubbles are expected to form for all H_2O_2 concentrations higher than 0.04 mol/L since their corresponding ratios are greater than 1. However, for the experiment with 0.13 mol H_2O_2/L, no bubbles were observed experimentally. This could be attributed to an underestimation of the O_2 flux caused by higher O_2 concentrations above the Pt. This is supported by the observation that the top surface of the nanochannel is bended, generating higher confinement of the liquid and thus, higher O_2 saturation concentrations. Another option is that the flux of H_2O_2 is overestimated since molecular diffusion is only considered in one dimension and any H_2O_2 concentration gradients perpendicular above the Pt patch are ignored. Even though this could support the absence of bubbles in the

experiment with 0.13 mol H_2O_2/L, it is also possible that bubbles did not form because the experimental time (5-6 h) was too short and the two competing diffusion processes did not reach steady state.

Table 1: Ratio from Equation 6 for all the H_2O_2 concentrations tested.

H_2O_2 concentration (mol/L)	$J_{H_2O_2}/(4*J_{O_2MAX})$
0.04	0.9
0.13	2.9
0.64	14.5
1.49	33.7
2.35	53.1

Notice that Equation 6 and Figure 11 imply that the reaction is fast as compared to diffusion and consequently the formation of bubbles only depends on the H_2O_2 concentration and not on the amount of catalyst or the geometry of the nanochannel. This is in agreement with the observation that the experiments with 0.04 and 0.13 mol H_2O_2/L do not exhibit bubbles in any of the nanochannels while the experiments with 0.64, 1.49 and 2.35 mol H_2O_2/L, present bubbles in all the nanochannels.

4.2. Effect of bubble direction on reaction rate

Bubble formation does not occur in any preferential direction. As shown in figure 12, the number of bubbles growing towards the H_2O_2 microchannel (46%) is almost the same as the number growing towards the water microchannel (48%). A small fraction of the nanochannels (6%) present a bubble that grows in both directions. This clearly indicates that the transport of H_2O_2 towards the Pt occurs only *via* molecular diffusion and not by convective flow due to capillary forces inside the nanochannels, otherwise all bubbles would grow and move in the same direction.

When bubbles form towards the microchannel containing H_2O_2, the rate of bubble formation decreases exponentially, as shown in figure 10. The growth rate

decreases because the presence of bubbles suppresses the supply of H_2O_2 by physically blocking the diffusion of the reactant molecules to the catalytic sites. Nevertheless, bubbles do not stop growing completely. This could be attributed to the presence of a thin stagnant layer of water on the walls of the nanochannel at the position of the bubble. This layer might enable very slow transport of H_2O_2 to the Pt patch. Alternatively, it could also be that bubbles continue growing due to reaction of H_2O_2 molecules that by-passed the Pt patch before bubble formation started, in the case of small Pt patches.

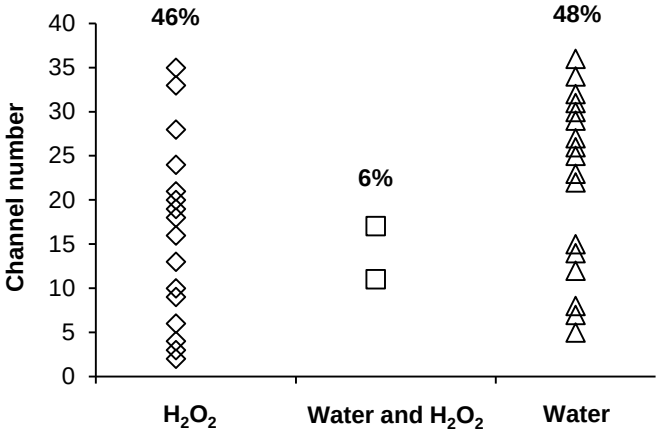

Figure 12: Direction of bubble formation (towards microchannel filled with water or H_2O_2) in the 36 different nanochannels studied during the experiment with a solution of 0.64 mol H_2O_2/L. Percentages indicate the fraction of nanochannels for each direction.

On the other hand, if bubbles form towards the microchannel with stagnant water, the formation rate of bubbles is high and remains high, even after hours of reaction (figure 10). The movement of these bubbles displaces liquid, which is immediately replaced by fresh H_2O_2 solution from the other microchannel, creating a forced convection of the liquid. As result, the reaction rate increases several orders of magnitude as compared to the case where H_2O_2 transport occurs only *via* molecular diffusion. For example, the maximum O_2 formation rate (assuming complete conversion on the Pt patch) achievable under molecular diffusion for the

experiment shown in figure 10 (towards H_2O) would be 4.8 * 10^{-15} mol O_2/s (equation 1). However, the experimental reaction rate is 1-2 orders of magnitude higher (≈ 1.5 * 10^{-13} mol O_2/s). We speculate that the oxidized Pt surface is more hydrophilic than the SiO_2 in the nanochannel walls. As a consequence, bubbles migrate from the Pt to the nanochannel, decreasing surface tension. The energy released during the reaction might also play a role in the movement of the bubbles.

From the linear velocity of the bubbles, the convective flow of the liquid and therefore the H_2O_2 flux to the Pt catalyst can be calculated. It can be estimated that 28% of the H_2O_2 transported to the Pt patch is converted in the nanochannel shown in figure 10 (towards H_2O). For further details on the calculations, see Appendix F. These results confirm that the high O_2 formation rates can be explained by H_2O_2 transport *via* forced convection.

The apparent kinetic constant was calculated from the observed reaction rate and the amount of Pt in the nanochannel shown in figure 10 (towards H_2O), using the average H_2O_2 concentration above the catalyst and assuming that all Pt contributes to the reaction (equation 2). The value obtained is more than 7 orders of magnitude higher than the values reported in literature (Table 2); it should be noted that the estimated rate is even an underestimation because only a part of the Pt patch actually contributes to the reaction. The values were compared under the same temperature and similar H_2O_2 concentrations. We speculate that these extreme differences might be caused by the completely different morphology of the Pt catalysts, namely flat Pt surface for the current work, and Pt nanoparticles and Pt powder for references [21] and [17] respectively. Similar results have been reported in literature for the direct synthesis of H_2O_2 with Pd catalyst. It was proven that Pd surfaces exposing specific planes, *i.e.* (100) [22] and (110) [23], exhibit activities per m^2 several orders of magnitude higher than some of the best powder catalysts. On the other hand, it is also possible that kinetic data reported so far for porous catalysts is strongly influenced by pore blockage by O_2 bubbles.

Table 2: Comparison between calculated kinetic constants from the current work and literature.

k bubbles ($min^{-1} * cm^{-2}$)	k [17] ($min^{-1} * cm^{-2}$)	k G10Pt [21] ($min^{-1} * cm^{-2}$)	k P10Pt [21] ($min^{-1} * cm^{-2}$)
$3.9 * 10^{4}$	$1.9 * 10^{-3}$	$4.1 * 10^{-5}$	$1.0 * 10^{-6}$

4.3. Bubble initiation time

The experimental results demonstrate that bubble initiation time is strongly affected by the diffusion length (figure 6) and the concentration of H_2O_2 in the feed stream (figure 8). All these parameters have an effect on the diffusion fluxes of H_2O_2 and O_2 (Equation 1) and/or the kinetics of the reaction (Equation 2).

The diffusion distance is inversely proportional to the diffusion flux (Equation 1). Consequently, long diffusion distances will slow down the transport of H_2O_2 to the catalyst and the transport of O_2 to the microchannels. In this case, longer times will be needed to fully develop the concentration profiles inside the nanochannels and consequently, the time of bubble formation will be increased, as shown in figure 6. As mentioned in section 4.1, the diffusion distance will not determine the formation of bubbles (Equation 6) but only the time needed for bubble nucleation to occur.

Increasing the H_2O_2 concentration accelerates bubble nucleation (figure 8), *via* increasing the H_2O_2 diffusion flux (Equation 1) and the reaction rate (Equation 2). Since the reaction is exothermic (ΔH=-98.2 kJ/mol [16]), an increase in reaction rate will also lead to an increase in temperature. The adiabatic temperature rise of the liquid above the Pt surface (calculated from the reaction enthalpy and the heat capacity of water) was estimated only for the experiment with 0.64 mol H_2O_2/L, giving values between 3.5 and 6 °C, depending on the nanochannel. Therefore, it can be concluded that exothermic effect will have only a minor influence on the reaction kinetics and solubility of O_2, as the experimental temperature rise will be significantly smaller because of dissipation of heat *via* the Pt patch to the SiO_2

substrate. This is in agreement with the results reported by Datsevich et al. [16] who observed temperature changes in the range of 1 °C.

The width of the nanochannel does not influence the transport of H_2O_2 and O_2 since the diffusion flux is independent of the area of diffusion. However, figure 7 shows a small increase in the time of bubble formation for the narrowest nanochannels. This phenomenon occurs because the amount of Pt does not scale with the width of the nanochannel. The distance between the Pt patch and side walls of the nanochannels is always 2 μm, therefore, narrow nanochannels contain relatively less Pt than wide nanochannels.

The bubble initiation time is not affected by the length of the Pt patch at constant diffusion length and H_2O_2 concentration. This confirms that the diffusion is the rate limiting step, since in a kinetically limited system, longer Pt lengths would lead to higher reaction rates and thus, faster bubble nucleation times. Only the smallest Pt patches (35 μm) in the experiment with 0.64 mol H_2O_2/L (figure 6a) show slightly longer bubble initiation time, probably due to incomplete H_2O_2 conversion.

4.4. Model catalyst pore

The results presented in this work demonstrate that formation of bubbles in porous catalyst supports influences the apparent activity of the catalyst. Surprisingly, both retardation as well as enhancement of the activity are observed.

Decreasing the apparent activity by blocking the access of the reactants to the catalytic active sites with bubbles is an effect that can intuitively be expected if the bubble covers the catalyst surface. Blockage can also occur if the bubble obstructs the pore by remaining between the reactants supply and the catalyst particles, causing isolation of the catalyst. The latter will not happen in real catalysts where the reactants supply occurs from both sides of the pore due to 3D network structures. Analogously, supports with homogeneous catalyst distribution along

the pore would also prevent complete isolation of the catalyst. However, some supports may also present 1D/2D structures with dead pore ends (active carbon) and/or mal-distribution of the catalyst and could then be qualitatively described by the model pores shown in this study.

The observation that the reaction rate can also be enhanced thanks to bubble formation is in agreement with the oscillation theory described by Datsevich [8]. However, the mechanism he reported differs from the mechanism occurring in our study. As explained in section 1, Datsevich suggested that once the growing bubble reaches the pore mouth, the pressure of the bubble will equilibrate with the pressure of the reactor and would drag new liquid inside the pore. However, we show here that the energy released during the reaction and the differences in hydrophilicity between the Pt and the nanochannel surfaces induce bubble movement, which leads to a liquid displacement. Both mechanisms are likely to happen in a real catalyst pore and can be used to enhance mass transport and reaction rates. However, this requires a significant effort regarding the design and preparation of such practical catalyst supports. For instance, bubble migration could be favoured by using supports that combine hydrophilic and hydrophobic zones [24], or that contain conical pores.

Up to date, conventional descriptions of liquid phase reactions have applied concepts like the Weisz-Prater criteria and the Thiele modulus to compare reaction rates to internal mass transport. In this work, it was demonstrated that liquid phase reactions producing gas bubbles cannot be described using these concepts because of both enhancing as well as retarding effects on the reaction rate due to the formation of bubbles within the pores. Further work is required to develop a model than can describe these reactions.

5. Conclusions

Formation of gas inside the model catalyst pores featured in a glass chip resulted in bubble nucleation above the catalyst patch. The reaction rate decreases

dramatically when the bubbles start growing in the direction of the H_2O_2 feed stream, almost suppressing the reaction completely. On the other hand, when the bubbles grow towards the opposite direction of the feed stream, a forced convective flow is created inside the pores, enhancing the reaction rate 1-2 orders of magnitude. As expected, results showed that at short diffusion distances and high H_2O_2 concentrations, bubble nucleation occurs more rapidly. Instead, an increase in Pt amount did not influence the nucleation time, indicating that the reaction is diffusion limited. These experiments provide direct evidence that reactions generating gas inside pores of supported catalyst cannot be described using the conventional Thiele/Zeldovich description. Future work should focus on the smart design and preparation of catalyst pore structures in order to benefit from the effects of bubble formation.

6. References

1. Thiele, E.W., *Relation between Catalytic Activity and Size of Particle.* Industrial & Engineering Chemistry, 1939. 31(7): p. 916-920.
2. Zeldovitch, Y.B., *To the theory of the reaction on a porous or powder catalyst.* J. Phys. Chem. (USSR), 1939. 13: p. 163-166.
3. Averill, M., van Santen and van Leeuwen ed. *Catalysis: an integrated approach*. Second ed. 2000, Elsevier. 582.
4. Fogler, H.S., *Elements of chemical reaction engineering*. 2006.
5. Klaewkla, R., Arend, M., and Hoelderich, W.F., *A Review of Mass Transfer Controlling the Reaction Rate in Heterogeneous Catalytic Systems*. 2011: INTECH Open Access Publisher.
6. P.A. Ramachandran, R.V.C., ed. *Three phase catalytic reactors*. ed. G.a.B.S. publishers. 1983: New York.
7. Blümich, B., Datsevich, L.B., Jess, A., Oehmichen, T., Ren, X., and Stapf, S., *Chaos in catalyst pores.* Chemical Engineering Journal, 2007. 134(1-3): p. 35-44.
8. Datsevich, L.B., *Alternating motion of liquid in catalyst pores in a liquid/liquid–gas reaction with heat or gas production.* Catalysis Today, 2003. 79-80: p. 341-348.
9. Datsevich, L.B., *Some theoretical aspects of catalyst behaviour in a catalyst particle at liquid (liquid–gas) reactions with gas production: oscillation motion in the catalyst pores.* Applied Catalysis A: General, 2003. 247(1): p. 101-111.
10. Datsevich, L.B., *Oscillations in pores of a catalyst particle in exothermic liquid (liquid–gas) reactions: Analysis of heat processes and their influence on chemical conversion, mass and heat transfer.* Applied Catalysis A: General, 2003. 250(1): p. 125-141.
11. Datsevich, L.B., *Oscillation theory.* Applied Catalysis A: General, 2004. 262(2): p. 149-153.
12. Datsevich, L.B., *Oscillation Theory.* Applied Catalysis A: General, 2004. 273(1-2): p. 151-156.
13. Datsevich, L.B., *Oscillation theory.* Applied Catalysis A: General, 2005. 279(1-2): p. 181-185.
14. Datsevich, L.B., *Oscillation theory.* Applied Catalysis A: General, 2005. 294(1): p. 22-33.
15. Oehmichen, T., Datsevich, L., and Jess, A., *Influence of Bubble Evolution on the Effective Kinetics of Heterogeneously Catalyzed Gas/Liquid Reactions. Part II: Exothermic Gas/Liquid Reactions.* Chemical Engineering & Technology, 2010. 33(6): p. 921-931.

16. Oehmichen, T., Datsevich, L., and Jess, A., *Influence of Bubble Evolution on the Effective Kinetics of Heterogeneously Catalyzed Gas/Liquid Reactions. Part I: Reactions with Gaseous Products.* Chemical Engineering & Technology, 2010. 33(6): p. 911-920.
17. McKee, D.W., *Catalytic decomposition of hydrogen peroxide by metals and alloys of the platinum group.* Journal of Catalysis, 1969. 14(4): p. 355-364.
18. Sander, R., *Compilation of Henry's law constants (version 4.0) for water as solvent.* Atmos. Chem. Phys., 2015. 15(8): p. 4399-4981.
19. Kreja, L., *Der heterogene Zerfall von Wasserstoffperoxid an Platinkatalysatoren*, in *Zeitschrift für Physikalische Chemie*. 1984. p. 247.
20. *CRC Handbook of Chemistry and Physics*. 2014.
21. Kamal, F., Yann, B., Charles, K., and Marie, T., *Decomposition of hydrogen peroxide: influence of the shape of catalyst support*, in *46th AIAA/ASME/SAE/ASEE Joint Propulsion Conference & Exhibit*. 2010, American Institute of Aeronautics and Astronautics.
22. Rossi, U., Zancanella, S., Artiglia, L., Granozzi, G., and Canu, P., *Direct synthesis of H2O2 on model Pd surfaces.* Chemical Engineering Journal, 2012. 207-208: p. 845-850.
23. Centi, G., Perathoner, S., and Abate, S., *Direct Synthesis of Hydrogen Peroxide: Recent Advances*, in *Modern Heterogeneous Oxidation Catalysis*. 2009, Wiley-VCH Verlag GmbH & Co. KGaA. p. 253-287.
24. Franch, C., Lammertink, R.G.H., and Lefferts, L., *Partially hydrophobized catalyst particles for aqueous nitrite hydrogenation.* Applied Catalysis B: Environmental, 2014. 156–157: p. 166-172.

Appendix D: Figures and graphs

Table D1: Nanochannels studied and their characteristics.

Nanochannel ID	Nanochannel length (μm)	Nanochannel width (μm)	Catalyst lenght (μm)	Catalyst width (μm)
L1,1	2900	10	35	6
L1,2	2900	30	35	26
L1,3	2900	50	35	46
L1,4	2900	70	35	66
L1,5	2900	10	175	6
L1,6	2900	30	175	26
L1,7	2900	50	175	46
L1,8	2900	70	175	66
L1,9	2900	10	250	6
L1,10	2900	30	250	26
L1,11	2900	50	250	46
L1,12	2900	70	250	66
L2,1	8500	10	35	6
L2,2	8500	30	35	26
L2,3	8500	50	35	46
L2,4	8500	70	35	66
L2,5	8500	10	250	6
L2,6	8500	30	250	26
L2,7	8500	50	250	46
L2,8	8500	70	250	66
L2,9	8500	10	3140	6
L2,10	8500	30	3140	26
L2,11	8500	50	3140	46
L2,12	8500	70	3140	66
L3,1	14000	10	35	6
L3,2	14000	30	35	26
L3,3	14000	50	35	46
L3,4	14000	70	35	66
L3,5	14000	10	250	6
L3,6	14000	30	250	26
L3,7	14000	50	250	46
L3,8	14000	70	250	66
L3,9	14000	10	3140	6
L3,10	14000	30	3140	26
L3,11	14000	50	3140	46
L3,12	14000	70	3140	66

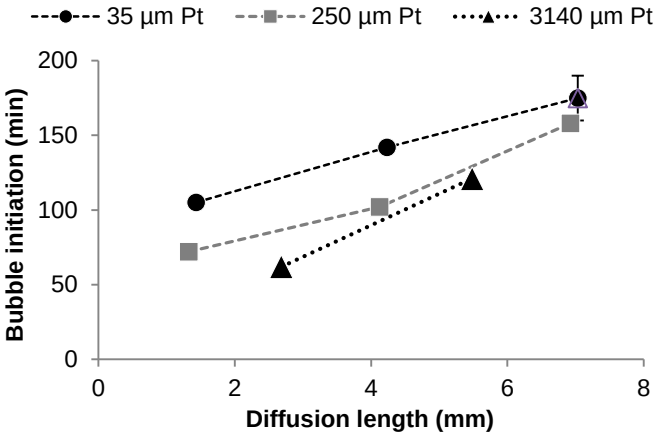

Figure D1: Effect of the diffusion length and the Pt length on the bubble initiation time for a constant nanochannel width of 50 µm and different platinum lengths (35, 250 and 3140 µm). The experiments were performed with 0.64 mol H2O2/L.

Appendix E: Bubble migration

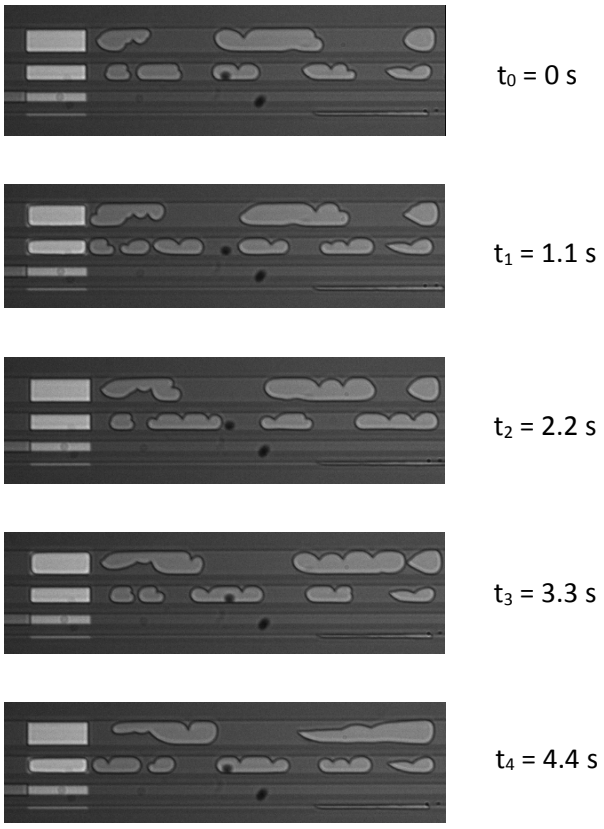

Figure E1: Evolution of the bubbles growing towards the microchannel filled with H_2O_2 after 532 min of experiment. Images were taken every 1.1 second. Nanochannels have a length of 2.9 mm, widths of 10, 30, 50 and 70 μm and a platinum length of 180 μm. The experiment was performed with a solution of 0.64 mol H_2O_2/L.

Appendix F: Calculation of H_2O_2 conversion

The conversion of H_2O_2 in the experiments with bubble formation towards the nanochannel filled with water (presence of convective flow) was calculated according to Equation F1:

$$Conversion\ H_2O_2 = \frac{H_2O_2\ converted}{H_2O_2\ fed} * 100 = \frac{\frac{2*\left(V_{O_2,f} - V_{O_2,i}\right)}{t_f - t_i} * \frac{P}{R*T}}{v*A*[H_2O_2]} * 100 \qquad \text{Equation F1}$$

Where $V_{O_2 f}$ and $V_{O_2 i}$ (m^3) are the volumes of the oxygen bubble at times t_f is and t_i (s) respectively; P is the pressure in the nanochannel (1 + ΔP bar), R (m^3 * bar * K^{-1} * mol^{-1}) is the constant of ideal gases, T (K) is the temperature in the nanochannel, v (m * s^{-1}) is the linear velocity of the liquid in the nanochannel, A (m^2) is the cross-sectional area of the nanochannel and [H_2O_2] (mol * m^{-3}) is the concentration of H_2O_2 in the feed stream.

Chapter 6

Concluding remarks and recommendations

1. Performance of membrane reactors in nitrite hydrogenation

Chapter 2 and 3 show that membrane reactors have a great potential for application in three-phase catalytic reactions where the independent control of both, gas and liquid phases is essential to regulate activity and selectivity. This was demonstrated for nitrite hydrogenation, where the H/N ratio of reaction intermediates at the catalyst surface has a remarkable effect on the product selectivity. To achieve high nitrogen selectivities (the desired product of the reaction), low H/N ratios are required. This can be accomplished by decreasing the concentration of hydrogen in the reaction zone by simply diluting hydrogen in an inert gas, resulting in low but homogeneous hydrogen concentration through the axial direction of the reactor. However, this is not feasible with conventional reactors where the gas is pre-saturated in the liquid, since small hydrogen concentrations would lead to low conversions and to an inefficient use of the catalyst. An increase in nitrogen selectivity can also be achieved by increasing the nitrite concentration. However, the concentration of the N-contaminant in waste water will be already pre-determined by the feed stream.

Nitrogen selectivity can also be tuned by varying the diffusion distance of the reactants to the reaction zone. This was shown in chapter 3 with the use of egg-shell membrane reactors which differed in the location of the active zone (figure 2a, b and c, chapter 3). It was observed that when the active zone is located near the gas feed and far from the nitrite solution, the nitrogen selectivity decreases dramatically. In this case, nitrite has to overcome a long diffusion barrier (300 μm) consisting of alumina pores filled with water, resulting in low nitrite concentrations in the reaction zone. On the other hand, hydrogen only has to diffuse through 10 μm of PDMS to reach the catalyst. This leads to extremely high H/N ratios which generate nitrogen selectivities close to zero. To favour the formation of nitrogen, diffusion barriers should be maximized for hydrogen and minimized for nitrite. This could be accomplished with various approaches. For instance, in the case of the thin egg-shell structure, the PDMS membrane could be coated in the inside wall of the alumina hollow fibre. Then, gas would be fed from the tube side while the nitrite solution

would flow around the shell of the alumina. The hydrogen diffusion barrier can also be increased by increasing the thickness of the PDMS layer by successive PDMS coatings or *via* coating with denser PDMS solutions. Additionally, synthesis of yolk-shell membrane reactors would also enhance the formation of nitrogen by shortening the diffusion distance of nitrite. To obtain such structures, the reactive gases during CNF growth should be fed from the tube side rather than from the alumina shell. An alternative would also be to selectively deposit nickel (catalyst for the CNFs) near the inner alumina wall instead of throughout the entire wall of the alumina.

In conventional reactors where gas and liquid are fed together, the concentration gradients inside the catalyst particles, if any, present similar profiles for nitrite and hydrogen. This leads to relatively constant H/N ratios along the catalyst pores. In contrast, in membrane reactors, the hydrogen concentration along the radial direction varies significantly. Analogously, nitrite concentration also experiences changes in the radial direction. This leads to a wide range of H/N ratios throughout the different radial positions. As a consequence, each radial position may present different kinetics (activation energy and reaction orders) and product selectivities. This sometimes induces counter-intuitive behaviours that can only be properly explained by modelling the reaction in the radial direction (modelling in the axial direction would also be necessary in the case of none differential conversions). For instance, competitive adsorption between nitrite and hydrogen was observed for thick or full CNF coverages, but not for thin CNF coverages in the egg-shell membrane reactors.

It is important to consider that in real water treatment, the waste stream is saturated in air and not in argon, as presented in this work. Therefore, studies using nitrite solution saturated in air should be performed to assess the effect of oxygen on the nitrite hydrogenation. Preliminary results demonstrated (not shown in this thesis), that the addition of oxygen is beneficial in terms of activity and selectivity since it reacts with the adsorbed hydrogen, thus decreasing the H/N ratio and the competitive adsorption. Future work should also study nitrate hydrogenation.

Initial tests with membrane reactors loaded with Pd-Cu bimetallic catalyst exhibit catalytic activity in nitrate hydrogenation. The Pd/Cu ratio strongly influenced the product distribution. Furthermore, a strong effect of the H/N ratio on the product selectivity was also observed. Finally, tests under real conditions and at long reaction times should be performed to assess the viability of these membrane reactors for real water purification.

2. Activity of the nickel 'hairy' foam in nitrite hydrogenation

Chapter 4 shows that nitrite hydrogenation can be performed in the absence of noble metals. This reduces the cost of the catalyst, making the process more economical. Experiments with nickel 'hairy' foams were performed both, with and without Pd. Results showed activities in the same order of magnitude in the presence and absence of the noble metal. The activity of the nickel 'hairy' foams (without Pd) was attributed to the presence of dissolved carbon in the nickel particles located within the CNF structure. Despite the observed high activities, the nitrogen selectivities obtained were low (30%). This is caused by the relatively high hydrogen concentration pre-dissolved in the liquid. To prevent this, low hydrogen concentrations should be fed to the reaction zone. This could be done with the use of hollow nickel 'hairy' foam membrane reactors. As mentioned in the previous section, low hydrogen concentrations could be supplied with this reactor configuration, achieving high nitrogen selectivities. An alternative would be to use formic acid as reducing agent. Low hydrogen concentrations could be obtained by slowly decomposing formic acid at moderate temperatures. Preliminary results showed that formic acid can already decompose and hydrogenate nitrite at room temperature, leading to higher nitrogen selectivities.

Future work should study the use of nickel 'hairy' foams in nitrate hydrogenation. Initial tests showed that nitrate can also be hydrogenated in the absence of noble metals but also exhibits low nitrogen selectivities. Further studies could also focus on reactions catalysed by noble metals. However, it is important to consider that the

presence of oxygen, especially at elevated temperatures, should be prevented since it causes catalyst deactivation due to nickel passivation and carbon oxidation (CO_x formation). Even though the catalyst could then be re-activated in hydrogen, there would be an irreversible decrease in the steady state activity.

3. H_2O_2 decomposition over a model pore catalyst

Datsevich [1, 2] described the oscillation theory to predict the effect of bubble formation in a catalyst pore on the reaction kinetics and transport phenomena. He predicted that bubbles would generate an oscillation movement that will create a forced convection inside the catalytic pores. Experiments performed in model catalyst pores (chapter 5) showed that bubble formation can indeed generate a convective flow that enhances mass transport and reaction rates inside the pores. However, it was also observed, that bubble formation can also be detrimental since it can physically block the H_2O_2 transport to the catalytic active sites, suppressing the reaction. All these results indicate that reaction and diffusion cannot be always described using the conventional Thiele and Zeldovich theory.

Real catalyst pores differ from the model pores as they are 3D networks with smaller pore dimensions and homogeneous catalyst distribution, instead of isolated pores with all the catalyst located in the centre. However, this study provides not only a qualitative understanding of the effect of gas bubbles on the transport mechanisms and reaction rates, but also for the first time direct observation of bubbles inside a catalyst pore. In further work, microreactors with more realistic pores could be fabricated and tested in H_2O_2 decomposition. Other three-phase catalytic reactions with gaseous products, such as formic acid decomposition or nitrite hydrogenation, could also be tested.

Surprisingly, the kinetic constant for H_2O_2 decomposition in the studied system was several orders of magnitude higher than the kinetic constants reported in literature. This was probably caused by the superior activity of certain exposed Pt planes in the Pt patch used in the model catalyst, quite different form the usual supported Pt

nanoparticles. These results call for further investigation since the intrinsic activity of some Pt-catalysed reactions could be significantly enhanced.

4. References

1. Datsevich, L.B., *Alternating motion of liquid in catalyst pores in a liquid/liquid–gas reaction with heat or gas production.* Catalysis Today, 2003. 79-80: p. 341-348.
2. Datsevich, L.B., *Some theoretical aspects of catalyst behaviour in a catalyst particle at liquid (liquid–gas) reactions with gas production: oscillation motion in the catalyst pores.* Applied Catalysis A: General, 2003. 247(1): p. 101-111.

Summary

This work aimed at fabricating structured catalytic reactors for fast multiphase reactions, namely, nitrite hydrogenation and H_2O_2 decomposition. These reactors allowed a better understanding of these reactions and an improvement in terms of catalytic activity and selectivity.

In **chapters 2 and 3**, membrane reactors were fabricated to improve the selectivity of nitrite hydrogenation. These reactors allow an independent control of the gas and liquid phase, which is essential to manipulate the concentration of the reactants in the reaction zone. They were fabricated by growing CNFs throughout the wall of an α-alumina hollow fibre and depositing Pd nanoparticles on the surface of the CNFs. The outer wall was coated with a PDMS membrane to avoid water permeation.

In **chapter 2**, reactor fabrication was optimized to obtain high surface areas (17 m^2/g) without compromising the open structure of the CNFs by limiting the extent of filling of the alumina pores (25 vol%). The optimal conditions were a nickel concentration of 1 g/L, nickel reduction temperature of 850 °C and CNF growth temperature of 600 °C. The optimized reactor was compared with two different reactor layouts with identical textural and chemical properties but differing in the flow operation. It was demonstrated that the selectivity towards nitrogen is enhanced with the membrane reactor. This was attributed to the low and homogeneous hydrogen concentration fed through the membrane, leading to low H/N ratios of reaction intermediates at the catalyst surface. Experiments performed with various hydrogen and nitrite concentrations also proved the important effect of the H/N ratio in the selectivity.

In **chapter 3**, different egg-shell membrane reactors were fabricated and tested in nitrite hydrogenation. They varied in the distribution of the Pd loaded CNFs through the membrane wall. The thickness of the CNF containing layer was determined by the CNF growth time. A growth time of 10 min led to thin layers

filled with CNFs of 200 μm, while a growth time of 45 min led to a complete CNF coverage of the internal surface of the alumina membrane. The catalytic results showed that thin layers filled with CNFs exhibit very low nitrogen selectivities due to the proximity of the hydrogen feed and the distance to the nitrite stream. In contrast, full CNF coverage resulted in the highest nitrogen selectivities due to similar diffusion distance of both reactants to the reaction zone. A decrease in hydrogen concentration showed again an increase in nitrogen selectivity, but surprisingly, indicated the presence of a competitive adsorption between nitrite and hydrogen for thick CNFs layers.

In **chapter 4**, a nickel 'hairy' foam catalyst consisting of a thin layer of CNFs covering a nickel foam was synthesized, characterized and tested in nitrite hydrogenation. It was proven that the reaction can be performed without the use of noble metals. The catalytic activity was attributed to the nickel particles generated during the CNF growth, which contain dissolved carbon that enhance the activity of the nickel. Experiments demonstrated that during oxidation at various temperatures, nickel passivates and becomes inactive. A posterior reduction treatment at room temperature re-activates the nickel particles, but decreases the steady state activity due to partial removal of the carbon *via* oxidation (CO_x formation).

In **chapter 5**, a microreactor was designed and fabricated to perform the catalytic decomposition of H_2O_2 inside a model catalyst pore. This microreactor was coupled with a microscope and was used to investigate the behaviour of gas products in catalytic pores during three-phase catalytic reactions. Experiments demonstrated that if the concentration of the gas products surpasses the saturation concentration, bubbles will form and will affect the reaction rate. Bubble formation will suppress the reaction rate if it physically blocks the diffusion of H_2O_2 to the catalytic active sites. In contrast, bubble formation will enhance the reaction rate if bubbles migrate, creating a convective flow that accelerates H_2O_2 transfer to the catalyst.

Samenvatting

Dit werk had als doel om gestructureerde katalytische reactoren te maken voor het uitvoeren van snelle meerdere fase reacties, met name nitriet hydrogenatie en H_2O_2 ontleding. Deze reactoren zorgen beide voor een beter begrip van de reacties en verbeteren de katalytische activiteit en selectiviteit.

In **hoofdstuk 2 en 3**, wordt beschreven hoe membraan reactoren warden gemaakt om de selectiviteit van nitriet hydrogenatie te verbeteren. Deze reactoren maken een onafhankelijke controle over de gas- en vloeistoffase mogelijk, dit is essentieel voor het manipuleren van de verschillende concentraties in de reactiezone. Ze werden gemaakt door het groeien van koolstofnanofezels (CNFs) binnen de structuur van een α-alumina holle fezel en vervolgens Pd nanodeeltjes op de CNFs te deponeren. De buitenkant van de holle fezel werd gecoat met een PDMS-membraan om water permeatie te voorkomen.

In **hoofdstuk 2**, werd de reactorfabricage geoptimaliseerd voor het verkrijgen van een hoog specifiek oppervlak (17 m^2/g) zonder de open structuur van de CNFs te compromitteren, door het limiteren van de vulling van de alumina poriën (25 vol%). De optimale condities waren: een nikkel concentratie van 1 g/L, nikkel reductie op een temperatuur van 850 °C en CNF-groeitemperatuur van 600 °C. De optimale reactor werd vergeleken met twee verschillende reactor ontwerpen met een identieke structuur en chemische eigenschappen, maar verschillende vloeiingsconfiguraties. Er werd aangetoond dat de selectiviteit richting stikstof wordt verbeterd met de membraanreactor. Dit effect werd toegeschreven aan de lage en homogene waterstofconcentratie die door de membraan werd toegevoerd, waardeer er een lage H/N-ratio of reactietussenproducten op het katalysatoroppervlak. Verscheidenen experimenten met verschillende waterstof en nitriet concentraties bewezen ook het belang van de H/N-ratio op de selectiviteit.

In **hoofdstuk 3** werden verschillende 'egg-shell' membraanreactoren gemaakt en getest in de hydrogenatie van nitriet. Er werd gevarieerd met de distributie van de Pd beladen CNF laag door de reactordoorstede. De dikte van de CNF lag werd bepaald door de groeitijd van de CNFs. Een groeitijd van 10 minuten leidde tot een CNF lag met een dikte van 200 μm, terwijl een groeitijd van 45 minuten leidde tot een complete CNF-bedekking van het interne oppervlak van het alumina. De resultaten van de test van het katalytisch systeem toonden aan dat een dunne CNF laag leidt tot een lage stikstofselectiviteit, door de korte afstand van de waterstofbron en een grote afstand tot de nitrietbron. Daarentegen gaf een volle CNF-groei een hoge stikstof selectiviteit, vanwege de vergelijkbare diffusielengtes voor beide reactanten naar de reactiezone. Het verlagen van de waterstofconcentratie leidde ook tot een verhoogde stikstof selectiviteit, maar verassend lied het ook een competitieve adsorptie tussen nitriet en waterstof zien, voor de dikke CNF lagen.

In **hoofdstuk 4**, werd een nikkel 'hairy foam' katalysator, bestaande uit een dunne laag CNFs over een nikkel schuim, gesynthetiseerd. Bewijs werd geleverd dat de reactie ook verloopt zonder de aanwezigheid van edelmetalen. Deze katalytische activiteit werd toegeschreven aan de nikkel deeltjes die gevormd worden tijdens de CNF-groei, deze bevatten opgelost koolstof wat de activiteit van het nikkel versterkt. Proeven laten zien dat door de oxidatie van nikkel op verscheidene temperaturen het nikkel voor gepacificeerd en inactief wordt. Een latere reductie van de nikkel deeltje op kamertemperatuur zorgt voor een heractivatie, maar de stabiele activiteit neem af, vanwege de gedeeltelijke verwijdering van het koolstof via oxidatie (CO_x formatie).

In **hoofdstuk 5**, werd een microreactor ontworpen en geconstrueerd, om het katalytisch omzetten van H_2O_2 in model katalysator poriën na te bootsen. De microreactor werd gekoppeld aan een microscoop, waarmee de gasformatie in de poriën werd gevolgd tijdens een drie-fase katalytische reactie. De proeven lieten zien dat, als de concentratie van het gas boven de verzadigingsconcentratie komt, bubbels zullen vormen, deze bubbels hebben een effect op de reactiesnelheid. De

bubbelvorming zal de reactie onderdrukken als deze fysiek de diffusie van H_2O_2 blokkeert richting het actief katalytisch oppervlak. In tegenstelling zal bubbelvorming de reactiesnelheid verhogen als de bubbel zich gaat bewegen en zo doende een convectieve vloeiing genereerd die het transport van H_2O_2 naar de katalysator vervorderd.

List of publications

Journal papers

1. Brunet Espinosa, R.; Rafieian, D.; Lammertink R.G.H and Lefferts, L.; Carbon nano-fibre based membrane reactor for selective nitrite hydrogenation (accepted in Catalysis Today journal).

2. Brunet Espinosa, R.; Rafieian, D.; Postma, R.S.; Lammertink R.G.H and Lefferts, L.; Egg-shell membrane reactors for nitrite hydrogenation: manipulating kinetics and selectivity (submitted to Applied Catalysis B: Environmental journal).

3. Brunet Espinosa, R.; Lefferts, L., Ni in CNFs: highly active for nitrite hydrogenation (submitted to ACS Catalysis journal).

4. Brunet Espinosa, R.; WijnPerlé, D.; Duits, M.H.G.; Mugele, F.G.; Lefferts, L., Hydrogen peroxide decomposition in a microreactor: effect of bubble formation on reaction rate (in preparation).

Patents

1. Brunet Espinosa, R.; Rafieian, D.; Lammertink R.G.H and Lefferts, L; Bruggink, W; Duineveld, P – Water purification catalyst, water purifier, beverage maker and method – EP15161426.0

Oral presentations

1. 4th International Conference on Structured Catalysts and Reactors (ICOSCAR-4) – Structured catalysts and reactors for the selective reduction of nitrite and nitrate to N_2 in water – 2013.

2. Netherlands' Catalysis and Chemistry Conference (NCCC XV) – Use of membrane reactors for the selective reduction of NO2- to N2 in water – 2014.

3. NanoCity2014 – Selective reduction of nitrite and nitrate to nitrogen in liquid phase – 2014.

4. Netherlands Process Technology Symposium (NPS14) – Structured membrane reactor for the selective reduction of nitrite and nitrite to N2 in water – 2014.

5. 9th International Symposium on Catalysis in Multiphase Reactors (CAMURE-9) – Manipulating selectivity in nitrite hydrogenation with a catalytic membrane reactor – 2014

6. Netherlands' Catalysis and Chemistry Conference (NCCC XVI) – Nobel Ni-carbon nanofiber based catalyst for nitrite and nitrate hydrogenation – 2015.

7. 24th North American Catalysis Society Meeting (NAM24) – New structured catalysts with enhanced mass transfer; towards selectivity control – 2015.

8. Chemistry As Innovating Science (CHAINS 2015) – Selective nitrite hydrogenation using a catalytic membrane rector – 2015.

9. Netherlands' Catalysis and Chemistry Conference (NCCC XVII) – New structured catalyst with enhanced mass transfer: improve selectivity – 2016.

Poster presentations

1. Netherlands' Catalysis and Chemistry Conference (NCCC XIII) – Reduction of nitrite and nitrate in aqueous phase – 2012

2. Netherlands' Catalysis and Chemistry Conference (NCCC XIIV) – Use of *hairy* supports for the reduction of nitrite and nitrate in aqueous phase – 2013

3. Ith European Congress on Catalysis (Europacat) – Structured catalyst-reactor for the selective reduction of nitrite and nitrate to N_2 in water – 2013

4. 8th International Conference on Environmental Catalysis (ICEC) – Structured membrane reactors for the selective reduction of nitrite and nitrate to N_2 in water – 2014

Awards

1. NIOK poster award for the best poster presentation – NCCC XIII

2. NIOK lecture award for the best oral presentation – NCCC XVII

Acknowledgments

You are now holding in your hands 4 to 5 years of my life, please be gentle with this book, it cost a lot of suffering and effort. This does not mean that I am expecting you to read the full book, just reading this section will be enough! Actually you can go ahead with the conventional way of reading the acknowledgments: fast screening through the text to make sure that your name is in there and then come back to this point again to continue reading. I apologize in advance if I did not include your name, probably it would have been a better idea not to write the acknowledgements the night before sending the thesis for printing…

During these last years I have grown as a scientist and hopefully, have entered in the Dr. community. However, what I will remember the most from my Dutch journey are the people I met on the way. You have all contributed in some extend to my thesis and made this day happen. First, I would like to thank Leon Lefferts for giving me the opportunity of doing my PhD in the Catalytic Processes and Materials (CPM) group. From the first day you gave me a lot of freedom in my research and you stimulated me to give 100% of myself. I learned from you that good is not enough, it should be perfect, because quality is always better than quantity. One of the things I will never forget (and maybe now is the perfect time to share) is the day I had my PhD interview and we went to the Faculty Club for lunch. That day I lied, I did not understand Dutch at all, and of course I did not know that 'paddenstoelen' meant mushrooms, otherwise I would have never ordered this dish for lunch because I hate them! It was so hard to finish it…, especially because I had to eat fast to keep up with your speed and in the meantime try to focus on the scientific discussion about nitrite hydrogenation which at that time seemed as confusing as Chinese language. I would also like to thank Seshan for all the non-scientific discussions about football, chess, bridge and life in general. I admire the way you connect with people, always trying to help and getting the best out of them. Barbara and Arie, I am grateful for the time we shared in CPM, you are both missed a lot! Rob Lammertink, your input in the second and third chapter was crucial as well as your effort to coordinate the NanoNextNL program. I still remember your first email when you asked me to collaborate with Damon on the membrane reactor project, was that a punishment? ☺ Frieder and Michel, your expertise in the field of microreactors made the fifth chapter possible. I really appreciate all your help and patience. Daniel, the

cleanroom master, thanks a lot for the exciting collaboration we had during the last years. We had a nice deal: you made the chips, I broke them. Gido Mul, Roland Dittmeyer and Harry Bitter, thanks for accepting being part of my committee, I am looking forward for a nice discussion on the 3rd of June.

Reached this point, I cannot continue without acknowledging Bert Geerdink. I always thought that there are two type of people: you and the rest. I could thank you for all the help in the lab, for all the fun in the borrels and for being the glue that binds all CPM together. However, what I remember the most is the full week you spent trying to recover the data from my hard drive (although we both knew that most likely, it would not work). Louise, Tom and Karin, thanks for all the characterization measurements and especially for not giving up on helping me with Dutch. Ruben, is there any sport that you are not good at? I enjoyed very much being part of your football team and playing tennis with you during lunch time (losing 6-1 was already a victory for me!). Frank, you are a funny and easy-going guy! I think that half of the time we talked was to complain about the salaries of the football players and their big egos.

In CPM I had a great time and I got to know many people that I will never forget! Most of them already left the group, others still have a long way to go. Yingnan, my IC brother, I am happy that we managed sharing the lab equipment for so long without killing each other. It was comforting to see that I was not the only crazy person working after midnight in the lab! Masoud, you thought me the first Farsi word. From the reaction of the other Iranian people I somehow understood that it is not a word that I should use the day I travel to Iran. Chau, you definitely have an answer for everything. I think I know you well enough to say that you have two passions in this life: cooking and talking! I will never forget that morning when I came early to office and I found you in the middle of the room inside a sleeping bag. Kamilla, the office became very boring and quiet when you left. I still think that we did a mistake stopping our morning competition on who would arrive first in office, my productivity was much higher at that time. Also thanks for improving my English, even though it meant being corrected every other sentence… Joline, I think you were the only PhD that kept talking in Dutch to me since the day I announced that I was seriously intending to learn it. Ok, it is true that you are the only Dutch PhD in the group, but still. Thanks a lot for introducing me to board games! Since then my game stack has been

increasing exponentially. Congratulations again to you and Arnout for your beautiful daughter! Shilpa and James, I enjoy very much each of our game nights! We should do that more often! But please Shilpa, stop winning in T'zolkin, give some chances to the other players every now and then. Arturo, I still wait for the beer you promised me if I would be able to run 10 km at your pace. I will be honest with you, I was broken after that and it took me a year to decide to run again. José Medrano Catalán, la bomba dancer and the expert in active sites! I never told you but your second last name is inspiring and beautiful. I hope you still remember our conversations in Catalan ☺. Jose Baeza, you spent a short time in the group but we became very good friends! It is true that you are from Madrid, but of course, no one is perfect ☺. The weekend that Maria and I spent with you in Madrid was fantastic! I am looking forward for the next occasion! Hrudya, Marijana and Son thanks also for the time we shared in CPM! Kaisa, the trip to USA would not have been the same without you! The only thing I regret is not being able to escape the room, we just needed 30 more seconds. Cristina, you were always happy and laughing! You showed me that, indeed, the best jam is in the small jar. Marta, I was very surprised with your music taste, we even named the whatsapp group after your favorite style (Surra de Bunda). Jie, my Chinese brother, I enjoyed very much being around you, except that day in the cooking workshop when you almost stabbed me with that big kitchen knife. Tushar, I am proud to say that I witnessed your first beer and liquor of God, was it the night of the Persian New Year? Pramod, please do not ever use the Spanish words I have taught you, unless you want to make enemies. I will follow the same advice with the words you taught me too! Reza, I wish I had more time to learn some Farsi from you but you came during my crazy last year of PhD. I had fun that evening playing ping-pong with you, Xavi and Damon. Just for the record: the Spanish team won! Guido, the party boy/animal, you do not go to parties, parties come to you! I heard that you like striping, I somehow consider myself lucky of having missed that… Songbo, you are very friendly and always in a very good mood! I think nowadays you are the only one who can compete with Bert on Friday evenings.

During my PhD journey, I had to supervise some students. They are the main reason why you are now holding my thesis in your hands. Alwin, I am happy that at the end you find your way! Hassan, you are the clear example that motivation and effort always lead to success. Anne, your work was enormous! You were always enthusiastic, perseverant and creative, some of the best qualities to become successful in your professional career. Thom, I

still have tones of unpublished data belonging to your work, one of these days I will do something about it. During the 9 months that you stayed in the group we became friends! I still remember the night I came to your place after the Alembic party. Did you know that I had a meeting next day at 10 a.m.? Rolf, you are extremely sharp! The quality of your work and your critical attitude towards the results amazed me. No wonder why Leon offered you a PhD position in the group. Thanks a lot for translating my summary to Dutch with such a short notice and sorry for forgetting your name in the NCCC presentation! I think you deserve an extra line in the acknowledgments of this thesis to compensate for it ☺.

Although I was part of CPM, I probably spent more time in SFI group, and I think we all know who is the responsible for this. Yali, sorry for coming to your office 10 times a day, and we both know that I am not exaggerating. Sander and Khalid, we should have gone for often to play ping-pong! Hanieh, your Persian handwriting looks like art. Jeff, I hope it was not your idea to put the romantic song in Damon's stuckje, you just took away all my dignity… Aura, thanks for reactivating my passion for tennis! I was very surprise when I found out that you can understand Spanish and Catalan.

I would also like to thank all the people from SPT group, you really look like a big family! Ehsan, I hope the girl I brought to you in Sushil's defense was your taste, at least you did not waste your time with her, not even for exchanging names. We have to go to the casino some other times, I know that it is far from your place but we can always go by taxi and come back with limousine ☺. Rens and Stijn, I had so much fun in India and in Munich with you! Stijn, you are always sharp in time but that day in the October fest, 'we are coming out in 5 minutes' became ' we will come out tomorrow or maybe the day after'. Rens, since Munich I hate sardines, can you guess why? Sam, you are a second hand child-stuff store. Thank you so much for all the things you gave to me and Maria. Prasad, the best Indian guy ever, I will never forget the experience of being in an Indian wedding! Guus, Varsha, Martin, Xiao Hua, Cindy, Sushil, Marek, Michal, Stevia, Lisette, Sandra, Diego, Pushkar, Pavlina and Laura, you are all amazing!

Here comes the category of the unclassified people but definitely, not less important than the rest. Erik (my Bulgarian friend) and Krzysztof (the toughest name to write!), we were the NanoNext team! Why did we stop playing snooker? I think it is because Damon started getting angry… Can, I am sorry for the two old Turkish ladies I found for you in Munich, it

seemed such a good idea at that moment! I still remember that day you called me on the phone, I could just understand: 'CNF', 'boom', 'oven'. Dimitris 'the philosopher', even though we both live in Enschede we keep just meeting in PhD defense parties. We have to do more risk games. Bijoy, I have never seen anyone belonging to so many football teams! Akansha, we both share the love for Guiness (you even drink them faster than me!).

During the last few weeks/months of writing this thesis I already started working at Eurekite. Sorry guys for complaining always about the few hours I slept the night before. Combining writing and working is quite difficult, especially if you want to include sleeping in the equation. Gerard and Bahruz, thank you for giving me the chance to work at your company. Gerard, the first time you called me on the phone I was in the casino, that day I was not winner but I got the feeling that something great was about to happen. Umit, I have never seen anyone providing as many examples as you! Marcel, you know about everything, you are like an encyclopedia! Pavel, it was funny to be interviewed by you when probably few weeks before we were at Molly´s watching a Barcelona match. We should keep practicing poker, hoping to get an extra salary instead of losing the one we have.

And finally it is the turn for my paranymphs. I consider you much more than friends: you are family! We have shared so many great moments that I will have a hard time choosing just a few. Filipe, Enschede is very quiet since you and Sherry left! I miss coming every weekend to your place and playing games until 4:00 a.m.! I think we never stopped because it was too late, we were just physically dead. Why are you so good at 'Love Letter'? You always rock it when we play it! To be honest, I am a bit worried that you will forget to come today, like the day you forgot that you had to take the plane from USA to Amsterdam. Please, do not forget your suit in the train, just wear it from home, otherwise it may end up forgotten in an empty train sit like all those hats, scarfs and umbrellas that you weekly lose. I know that your revenge will come later in the evening, so let me have here my moment. Damon, the first time I met you there was, of course, no romantic song was playing. I remember that at the beginning you were very polite and always saying yes to everything even before I would finish the sentence. Therefore, I had to start using the word 'umbrella' in between sentences to really see if you were paying attention at what I was saying. You probably noticed 1 out of 10! I was also sad when you left Enschede! However, when you come back, I know that you are in good hands because Johny is taking good care of you. We

were lucky that no one ever discovered what is hidden in the Horst Tower, the blockage-in was always my favorite! Do you remember the day that we almost became rich? The feeling was so strong that the electricity went off. This was our chance because the table is always broken! If you say 'kapot' one more time you know what will happen… Sherry, you are the best artist I know, you should never stop painting, even though Arion is taking most of your time. It was amazing to have you and Filipos in Barcelona, I hope there are many more trips to come. I have to admit that I have never seen anyone so passionate about ice creams (well, maybe your mother!). Saghar, you are the most strong and hard-worker person that I have ever seen: no challenge is impossible for you! However, you should practice backgammon a bit more, I can give you some tips if you want ☺. Let's not forget about the trip to Japan!

In Barcelona I have left many people that mean a lot to me. Aleix, Uri, Vic and Pol, thanks for proving to me that distance does not matter at all and for being always there when I needed you! I really hope that some of you can make it to my defense. I would also like to thank my whole family which recently (officially) increased one order of magnitude! Papa, mama, sorry for freaking you out in January 2016 when I told you that I was not sure if I could make this thesis happen. Tieta, I am happy that now all the family is living together! Avia, I am so happy that you could come once to Enschede, we had an amazing time! Avi, it hurts not to have you here today and not being able to share with you this moment of happiness. This thesis is dedicated to you! I will always love you!

Of course, I could never forget the most important person of my life! Maria, I met you when I was 18 and from then I knew for certain that you were the person I would like to have next to me until my last day. We have shared so much and spent so many unforgettable moments together that I cannot recall them all anymore. All these years you have been an inspiration for me, you are simply perfect, I would change nothing from you. A new step in our lives is now approaching and I do not feel scared at all, because next to you, there is nothing that can ever go wrong! Thank you Maria, t'estimo!

Roger